

**FATIGUE AND CYCLIC LOADING OF 3D PRINTED SOFT POLYMERS FOR  
ORTHOPEDIC APPLICATIONS**

A Dissertation  
Presented to  
The Academic Faculty

by

Andrew T. Miller

In Partial Fulfillment  
of the Requirements for the Degree  
Doctor of Philosophy in Bioengineering

Georgia Institute of Technology  
May 2017

Copyright © 2017 Andrew T. Miller

**FATIGUE AND CYCLIC LOADING OF 3D PRINTED SOFT POLYMERS FOR  
ORTHOPEDIC APPLICATIONS**

Approved by:

Dr. Robert E. Guldborg, Advisor  
Institute for Bioengineering and  
Bioscience  
Woodruff School of Mechanical  
Engineering  
*Georgia Institute of Technology*

Dr. Ken Gall  
Department of Mechanical  
Engineering and Materials  
Science  
*Duke University*

Dr. Johnna S. Temenoff  
Wallace H. Coulter Department  
of Biomedical Engineering  
*Georgia Institute of Technology*

Dr. Nick Willett  
School of Medicine  
*Emory University*  
Institute for Bioengineering and  
Bioscience  
*Georgia Institute of Technology*

Dr. Meisha L. Shofner  
School of Materials Science and  
Engineering  
*Georgia Institute of Technology*

Date Approved: March 30, 2017

## ACKNOWLEDGEMENTS

I would like to thank Ken Gall, for taking on a new student even when the timing was not ideal, for enabling me to chase this opportunity in a doctoral program and open new doors for myself, and for starting me on a project that truly interested me. I would like to thank Robert Guldberg, for seeing the potential in me and being a tremendous source of guidance throughout my studies. I would like to thank my remaining committee members: Johnna Temenoff, Nick Willett, and Meisha Shofner, for their time and thoughtful input in making this thesis what it is today. I would like to thank David Safranski, for being my go-to source for technical guidance, for all the time he devoted to my work, and for making sure I did not poke my eye out or otherwise maim myself in the lab. I would like to thank Dalton Sycks, Ken Dupont, Kat Smith, Nathan Evans, Brennan Torstrick, Angela Lin, Hazel Stevens, and the remainder of the Guldberg lab for their input and guidance throughout my project. I would like to thank Kurt Jacobus and Medshape Inc., for allowing me to use their facilities and dealing with the unrelenting noise of a 3D printer. I would also like to thank Catherine Wood, Kanchi Patel, and Nick Watson, all of whom were outstanding undergrads and vital to my success.

Lastly, I would like to thank my family and friends for their tremendous support throughout my doctoral program. Thanks to my parents and in-laws, who were overwhelmingly supportive from the very first day I mentioned returning to school. A special thanks to my mother, who has always been one of my biggest cheerleaders and sources of encouragement. Thanks to my brother Rob and good friends Way Joe and Justin, for putting up with my research talk and rants, and for being a welcome distraction. Finally,

and most importantly, I would like to thank my wife Lisa. Thank you Lisa, for your support throughout the program, for your patience and understanding, for making me smile when I was stressed, and for believing in me. Without the support of my family and friends, this adventure would literally have never happened.

## TABLE OF CONTENTS

ACKNOWLEDGEMENTS	iii
LIST OF TABLES	vii
LIST OF FIGURES	viii
LIST OF ABBREVIATIONS	xiii
SUMMARY	xiv
CHAPTER 1: INTRODUCTION	1
1.1 Background, Motivation, and Significance	1
1.2 Research Aims	8
CHAPTER 2: LITERATURE REVIEW	11
2.1 Fatigue of Biomedical Elastomers	11
2.2 Fatigue of 3D Printed Polymers	15
2.3 Fatigue of Polymer Scaffolds & Porous Polymers	16
CHAPTER 3: EFFECT OF POLYMER STRUCTURE ON THE FATIGUE AND CYCLIC LOADING PROPERTIES OF SOFT BIOMEDICAL POLYMERS	18
3.1 Introduction	18
3.2 Materials and Methods	19
3.3 Results	24
3.4 Discussion	38
3.5 Conclusions	44
CHAPTER 4: EFFECTS OF POLYMER STRUCTURE AND 3D PRINTING ON THE MECHANICAL PROPERTIES AND FATIGUE PERFORMANCE OF PCU	47
4.1 Introduction	47
4.2 Materials and Methods	48
4.3 Results	62
4.4 Discussion	86
4.5 Conclusions	94
CHAPTER 5: EFFECT OF PRINTED ARCHITECTURE ON THE MECHANICAL PROPERTIES AND FATIGUE PERFORMANCE OF POLYURETHANES	97
5.1 Introduction	97
5.2 Materials and Methods	98
5.3 Results	108
5.4 Discussion	129
5.5 Conclusions	138

CHAPTER 6: FOLLOW-UP STUDIES	140
6.1 Introduction	140
6.2 Materials and Methods	141
6.3 Results	144
6.4 Discussion	152
6.5 Conclusions	155
CHAPTER 7: CONCLUSIONS AND FUTURE WORK	157
REFERENCES	167
VITA	187

## LIST OF TABLES

Table 1.1: Modulus data for common implant materials versus soft tissue.	2
Table 3.1: Glass transition temperature determined from DMA and DSC.	26
Table 3.2: Moduli data.	29
Table 4.1: Tabulated data from FDM quality control tests.	54
Table 4.2: Tabulated transition temperatures from DSC and DMA data, ND denotes not detectable (n = 3 for each grade and processing method).	64
Table 4.3: Degree of phase separation as determine from Equation 4.1. No significant differences were found between IM and FDM samples of the same grade.	68
Table 4.4: Tabulated tensile failure stress and strain for FDM and IM samples (n = 10 for FDM, n = 3 for IM).	76
Table 5.1: Summary of tested architectures.	102
Table 5.2: Porosity, crosshatch dimensions, and tensile data for all samples (n = 3).	109
Table 6.1: Summary of tested groups for aging and annealing study.	142

## LIST OF FIGURES

Figure 3.1: Results of the PBS absorption test (n = 3 for all).	25
Figure 3.2: Representative DSC curves for each material.	26
Figure 3.3: Representative DMA curves for each material. Storage modulus versus temperature (A) and tan delta versus temperature with an inset showing details at the testing temperature and body temperature (B).	28
Figure 3.4: Representative stress-strain curves for each material. Complete stress range for harder material plots (A) and a smaller stress range for softer material plots (B).	30
Figure 3.5: Fatigue-life curves. Acrylates 95BA and 95/0 were too weak to represent on this graph with the minimum stress level of 2.5 MPa. Open arrows indicate runout at 1 million cycles.	32
Figure 3.6: Representative ratcheting curves for 50/45 (A & B), PCU (C & D), and bovine meniscal tissue (E & F) during cyclic tests. Plots show comparison of behavior at 10 Hz (A, C, E) versus 1 Hz (B, D, F).	33
Figure 3.7: Peak cycle compressive strain versus cycle number for 50/45, PCU, and bovine meniscal tissue at 10 Hz (A) and 1 Hz (B). PDMS added for comparison. 50/45 data shown for a cyclic compression test to a peak compressive stress of 40 MPa. PCU and meniscal tissue data shown for cyclic compression tests to a peak compressive stress of 10 MPa.	36
Figure 3.8: Strain recovery data for 50/45 and PCU (n ≥ 3).	38
Figure 4.1: Representative FDM tension monotonic and shear samples.	51
Figure 4.2: Histogram of dogbone sample solid fraction (A). 3D images showing void distribution for grade 95A with solid fractions of 0.9876 (B), 0.9956 (C), and 0.9993 (D). Scale bar represents 1 mm.	53
Figure 4.3: Plot of all 10 quality control tensile monotonic tests on 95A samples. Solid lines represent samples above the 0.99 solid fraction cutoff, dashed lines represent samples below the cutoff.	54
Figure 4.4: Custom dogbone shape used in fatigue tests, all dimensions in millimeters. Samples were approximately 6 mm thick.	61



Figure 4.5: Representative DSC curves for each material. Endothermic reactions shown in the downward direction. Initial heating and cooling (Cycle 1) shown on top with subsequent heating cycle shown below (Cycle 2).	63
Figure 4.6: Representative storage modulus (A) and loss modulus (B) curves for each grade of PCU.	65
Figure 4.7: Representative NMR spectrum of 85A grade, labels correspond to moieties given in Figure 4.8.	66
Figure 4.8: Chemical structure of PCU material, labels correspond to peaks in Figure 4.7.	67
Figure 4.9: Representative FTIR spectra for each grade of PCU for both IM and FDM samples.	68
Figure 4.10: Representative curves for monotonic tension tests at various times points after printing for 75A (A), 85A (B), and 95A (C).	70
Figure 4.11: Average failure strain of FDM samples by grade and time after printing, error bars indicate standard deviation (n = 3 for each grade and time point). No significant differences were found between 2d and 7d time points for any grade.	71
Figure 4.12: Representative FTIR curves of the carbonyl peak of FDM 75A at 10 minutes, 1 hour, and 7 days after printing.	72
Figure 4.13: Representative monotonic tension curves for 75A (A), 85A (B), and 95A (C) as well as representative monotonic compression curves (D). FDM tensile samples show significantly increased failure strain vs. IM samples with no difference in failure stress. Increased HSC leads to significantly increased compressive modulus (p < 0.0001 for all).	74
Figure 4.14: Representative images of tensile tests for IM and FDM varieties of each grade, immediately before sample failure, showing differences in opacity. Strain readings shown in parentheses, units in mm/mm. Failure stress for all samples shown ranged between 51.1 and 56.7 MPa.	76
Figure 4.15: Median plots of shear stress versus extension for each grade and processing method (A). Average maximum shear stress for IM and FDM PCU, error bars indicate standard deviation (n = 6 for each grade and processing method) (B). Increased HSC leads to significantly increased shear stiffness and shear strength (p < 0.0001 for all comparisons). No significant differences in strength or stiffness between IM and FDM samples.	78
Figure 4.16: IM fatigue data based on strain amplitude (A) and median life tensile stress amplitude (B).	80

- Figure 4.17: Peak tensile stress as a function of cycle number for IM samples of each grade lasting between 1,000 and 1,200 cycles. 81
- Figure 4.18: FDM fatigue data shown against IM counterparts for 75A (A & D), 85A (B & D), and 95A (C & D). Plotted against strain amplitude (A, B, C) and against median life stress amplitude (D). FDM 85A and 95A stress-based data (D) show significantly greater x-axis intercepts and lower slopes vs. IM varieties ( $p < 0.0001$  for all). 83
- Figure 4.19: SEM images of fatigue sample fracture surfaces for IM (A) and FDM (B) samples. 85
- Figure 5.1: Image showing crosshatch samples of 95A and EPU40 (A) and notched as well as cylindrical pore and BCC architectures of EPU40 (B). 103
- Figure 5.2: Custom dogbone geometry used in monotonic and fatigue tests. Samples were printed 6 mm thick. The gage section of notched specimens was widened by 2 mm to maintain the same cross-sectional area. 105
- Figure 5.3: CT scan images showing 95A (A) and EPU40 (B) sample gage sections. Scale bar represents 1 mm. 110
- Figure 5.4: Monotonic tension results for 95A crosshatch samples (A), EPU40 crosshatch samples (B), and EPU40 notched and advanced architectures (C). 95A crosshatch samples show significantly reduced failure stress and strain versus solid samples ( $p \leq 0.0135$  for all). EPU crosshatch, EPU-CP, and EPU-BCC samples show significantly reduced failure stress ( $p \leq 0.0274$ ) with no significant difference in failure strain versus solid samples. No significant differences in failure stress or strain for EPU-CIRC or EPU-DIA notched samples versus solid samples. 113
- Figure 5.5: Normalized failure stress of crosshatch samples as a function of porosity. Data points represent the average of porosity and normalized failure stress for each sample group while the error bars represent standard deviation. 114
- Figure 5.6: Monotonic tension results for EPU-37 (A), EPU-CP (B), and EPU-BCC (C) with architecture printed globally versus localized to the gage section only, with and without a perimeter. Localized EPU-37 samples display significantly increased failure strain versus the global variety ( $p \leq 0.0263$  for both). Local EPU-37 samples without a perimeter display significantly reduced failure stress versus both varieties with a perimeter ( $p \leq 0.0043$  for both). 115
- Figure 5.7: CT scan images of EPU40 global crosshatch (A), local crosshatch with perimeter (B) and without (C), cylindrical pore (D), and BCC spherical pore (E) samples at rest and under tensile strain. Strained samples are shown at approximately 50% tensile strain. Scale bar represents 1 mm. 116

Figure 5.8: Fatigue data for solid and crosshatch 95A samples in terms of strain amplitude (A) and median life stress amplitude (B). C shows median life stress amplitude fatigue data after adjusting for crosshatch sample solid fraction percentages. Crosshatch varieties demonstrate significantly decreased x-axis intercept and increased slope for stress-based data (B) when compared to solid samples ( $p < 0.0001$  for all), even when adjusted by solid fraction (C) ( $p < 0.0001$  for all). 120

Figure 5.9: Fatigue data for notched specimens of EPU40 versus solid control in terms of strain amplitude (A) and median life stress amplitude (B). No significant differences in intercept or slope of stress-based data (B) were found for either notched sample versus the solid samples. 123

Figure 5.10: Fatigue data for solid, crosshatch, cylindrical pore, and BCC spherical pore EPU40 samples in terms of strain amplitude (A) and median life stress amplitude (B). C shows median life stress amplitude fatigue data after adjusting for sample solid fraction percentages. Stress-based data (B) shows significantly reduced x-axis intercepts for all architectures ( $p < 0.0001$ ) and significantly increased slope for EPU-37 samples ( $p = 0.0111$ ) when compared to solid samples. When adjusted by solid fraction (C), stress-based data shows no significant difference in slope or intercept for EPU-CP and EPU-BCC samples versus solid samples, however EPU-37 samples still demonstrate significantly increased slope. 125

Figure 5.11: Strain amplitude fatigue data for crosshatch (A), cylindrical pore (B), and BCC spherical pore (C) EPU40 samples with global architecture and a perimeter as compared to samples with architecture localized to the gage, with and without a perimeter. 127

Figure 5.12: Fatigue data for three grades of solid printed PCU and solid EPU40 in terms of strain amplitude (A) and median life stress amplitude (B). All PCU fatigue data obtained from a previous study (Chapter 4). 137

Figure 6.1: Image showing printed sheet stock, laser cut sheet, and final sample. 143

Figure 6.2: Monotonic tension curves of original IM and FDM samples, as well as the new groups for 75A (A), 85A (B), and 95A (C). FDM 200C 85A samples (B) showed no significant difference in failure stress or strain as compared to IM samples. 145

Figure 6.3: Fatigue data for original IM and FDM specimens together with new laser cut FDM samples in terms of strain amplitude (A) and median life stress amplitude (B). No significant difference was found in intercept or slope of LC FDM samples as compared to FDM. 148

Figure 6.4: Representative FTIR plots of oxidized and control PCU samples. Oxidized samples demonstrate a significantly reduced ratio of the  $1256\text{ cm}^{-1}$  peak to the  $1600\text{ cm}^{-1}$  peak as compared to the control samples ( $p = 0.0135$ ). 150

Figure 6.5: Fatigue data for oxidized and control samples in terms of strain amplitude (A) and median life stress amplitude (B). No significant difference between the control and oxidized samples was found in either intercept or slope of the stress-based data (B). 151

## LIST OF ABBREVIATIONS

ABS	acrylonitrile butadiene styrene
BA	butyl acrylate
CLIP	continuous liquid interface production
CM	compression molded
DDDA	1,12-dodecanediol dimethacrylate
DMA	dynamic mechanical analysis
DMPA	2,2-dimethoxy 2-phenylacetophenone
DPS	degree of phase separation
DSC	differential scanning calorimetry
EPU	elastomeric polyurethane
FDM	fused deposition modeling
FTIR	Fourier transform infrared spectroscopy
$^1\text{H}$ NMR	$^1\text{H}$ Nuclear magnetic resonance spectroscopy
HSC	hard segment content
IM	injection molded
MA	methyl acrylate
MMA	methyl methacrylate
PBS	phosphate buffered saline
PCU	polycarbonate urethane
PDMS	polydimethylsiloxane (silicone)
PU	polyurethane
SEM	scanning electron microscopy
$T_g$	glass transition temperature
TPU	thermoplastic polyurethane
3DP	3D printing

## SUMMARY

The use of soft, synthetic materials for soft tissue replacement in load-bearing, orthopedic applications has been largely unsuccessful due to a lack of adequate materials with sufficient fatigue and wear resistance. Silicone was once purported to be suitable for this purpose, and has been used in applications ranging from radial head implants to intervertebral disc replacements. However, the long term results for these devices demonstrated that there was significant room for improvement, with complications including implant fracture, deformation, and wear. More recently, there has been a surge in devices based on polycarbonate urethane (PCU), which has gained traction due to its relative biocompatibility, compliant nature, viscoelastic properties, as well as its durability as seen through preclinical device testing. Despite its promising nature, caution is warranted as the long-term clinical results of PCU devices have yet to be seen. Considering past difficulties, there is a clear need for a better fundamental understanding of the fatigue resistance of soft, synthetic polymers for orthopedic applications. Therefore, the purpose of this thesis was to develop useful processing-structure-property relationships for relevant soft polymers under fatigue loading in order to assist in the use and success of such polymers in load-bearing orthopedic applications. This was accomplished through the use of three specific aims as summarized below.

In the first aim (Chapter 3), various soft biomedical polymers, including PCU and PDMS, were investigated under cyclic compressive loading to develop general relationships between soft polymer structure and cyclic loading performance. Results indicated that polymers such as polycarbonate urethane (PCU), which have adequate

energy dissipation mechanisms as evidenced by tan delta or loss modulus value, resisted fatigue fracture and instead exhibited cyclic ratcheting much like native meniscal tissue. In contrast, polymers devoid of significant dissipation mechanisms, such as silicone (PDMS), typically exhibited fatigue fracture. In the second aim (Chapter 4), solid samples of PCU were 3D printed through a process known as fused deposition modeling (FDM), and then compared to injection molded (IM) controls via monotonic and tensile fatigue tests. Results showed that FDM samples matched or exceeded the performance of IM controls in terms of tensile strength, tensile failure strain, shear strength, compressive behavior, and tensile fatigue behavior. The success of FDM PCU samples was attributed to optimal printing parameters as well as the toughness of PCU which results in lower flaw sensitivity. Finally, in the third aim (Chapter 5), various printed architectures of PCU, as well as a photo-cured, elastomeric polyurethane (EPU), were tested utilizing tensile fatigue tests and compared to solid printed sample controls. In general, both materials proved quite tolerant to the introduced architectures and notches, with the softer EPU material outperforming PCU. Comparison of different notch and pore geometries revealed that notch severity does indeed impact the tensile fatigue performance of elastomeric PUs, and the effect seems largest in the high cycle regime. The study also revealed a geometrical or structural effect for PUs that can significantly impact fatigue results and illustrates the importance of careful sample design. Finally, it was concluded that the EPU material performs on par with thermoplastic PCUs in tensile fatigue despite vastly different printing methods.

# CHAPTER 1

## INTRODUCTION

### 1.1 Background, Motivation, and Significance

Within the biomedical industry, there has been considerable interest for decades in developing suitable synthetic replacements for soft load-bearing tissues such as intervertebral disc, meniscus, and articular cartilage. These tissues are particularly prone to degeneration as an individual ages which can lead to significant impairment and morbidity [1-5]. Unfortunately, current treatment options such as spinal fusion, total disc replacement, and total knee replacement are associated with a host of complications and negative side effects which are often attributed to the altered biomechanics of the joint due to a mismatch in mechanical properties between the implant materials and the tissues they replace [6, 7]. For example, the loss of a flexible joint following spinal fusion can lead to adjacent-segment degeneration in a significant percentage of cases [8]. Total disc replacement has been proposed as an alternative; however, the unnatural motion of current devices, as well as wear debris, is known to lead to facet joint degeneration and even heterotopic ossification, causing fusion of the joint [9-11]. Likewise, total knee replacement has issues which can also be in part attributed to implant materials, including: bone resorption due to stress shielding effects, osteolysis due to bearing surface wear particles, and an overall functional deficit [7, 12, 13]. For applications such as these, it seems a potentially superior approach could be developed in which joint properties and mechanics are restored utilizing a softer material which more closely mimics the natural tissue properties. Table 1.1 lists modulus data for several common implant materials as



compared to native soft tissues and soft synthetic materials such as polycarbonate urethane (PCU) and silicone (PDMS), and illustrates the vast difference in stiffness these materials exhibit. In general, the development of a durable and biocompatible soft material would have many applications in the field of soft tissue replacement. Due to the load-bearing nature of many of the soft tissues in the body, an important consideration when developing replacement materials is the response to cyclic loading and fatigue behavior. Not surprisingly, such behavior of current common implant materials such as cobalt-chrome, stainless steel, titanium alloys, and ultra-high molecular weight polyethylene have been extensively studied. This includes the effects of various microstructures, surface treatments, and fabrications methods, as well as the effects of a physiological environment [14-28].

Table 1.1: Modulus data for common implant materials versus soft tissue [29-38].

Material	Modulus (MPa)
Co-Cr alloys	200,000 - 253,000
Stainless Steel (316)	190,000 - 200,000
Ti-6Al-4V	110,000 - 115,000
PEEK	3,000 - 5,000
UHMWPE	800 - 1,600
PCU (75A - 95A)	12 - 42
PDMS	3
Articular Cartilage	2 - 45
Annulus (tensile)	4 - 25

There have been significantly fewer clinically successful devices based on soft materials. For example, as recently as the late 90's, silicone was touted as a potentially suitable material for the replacement of arthritic joints [39]. However numerous studies since have documented cases of failed implants when silicone is used in hand, foot, wrist,

and cardiac lead applications. The failure of these implants is generally attributed to fracture, compressive deformation, and wear leading to inflammation, arthritis, foreign body response, and loss of function [40-44]. Similar issues with silicone were encountered in the development of the Acroflex lumbar disc replacement (DePuy-AcroMed Inc.). Mechanical failure of the silicone core was observed six months after implantation, ending the clinical trial and prompting a return to the original design utilizing a polyolefin rubber core. Despite the promising results from preliminary fatigue and biocompatibility testing, clinical trials were ultimately stopped with results including: mechanical failure of the polyolefin rubber core, osteolysis attributed to the presence of wear particles, as well as periannular ossification [45-48]. Besides silicone, polyolefin rubbers, and thermoplastic polyurethanes (TPUs), few other compliant materials have documented efforts towards their use in load-bearing orthopedic applications, something also noted by Quigley et al. [49]. Several studies have been published on the use of polyvinyl alcohol as a cartilage substitute, including *in vivo* studies as an artificial meniscus [50], however it has yet to gain the popularity of silicone and TPUs. Learning from the issues that plagued prior compliant devices, a newer generation of soft orthopedic devices has emerged recently utilizing a specific TPU, polycarbonate urethane (PCU).

PCU is one subset of a large family of thermoplastic polyurethanes (TPUs). TPUs are block copolymers, with chains comprised of hard and soft segments. Hard segments typically consist of alternating units of a diisocyanate with a diol chain extender, which join through urethane linkages, while soft segments consist of long, flexible macrodiols [51, 52]. The most popular macrodiols for biomedical use often include ester, ether, or carbonate groups thus yielding polyester, polyether, or polycarbonate urethanes,

respectively. Polycarbonate urethane has become especially popular due to its relative biocompatibility [53-56]. In fact, the development of TPUs for biomedical purposes has largely been spurred by biostability concerns. Early polyester urethanes were found to be susceptible to substantial hydrolytic degradation, prompting a shift towards polyether urethanes. However, polyether urethanes have since been found to be susceptible to substantial oxidative degradation, prompting a shift towards the newest iteration -- polycarbonate urethanes [54, 55]. The biostability of polyurethanes has been well studied, and literature includes results from both *in vitro* and *in vivo* studies, as well as the effects of both static and dynamic loads. The general consensus is that PCU shows significantly greater resistance to biodegradation than both polyether and polyester urethanes [53, 55-64]. It has been shown that static and dynamic loading under oxidative conditions does not exacerbate oxidative degradation for PCU [56, 60, 62], in fact PCU showed only minimal degradation after a 24 day accelerated oxidation test -- which is in contrast to polyether urethanes which showed significant destruction through the bulk of the material [56]. Tests of a PCU acetabular cup liner demonstrated no evidence of biodegradation after 3 years *in vivo* [58], and explanted intervertebral disc devices demonstrated only superficial damage on PCU surfaces after 0.7 to 6.5 years *in vivo* [65]. PCU has even been found to be superior to ultra-high molecular weight polyethylene, a material which is used extensively *in vivo*, in terms of oxidative stability [66]. Despite these results, some researchers still urge caution regarding the use of PCU *in vivo* as biodegradation is still found to occur albeit to a relatively small degree.

When TPU hard segments are present in sufficient concentration under the right conditions, they will aggregate into domains due to thermodynamic incompatibility

between the hard and soft segments, leading to microphase separation. These hard domains, held together by hydrogen bonding and thermodynamic forces, provide physical crosslinks for the amorphous matrix of the soft segments. This morphology gives the TPUs many of their favorable properties including its thermoplastic nature, which greatly simplifies processing when compared to conventional, chemically cross-linked rubbers [51, 52]. While the TPU system may seem straightforward, the morphology and resulting mechanical properties can be tailored through a great number of variables including, but not limited to: hard and soft segment chemistry, structure, molecular weight, hard segment content, fillers, and method of preparation and/or processing [51, 52, 67-89]. Further complicating the matter is the fact that these variables can have very nuanced effects and may not necessarily have independent effects on the resulting material properties. For example, as was shown with PCU, an increase in hard segment content generally leads to an increase in tensile strength, but only to a certain extent and only when the soft segment molecular weight is high enough to prevent phase mixing. If soft segment molecular weight is too low, excessive phase mixing prevents crystallization of soft segment under high loads, but excessive phase separation from high hard segment contents may lead to greater localization of shear stresses [88]. As was also noted by Spirkova et al. [84], these structure-property relationships have been somewhat extensively studied for polyester and polyether urethanes [67-81, 89], but only a relatively modest body of work exists for PCUs [82-89]. Taken a step further, studies on the structure-fatigue properties of PCUs represents a nearly nonexistent subset.

Devices utilizing PCU include the LP-ESP total disc replacement (FH Orthopedics Inc.). The LP-ESP utilizes an outer annulus of polycarbonate urethane surrounding an inner

core of silicone with microvoids, and preclinical tests have demonstrated promising results for the device in terms of fatigue, wear, and biostability. Since 2005, the device has been used in over 2000 cases in Europe, and literature has yet to report a complication due to material wear or fatigue [90-94]. In addition to the LP-ESP, promising results have also been seen with similar PCU-based devices including: Total Posterior Spine [95, 96], Bryan Cervical Disc [97-99], M6 cervical and lumbar discs [100-102], Freedom Lumbar Disc [103], acetabular cups [104-109], meniscal implant [110, 111], a bearing surface in osteochondral implants [112], as well as heart valve replacements [113, 114]. While short-term trials for these devices have been relatively successful, long-term results are largely missing as the push for the use of polycarbonate urethane in orthopedic devices has been a rather recent development [54, 115].

In addition to their favorable biocompatibility and relatively low stiffness, the thermoplastic nature of TPUs makes their processing particularly convenient, especially compared to conventional rubbers. It also makes them ideal candidates for additive manufacturing, or 3D printing, through a process known as fused deposition modeling (FDM). 3D printing capabilities for elastomers would provide obvious benefits to the biomedical field through cheaper, faster, and easier device prototyping and even manufacturing, as well as the potential for more complex geometries and architectures. However, as with any material that is 3D printed, such processing will have implications on the material microstructure and ultimately the mechanical properties, particularly fatigue.

Besides the preclinical testing of devices, little work has been done to characterize and understand the fundamental fatigue responses of synthetic, soft polymers in a

physiological environment. Careful examination of the response to cyclic loading across multiple types of soft materials could provide valuable insights into the design and development of such materials for orthopedic applications. In regards to PCU specifically, it would seem that with the recent surfeit of devices, there would be a documented understanding of the relationship between basic PCU properties and fatigue response. However, this is a largely understudied area. Finally, recent improvements in 3D printing technology, which allow for the feeding of flexible filaments into the extruder head, has improved the ability of printing compliant materials such as PCU. The use of 3D printing would allow for simplified device creation and the ability to incorporate complex architectures, multiple materials, functionally graded materials and internal geometries. All of these capabilities could provide tremendous benefits to the biomedical field, however, the effects of such processing on the resulting fatigue properties must first be documented.

The following research is significant in that it would provide fundamental knowledge useful to a wide array of applications with large markets. As previously discussed, current treatments options for degenerative joints such as spinal discs, knee joints, and hip joints are less than optimal solutions that could potentially benefit from the development of compliant material capable of withstanding *in vivo* loads over the course of a lifetime. From 1998 to 2008, the annual number of spinal fusions performed in the US increased by 137% to nearly half a million. Likewise, the number of hip replacements and knee arthroplasties increased 49% and 126%, respectively. The number of spinal fusions, combined with increasing hospital charges, resulted in a 7.9-fold increase in national expenditure on fusions [116]. Clearly, if a compliant material can be developed to meet the demands of these applications, it has potential for significant economic impact.

## 1.2 Research Aims

The goal of this research is to provide fundamental knowledge pertaining to the use of soft polymers for load-bearing orthopedic applications. Our focus was on the fatigue and cyclic loading responses of relevant biomedical polymers as a function of polymer structure as well as processing method, a largely understudied area in this field. The studies focus largely around PCU due to its promising nature and current use in orthopedic devices. As such, the specific aims of our research were as follows.

### 1.2.1 Specific Aim 1: Develop relationships between polymer structure and compressive fatigue/cyclic loading properties for a broad range of soft, biomedical polymers

The central hypothesis of this aim was that polymer structure will have implications on fatigue resistance and cyclic loading properties. Specifically, we hypothesized that materials with higher energy dissipation, as evidenced by tan delta value, will be more resistant to fatigue fracture and exhibit improved compressive fatigue performance (i.e. higher cycles to failure). For this aim, we compared silicone, PCU, as well as several acrylates with tailored thermo-mechanical properties. In addition, we also included a natural soft tissue, bovine meniscus, for comparison purposes. Each material was characterized through dynamic mechanical analysis (DMA) and differential scanning calorimetry (DSC) to determine thermo-mechanical transition behavior and tan delta values. Such thermo-mechanical transition behavior is indicative of various aspects of polymer structure such as chain mobility, crosslinking, and energy dissipation as functions of temperature, and is used in interpreting fatigue results. Cyclic compression fatigue tests were run on each material under aqueous conditions in a bath to develop fatigue life curves.

This broad study provided the context and a point of reference for our other studies focused primarily on PCU.

1.2.2 Specific Aim 2: Investigate the effects of PCU structure on fatigue performance as well as the effects of 3D printing (FDM) on the mechanical properties and fatigue performance of solid printed PCU

PCU chains are subject to hydrogen bonding, and these bonds are the source of significant energy dissipation under applied load. The degree of hydrogen bonding in PCU is largely affected by hard segment content due to the presence of urethane groups [52, 84, 88]. Therefore our hypothesis was that hard segment content would have implications on the fatigue performance of these materials, specifically, increased hard segment content would result in improved fatigue performance (i.e. higher cycles to failure). For this aim we tested injection molded (IM) PCUs of different hardnesses, created by varying the hard segment content, under cyclic tensile fatigue tests in solution. Fatigue data, as well as thermo-mechanical transition data, provided insights into the effect of these chain interactions on the overall properties of the material. In addition, 3D printing, specifically fused deposition modeling (FDM), is a potentially useful method for the creation of devices and specimens through the process of additive manufacturing. However, the layer-by-layer addition process of FDM raises some obvious, yet unstudied, concerns about the resulting mechanical properties of the part. This is particularly true in the case of fatigue, where inherent voids and imperfections can lead to accelerated destruction of the part under loading. For this aim we examined the mechanical properties and fatigue performance of FDM PCU versus that of IM controls. Our hypothesis was that the layer-by-layer addition process of FDM, and presence of voids, would negatively impact the material's monotonic



failure stress and strain as well as resistance to tensile fatigue. For this aim we tested solid FDM PCU samples in monotonic tension, compression and shear, as well as cyclic tensile fatigue tests under aqueous conditions, and compared the results to IM controls.

### 1.2.3 Specific Aim 3: Investigate the effects of printed architecture on the mechanical properties and fatigue performance of polyurethanes

Besides the creation of custom solid shapes without the need for a mold, additive manufacturing is also valuable for the creation of complex architectures often desired in the biomedical field that would otherwise not be possible through conventional processing techniques. However, the addition of architectures raises some obvious, yet unstudied, concerns about the resulting mechanical properties of the part. This is particularly true in the case of fatigue, where stress concentrations and altered loading states can lead to accelerated destruction of the part under loading. For this aim we examined the mechanical properties and tensile fatigue performance of an array of biomedically relevant architectures as compared to solid printed controls. It was our hypothesis that the printed architectures would negatively impact the material's monotonic failure stress and strain as well as resistance to tensile fatigue, and that increased porosity or notch severity (decreased notched radius or increased notch width) would lead to diminished fatigue performance. For this aim we tested simple crosshatch scaffolds, notched specimens, as well as a couple advanced architectures utilizing a thermoplastic PCU as well as a photo-cured, elastomeric PU. Samples were subjected to cyclic tensile fatigue tests under aqueous conditions and results were compared to solid printed controls.

## **CHAPTER 2**

### **LITERATURE REVIEW**

#### **2.1 Fatigue of Biomedical Elastomers**

When it comes to predicting fatigue performance of engineered components, the approaches typically used for metals and stiff polymers (stress-life, linear elastic fracture mechanics) are generally not always applicable for soft or elastomeric components. The discrepancy is due primarily to the nonlinear behavior and relatively large strains that most elastomeric materials exhibit. Fatigue approaches for elastomeric materials typically rely on strain and strain energy functions [117-120]. Further complicating the matter is the fact that the fatigue performance of elastomers, and most polymers in general, is especially susceptible to common factors well studied in metals such as load history, R-ratio, strain rate, geometry, frequency, temperature, material formulation, and environment [120-122]. There has been a fair amount of work on the fatigue of elastomers and rubbers with most focused on natural rubbers for the tire industry. Effects such as minimum stress, strain crystallization, variable amplitudes, molecular weight, fillers, additives, and temperature have been studied with some papers proposing fatigue life models and investigating damage mechanisms [89, 123-129]. While there has been considerable work on the fatigue of elastomers and rubbers in general, biocompatible elastomers tested in physiological conditions represent only a small subset. This is an important distinction when one considers the sensitivity of polymers to their environment. Currently known soft polymers suitable for biomedical applications generally fit into one of a few categories: polyurethanes, silicones, polyolefin rubbers, acrylates, and others (non-polyurethane

thermoplastic elastomers, etc.) [130-132]. A review of the literature on the fatigue and high-cycle loading response of these polymers, in physiological conditions, turns up a relatively small body of scientific work.

Research on polyurethanes includes that of Chaffin and colleagues who tested various mechanical properties of two commercial PDMS and polyether urethanes, often used in pacemaker and defibrillator leads, after accelerated water exposure. They found a decrease in the molar mass related to the length of time spent in solution and subsequently reduced ultimate tensile strength, toughness, wear, and fatigue resistance properties. The molar mass reduction was attributed to hydrolytic cleavage of the polymer backbone, illustrating the dramatic effect a physiological environment can have on elastomers [133, 134]. In fact, the development of polyurethane materials for biomedical applications is testament to this effect. Initially polyester urethanes were used until it was discovered that the polyester segment was susceptible to substantial hydrolytic degradation *in vivo*. Polyether urethanes (PEUs) were then developed to improve upon the hydrolytic degradation, but were ultimately found to be susceptible to oxidation *in vivo*. Finally, polycarbonate urethanes and PDMS containing PEUs were developed that have proven superior to previous polyurethanes in terms of hydrolytic and oxidative resistance; however, both are still somewhat susceptible to *in vivo* degradation [54, 61, 65, 133, 134]. Based on work from Wiggins et al, who examined the effect of strain rate and polyurethane soft segment chemistry on *in vitro* fatigue resistance of film type specimens, these degradative effects are exacerbated by mechanical loading [56, 135, 136]. In addition to the studies above, several specialized and accelerated tests on polyurethanes, as well as

polyolefin rubbers, have been conducted in physiological conditions for cardiovascular and blood pumping applications [137-145].

In parallel with polyurethanes, cyclic testing in physiological conditions has also been investigated on a few non-polyurethane thermoplastic elastomers (NPUTPEs). The most notable is a polystyrene-polyisobutylene-polystyrene block copolymer often referred to as SIBS. SIBS, which resembles silicone, has proven to be an exceptionally biocompatible and biostable material and is often placed between silicone and polyurethane in terms of stiffness and tensile strength. The fatigue properties of SIBS and a few other NPUTPEs have been investigated using the so-called hysteresis method recently pioneered for polymers by Renz, Ehrenstein, and Altstädt. The method involves tracking changes in hysteresis loops during cyclic loading which reveals changes in dynamic modulus and material damping. It is proposed that these parameters reveal more about irreversible structural changes and damage than conventional fatigue testing methods. Using this method various compositions and architectures of SIBS and other NPUTPEs have been tested, in air as well as in physiological conditions, alongside polyurethane, polyester, and silicone. Their work provides important insights into the relationship between chemical structure, network architecture, chain interactions, hard and soft segment compositions and the resultant cyclic responses. While the results for SIBS seem promising, often outperforming silicone in terms of fatigue resistance, these block copolymers typically exhibit extensive permanent creep under cyclic load attributed to its' thermolabile physical crosslinks [71-73, 146-154]. However, recent work by the same group has shown that carbon black reinforcing of dendritic polyisobutylene-based block copolymers not only improves tensile performance but also results in a reduction of cyclic creep to levels on par

with silicone [153, 155]. While the work is still ongoing, the results so far have provided interesting insights into the fundamental differences in fatigue responses between several materials.

In addition to the research on elastomers for cardiovascular applications, one other study was found which investigated the fatigue of a polyolefin rubber in physiological conditions for dental and orthopedic applications [156]. To the best of the authors' knowledge, the previously mentioned papers represent the bulk of the literature regarding non-device fatigue and high-cycle testing of soft polymers in physiological conditions. Furthermore, within this body of work, the number of papers that sought to develop fundamental knowledge about the correlation between material chemistry, structure, etc. and cyclic loading or fatigue response represents an even smaller subset. As mentioned previously, acrylates have also been touted as potentially suitable polymers for the replacement of soft bodily tissues. While fatigue data in physiological conditions could not be found, their toughness in relation to their chemistry and structure have been well documented in such conditions [132, 157-161]. In addition, their easily tailored nature makes them an attractive material for the investigation of fatigue properties in relation to polymer structure and thermo-mechanical transitions.

Knowing the susceptibility of polymers to factors such as environment, geometry, and R-ratio, it comes as no surprise that many of the fatigue testing standards for elastomers state that standardized test results do not provide correlation with service performance (for example, ISO 4666-1:2010 and ASTM D4482-11). It seems likely then that the preference towards device testing versus standardized elastomer testing is due in part to the difficulties in translating such standardized data to useful predictions for engineered components.

Regardless, the testing of a broad range of soft polymers still allows for relative comparisons and the development of fundamental knowledge useful for materials optimization in fatigue-prone applications. In addition, as was seen in the case of the Acroflex lumbar disc, even seemingly conservative simulated fatigue tests of an actual device are imperfect as the Acroflex still failed *in vivo*. While the relatively new polycarbonate urethane based devices have clinical promise, the implantation history of elastomeric devices indicates that there is a clear need for fundamental knowledge of the fatigue properties of elastomers in physiological conditions.

## **2.2 Fatigue of 3D Printed Polymers**

3D printing capabilities for elastomers would provide obvious benefits through cheaper, faster, and easier device prototyping and sometimes final component manufacturing, as well as the potential for complex geometries and architectures. As with any material that is 3D printed, such processing will have implications on the material microstructure and ultimately the mechanical properties, particularly fatigue. A literature review on the fatigue properties of 3D printed polymers turns up a relatively modest amount of work, especially in regards to printed elastomers, a fact that was also noted by Moore and Williams [162]. Currently, regarding the fatigue of 3D printed polymers in general, there are a few studies on the fatigue of FDM ABS which have largely focused on printing direction and the effect of material mesostructure on mechanical performance [163-165]. In addition, a fair amount of work exists on the fatigue of laser sintered nylons [166-175], which represents a significantly different process than FDM. One paper exists on the fatigue of a photo-cured elastomer printed through material jetting [162], however the authors could not find any work on the fatigue of FDM elastomers.

### **2.3 Fatigue of Polymer Scaffolds & Porous Polymers**

Biomedical polymers are available in both bioresorbable as well as nonresorbable varieties that are more resistant to degradation [176, 177]. The case for the use of pores and architectures for bioresorbable polymers is rather obvious for the application of tissue engineering, where permeability will assist in cell migration and tissue ingrowth and eventual replacement of the scaffold. However, the use of pores and architectures may also be desirable with long-term polymers where permeability or ingrowth for permanent attachment is desired, for example. The published literature contains very little information on the fatigue performance of polymer scaffolds, porous polymers, or polymers with architecture. Work includes that by Evans et al., who investigated the fatigue performance of a variety of surface-porous, hard polymers including polyether-ether-ketone (PEEK) and polycarbonate. Generally, they found a substantial decrease in fatigue performance when surface porosity was introduced, and that the ratio of upper to lower yield points of the material could provide insight as to how large of an impact such defects might have [178, 179]. Hoyt et al. examined the compressive and tensile fatigue of open-cell, porous poly(para-phenylene) scaffolds fabricated through porogen leaching. They found a hundredfold decrease in the tensile endurance limit due to large stress concentrations in their porous architecture [180]. To the best of the authors' knowledge, few studies exist that have investigated the high cycle fatigue performance of porous polymers or polymer scaffolds. The lack of research in this area for polymers is likely due to the significant impact pores and architecture can have on a material's fatigue performance, leading to a preference for stronger materials for permanent applications, such as metals. In contrast with polymers, considerably more work exists examining the fatigue performance of metal

scaffolds and porous metals. For example, several groups have investigated the fatigue performance of porous Ti-6Al-4V. Generally, they have found that the inclusion of pores or architectures leads to a substantial decrease in fatigue strength on the order of approximately 75% [181-189]. Similar work has also been conducted for porous tantalum [190-192].

Studies on the fatigue performance of scaffolds and porous samples of compliant materials, or elastomers, represents a virtually nonexistent subset. From a more fundamental point of view, the effects of pores and architectures on fatigue performance can be seen as simply a notch sensitivity or stress concentration issue. However, the literature also contains very little information on notch sensitivity and stress concentrations effects in elastomers. This fact also was also noted by McNamara et al., who performed tensile fatigue tests on notched dumbbells of both ethylene propylene diene monomer (EPDM) and natural rubbers. They found that fatigue life was directly influenced by the severity of the notch, notch severity diminishes with increasing deformation, and that notch sensitivity is less pronounced for natural rubber than EPDM due to strain crystallization [193]. Monotonic testing of notch effects for rubbery and rubber-modified materials shows generally promising results, with most displaying small, or even negative, notch sensitivity factors [194, 195]. Additionally, for materials exhibiting substantial hysteresis, such as PUs, it has been found that stress concentrations at notches are significantly lessened under dynamic loading leading to superior performance as compared to materials with less hysteresis [196, 197].



## CHAPTER 3

### EFFECT OF POLYMER STRUCTURE ON THE FATIGUE AND CYCLIC LOADING PROPERTIES OF SOFT BIOMEDICAL POLYMERS

#### 3.1 Introduction

Besides the preclinical testing of devices, little work has been done to characterize and understand the fundamental fatigue responses of synthetic, soft polymers in a physiological environment. Careful examination of the response to cyclic loading across multiple types of soft materials could provide valuable insights into the design and development of such materials for orthopedic applications. As such, the objectives of this study are threefold:

1. Examine the fatigue properties and responses to cyclic loading of a range of synthetic polymers with systematically varied thermo-mechanical transitions to develop an understanding of the relationship between these transitions and responses.
2. Understand the response to cyclic loading (creep, recovery, damage accumulation) for the most promising materials from objective 1.
3. Compare the behavior of the synthetic polymers with soft biological tissues.

It is our hypothesis that the thermo-mechanical transition behaviors, which are indicative of various aspects of polymer structure and fundamental to classifying various polymer systems, will have implications on the fatigue performance of these materials. Specifically, materials with higher energy dissipation, as evidenced by tan delta value, will be more resistant to fatigue fracture thus exhibiting improved fatigue performance (i.e. higher cycles to failure). Through these objectives we hope to develop a better

understanding of the link between polymer structure and response to cyclic compressive loading.

## **3.2 Materials and Methods**

### 3.2.1 Materials

PDMS samples were created using the Sylgard 184 elastomer kit (Dow Corning). Methyl methacrylate (MMA), methyl acrylate (MA), butyl acrylate (BA), and 2,2-dimethoxy 2-phenylacetophenone (DMPA) were obtained from Sigma-Aldrich, and used as received. 1,12-dodecanediol dimethacrylate (DDDA) was obtained from Monomer-Polymer and Dajac Labs. Carbothane AC-4085A was obtained from Lubrizol. Bovine meniscus samples were obtained through Animal Technologies, Inc. (Tyler, Texas) and kept frozen until use.

### 3.2.2 Synthesis

PDMS compression samples were prepared by mixing the Sylgard 184 elastomeric base with the curing agent in a 10:1 weight ratio. The mix was degassed in a vacuum oven for 15 minutes prior to being poured into a Teflon block mold. The mold was sealed at the bottom with a Rain-X-coated glass slide. Acrylate compression samples were prepared by first creating solutions of the appropriate monomer ratios. Four compositions were prepared, each using 5% by weight DDDA crosslinker and 0.4% by weight DMPA photoinitiator. The four compositions include: 50% MA with 45% MMA (50/45), 70% MA with 25% MMA (70/25), 95% MA (95/0), and 95% BA (95BA). Each solution was manually mixed in a glass vial before injecting into a Rain-X-coated shell vial (0.5dr shell vial, Fisher Scientific). The shell vials were capped and placed in a UV chamber (model CL-1000L ultraviolet cross-linker,  $\lambda = 365$  nm, energy =  $2000 \times 100 \mu\text{J cm}^{-2}$ ) for

approximately 44 minutes (50/45), 9 minutes (70/25), 5 minutes (95/0), or 12 minutes (95BA) of total time. Polycarbonate urethane (PCU) compression samples were prepared by first drying the Carbothane AC-4085A pellets in an oven at 120°C for 30 minutes. The pellets were then run through a single screw extruder set to 204°C to form them into a cylindrical shape. The cylinders were cut to approximate 1 g increments and placed into a steel mold with 10 mm diameter holes. Compression pins were placed on top of the PCU samples in the mold, and the mold was placed into a hot press (Carver, Model 3851-0) (200°C, 500 lbs pressure per sample, 10 minutes) to form the final samples. Samples for phosphate buffered saline (PBS) absorption, differential scanning calorimetry (DSC), and dynamic mechanical analysis (DMA) were made from 1 mm thick sheets of each material prepared with similar processes as the compression samples.

### 3.2.3 Characterization

#### *3.2.3.1 PBS absorption*

The swelling behavior of each material was evaluated utilizing a PBS absorption test. Samples of each material (approximately 1 mm x 10 mm x 10 mm) were soaked in PBS, after which they were blotted of excess moisture and weighed on a scale ( $W_w$ ). Samples were then dried in a vacuum oven (-15 inHg, 80°C) for 24 hours before being weighed again ( $W_D$ ). Each material was tested for a 24 hour and 1 week soak duration. The water content was calculated as the difference between the wet and dry weights divided by the dry weight, and the average and standard deviations were calculated for each material ( $n = 3$ ).

### *3.2.3.2 Differential scanning calorimetry*

The glass transition temperature ( $T_g$ ) was determined for both dry and wet conditions of each material by DSC (TA Instruments Q100, New Castle, DE) in a nitrogen environment. Disc-shaped samples were weighed prior to testing (average mass between 10 and 15 mg). Wet samples were allowed to equilibrate in PBS for 24 hours at room temperature and were blotted of excess moisture prior to weighing and testing. Samples were equilibrated at a temperature between  $-25^{\circ}\text{C}$  to  $-100^{\circ}\text{C}$ , held isothermal for 3 minutes, and ramped at  $10^{\circ}\text{C}/\text{min}$  to a final temperature between  $75^{\circ}\text{C}$  to  $100^{\circ}\text{C}$ , depending on the expected  $T_g$  of the material. The  $T_g$  was denoted as a second order endothermic transition on the DSC curve and the average and standard deviation was calculated for both wet and dry conditions for each material ( $n = 3$ ).

### *3.2.3.3 Dynamic mechanical analysis*

The storage modulus and tan delta values were determined through a temperature sweep by DMA (TA Instruments Q800, New Castle, DE). Rectangular samples were measured using digital calipers (approximately 1 mm by 5 mm in cross-section) and then loaded into the tensile clamps and tested at a frequency of 1 Hz and strain of 0.1%. Samples were equilibrated at a temperature between  $-40^{\circ}\text{C}$  to  $-140^{\circ}\text{C}$ , held isothermal for 3 minutes, and ramped at  $3^{\circ}\text{C}/\text{min}$  to a final temperature between  $40^{\circ}\text{C}$  to  $140^{\circ}\text{C}$ , depending on the expected  $T_g$  of the material. The storage modulus and tan delta values were plotted as a function of temperature, with the peak of the tan delta curve taken as the  $T_g$  ( $n = 3$ ).

### *3.2.3.4 Compression testing*

Compression tests were utilized to determine the stress-strain behavior of each material. Cylindrical samples of approximately 9.5 mm diameter x 9.5 mm height were

prepared as described and allowed to equilibrate in PBS (Sigma-Aldrich) at room temperature for 24 hours prior to testing. The diameter and height of each sample was measured using digital calipers immediately prior to testing. The tests were performed using an MTS Bionix machine with a 15 kN load cell and each sample was tested in a bath filled with PBS at room temperature. The samples were compressed to 90% strain over 10 seconds utilizing a strain-controlled test. The elastic modulus was calculated for each material as the slope of the initial linear portion of each stress-strain curve ( $n = 4$ ).

#### 3.2.4 Cyclic compression testing

Cyclic compression tests were utilized to screen the fatigue behavior of each material. For these tests, cylindrical samples were used and tested in the bath setup as described for compression testing. Samples were tested in a force-controlled manner at 10 Hz with a lower bound load corresponding to 1 MPa in compression and an upper bound load corresponding to 2.5 MPa to 50 MPa in compression, depending on the stress level of the test. Each material was tested through a range of upper bound stresses to develop a fatigue life curve. Tests were run until failure, defined as a 10% increase in strain from initial value, or until they reached 1 million cycles. While this study considered only meniscal tissue, the 10% increase in strain criteria was chosen based on literature regarding several soft tissue pathologies, such as the increase in meniscal axial strain following partial meniscectomy [198], as well as the correlation between similar changes in intervertebral disc height and back pain scores [199]. The criteria also exceeds the maximum average diurnal variation in articular cartilage strain over a normal day of use [200], supporting the notion that our criteria represent a pathological change rather than physiological. In the interest of consistency, synthetic samples were held to the same failure

criteria, whether this criteria was met through abrupt fatigue failure or cyclic ratcheting. The average number of cycles and standard deviation was calculated for each stress level for each material ( $n \geq 3$ ). In addition to the tests at 10 Hz, tests at 1 Hz were conducted at selected stress levels for 50/45 and PCU in order to elucidate frequency effects.

### 3.2.5 Strain recovery testing

Strain recovery following cyclic tests was examined for PCU and 50/45 by comparing the strain recovery of specimens loaded cyclically versus monotonically. For these tests, cylindrical samples were used and tested in the bath setup as described for compression testing. Cyclic samples were tested in a force-controlled manner at 10 Hz with a lower bound load corresponding to 1 MPa in compression and an upper bound load of 40 MPa (50/45) or 10 MPa (PCU) until the 10% strain increase failure criteria was met. For each cyclic test performed, a matching monotonic test was performed on a new specimen in a displacement-controlled manner to the maximum strain reached during the cyclic test. Following the tests, samples were stored in saline at room temperature and sample height was recorded at regular time intervals to compare the strain recovery of monotonic versus cyclically loaded samples. Due to the slightly differing strain levels between cyclic-monotonic pairs, normalized strain recovery is presented as the difference between the maximum strain reached during testing and remaining strain divided by the maximum strain ( $n \geq 3$ ).

### 3.2.6 Bovine meniscal tissue testing

Tests on bovine meniscal tissue included DSC, DMA, monotonic stress-strain, and cyclic compression testing. For DSC, disc-shaped samples (average mass between 10 and 15 mg) were cut from a peripheral section of the meniscus. Samples were hydrated for 30

minutes in PBS and then blotted of excess moisture prior to weighing and testing. Tests were conducted as described for the synthetic materials between temperatures of  $-15^{\circ}\text{C}$  to  $75^{\circ}\text{C}$  ( $n = 5$ ). For DMA, the peripheral surface of the meniscus was first trimmed to create a flat and clean surface. The DMA samples (approximately 2 mm x 6 mm x 25 mm) were then cut circumferentially from along the new peripheral surface. Samples were hydrated for 30 minutes in a water bath, then coated in petroleum jelly to delay drying during testing. Samples were then measured and tested as described for the synthetic materials between temperatures of  $5^{\circ}\text{C}$  and  $80^{\circ}\text{C}$  ( $n = 4$ ).

Monotonic stress-strain and cyclic compression testing samples were harvested utilizing a 10 mm diameter punch. Samples were punched in the axial orientation of the meniscus, near the periphery, following which the tibial and femoral surfaces were trimmed to make flat cylindrical samples (approximately 8 mm tall x 10 mm diameter). Samples were allowed to hydrate in PBS for a minimum of 30 minutes, following which they were measured and tested in an MTS Bionix machine as described for the synthetic materials ( $n = 4$  for monotonic,  $n \geq 5$  for each stress level of cyclic testing). In addition to the cyclic tests at 10 Hz, cyclic tests at 1 Hz were conducted at 10 MPa for the meniscal tissue in order to elucidate frequency effects.

### **3.3 Results**

#### **3.3.1 Characterization**

##### ***3.3.1.1 PBS absorption***

The water content is reported for all synthetic materials in Figure 3.1. With the exception of PCU, results indicated that the water content for all materials stabilizes within

24 hours of being placed in PBS. The acrylates showed a small increase in water content as the proportion of methyl acrylate increases relative to methyl methacrylate.

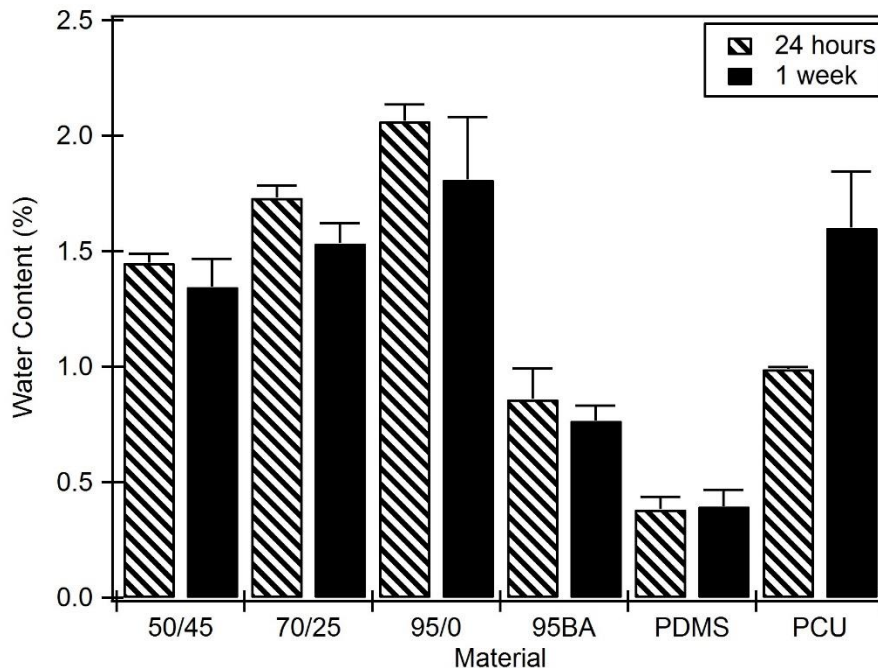


Figure 3.1: Results of the PBS absorption test (n = 3 for all).

### 3.3.1.2 Differential scanning calorimetry

Figure 3.2 shows representative DSC curves for the tested materials, Table 3.1 shows tabulated glass transition temperatures for each material calculated from both DSC as well as DMA results. The methyl-acrylate-containing materials showed a marked decrease in  $T_g$  of approximately 5-10°C following a 24 hour soak in PBS, while 95BA and PCU were relatively unaffected. The DSC machine was unable to cool below the estimated  $T_g$  of PDMS (-125°C [201]); however, the results still indicated a lack of transition over the range of temperatures tested. Results for PCU indicated two transitions, one around -28°C and the other at approximately 50°C. The remaining synthetic materials demonstrated



a single glass transition over the temperature ranges tested. Results also indicated that bovine meniscal tissue demonstrates stable behavior over the temperature range tested as the prominent features of the plot are attributed solely to the water content and eventual drying of the samples.

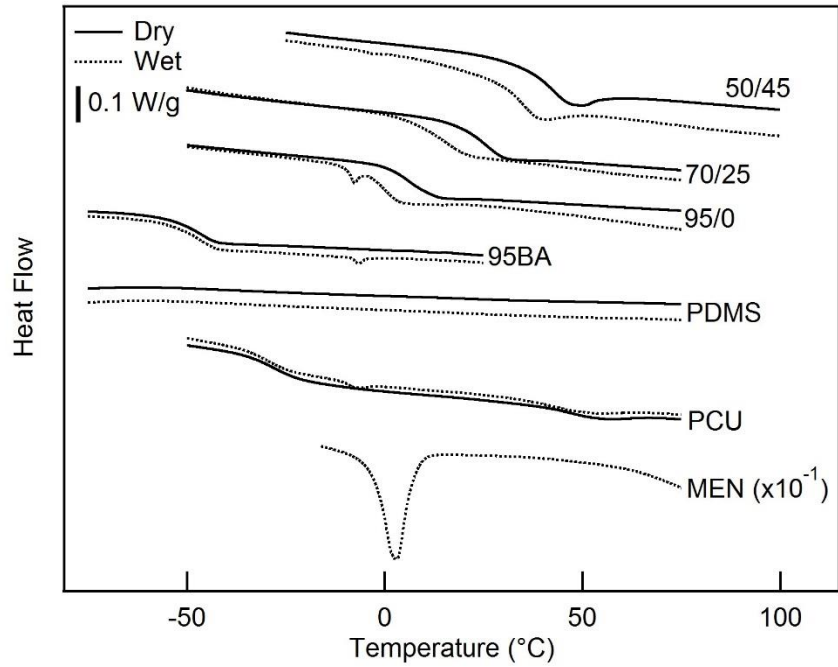


Figure 3.2: Representative DSC curves for each material.

Table 3.1. Glass transition temperature determined from DMA and DSC.

Material	T <sub>g</sub> <sup>†</sup>					
	Tan Delta Peak		DSC - dry		DSC - wet	
	Average	STD	Average	STD	Average	STD
50/45	63.6	1.0	42.3	0.8	35.5	0.4
70/25	43.6	0.6	25.8	0.2	15.8	0.3
95/0	25.8	0.3	5.2	0.8	0.4	0.9
95BA	-30.4	1.4	-46.7	0.8	-46.5	0.9
PCU	-9.7	0.6	-28.0	0.4	-29.9	0.4
PDMS	-117.5	0.3	ND	ND	ND	ND
† n = 3						

### 3.3.1.3 Dynamic mechanical analysis

Figure 3.3 shows representative storage modulus and tan delta curves for the tested materials. The  $T_g$  determined from the tan delta peak consistently reported 16-22°C higher than dry DSC, an expected result due to fundamental differences between DMA and DSC [157]. Based on the tan delta peaks, the materials exhibit a large spread of  $T_g$  from -117.5°C (PDMS) to 63.6°C (50/45). The acrylates tended to exhibit very abrupt transitions, while PDMS and PCU showed relatively broad transitions. The acrylates showed an expected decrease in  $T_g$  and increase in peak tan delta as the proportion of methyl acrylate is increased relative to methyl methacrylate as expected based on the  $T_g$ 's of the two components and using the Rule of Mixtures [202]. Of particular importance is that, at room temperature and body temperature, the materials exhibit a variety of states including glassy, viscoelastic, and rubbery. Stable behavior for the bovine meniscal tissue is confirmed with DMA results, which demonstrate a lack of transition for the tissue over the temperature range tested. The slight upturn in storage modulus for meniscal tissue is attributed to gradual drying of the sample as the test proceeded. As was demonstrated by Adams and colleagues, the value of rubbery modulus for the meniscal tissue presented in Figure 3.3 may not necessarily represent the intact stiffness *in vivo* due to the disruption of the collagen network [203]. Rather, DMA was employed to investigate the presence of thermo-mechanical transitions near body temperature.

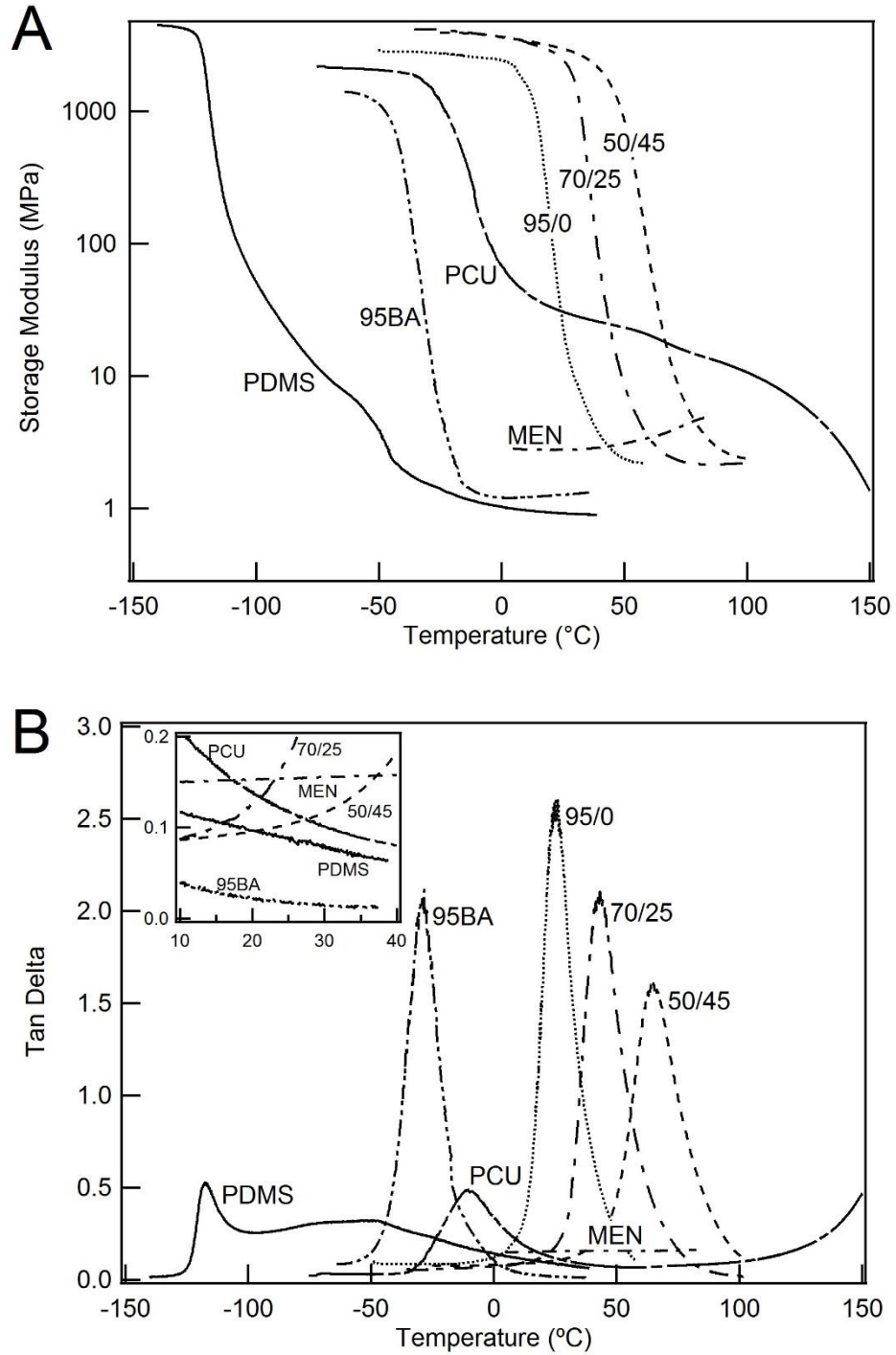


Figure 3.3: Representative DMA curves for each material. Storage modulus versus temperature (A) and tan delta versus temperature with an inset showing details at the testing temperature and body temperature (B).

### 3.3.1.4 Compression testing

The synthetic materials tested showed a wide array of stress-strain behaviors and elastic moduli. Moduli for all materials are tabulated in Table 3.2 and range from 2.3 MPa (95BA) to 1.9 GPa (50/45). Representative curves for each material are shown in Figure 3.4. The acrylates showed an expected decrease in elastic modulus as the proportion of methyl acrylate is increased relative to methyl methacrylate. The two stiffer acrylates, 50/45 and 70/25, showed distinct yielding points at a strain of approximately 0.08-0.1 mm/mm while the remaining materials displayed nonlinear, elastomeric behavior. The initial modulus for bovine meniscal tissue is approximately on par with that of PCU, however the samples exhibited failure typically between 10 and 20 MPa.

Table 3.2. Moduli data.

Material	Average Modulus (MPa) <sup>†</sup>	Standard Deviation
50/45	1900	300
70/25	550	140
95/0	6.7	0.3
95BA	2.3	0.1
PCU	27.3	0.4
PDMS	2.9	0.2
MEN	37.0	11.0
<sup>†</sup> n ≥ 3		

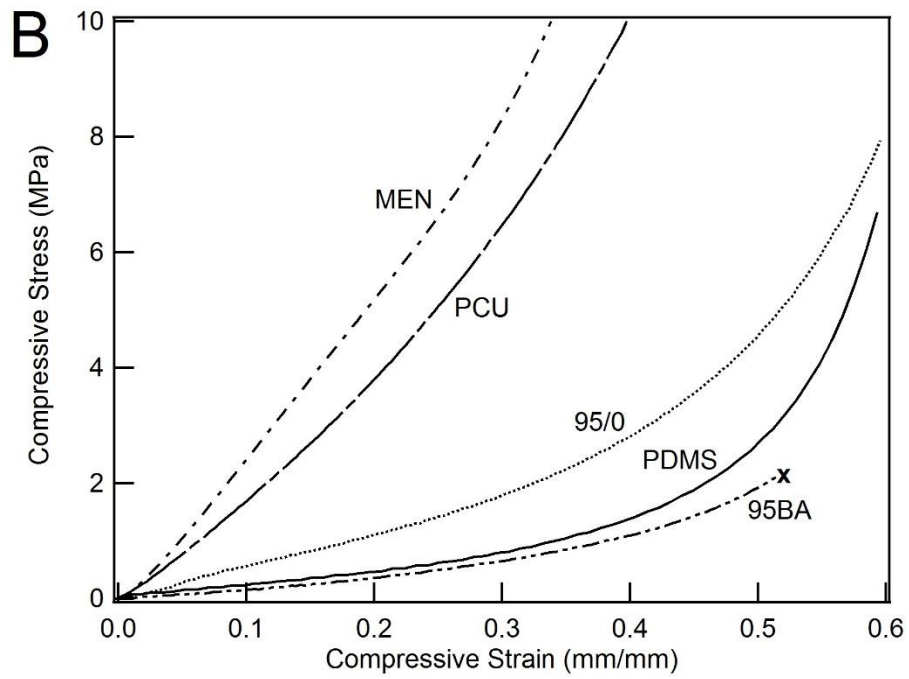
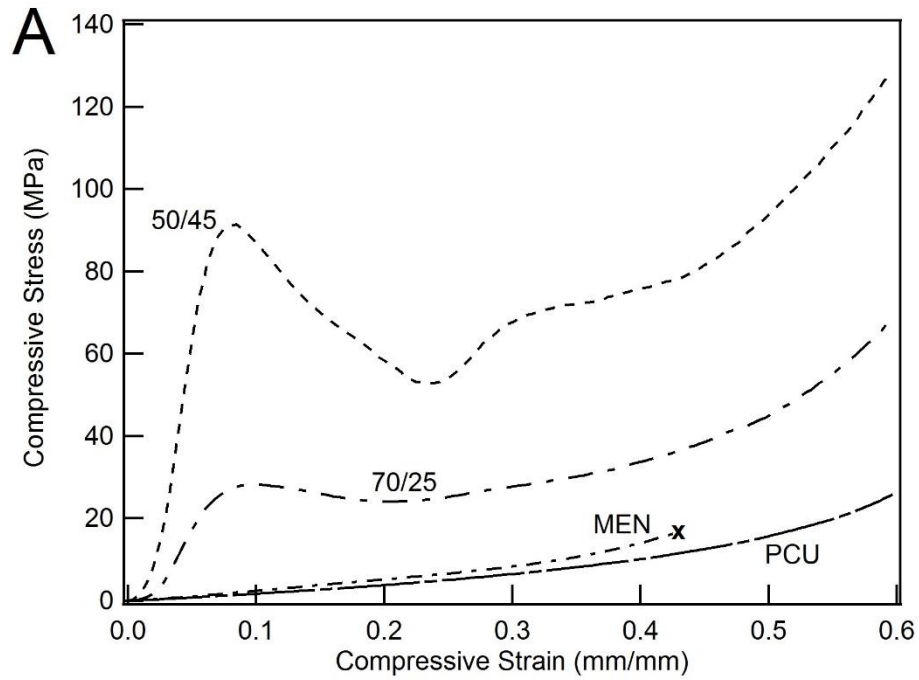


Figure 3.4: Representative stress-strain curves for each material. Complete stress range for harder material plots (A) and a smaller stress range for softer material plots (B).

### 3.3.2 Cyclic compression testing

Fatigue life curves are shown in Figure 3.5. The five materials shown (50/45, 70/25, PDMS, PCU, MEN) demonstrated classical stress-life behavior even though the “failure” mechanisms differ amongst the polymers. The remaining two materials (95/0, 95BA) were unable to be shown on the plot due to not being able to withstand cyclic tests at the threshold stress level considered in this study (2.5 MPa). Samples of 95BA routinely fractured within the first cycle, whereas 95/0 samples ratcheted so abruptly that the testing machine was unable to ramp up to the proper load level for valid results. With the exception of the runout tests stopped at 1 million cycles, PDMS tests ended with an abrupt fracturing of the sample. The remaining materials (50/45, 70/25, PCU, MEN), which are in a viscoelastic state at the testing temperature, displayed a cyclic ratcheting type failure without fracture of the sample. For the acrylates, as the proportion of methyl acrylate increases relative to methyl methacrylate, there is a clear trend towards an increase in cyclic ratcheting.

Figure 3.6 shows representative ratcheting curves for 50/45, PCU, and MEN during cyclic testing at both 1 Hz and 10 Hz. Figure 3.7 shows representative curves of the peak strain reached during each loading cycle as a function of cycle number for these same materials and illustrates the overall rate of ratcheting. As the samples ratcheted in cyclic testing, 50/45 maintained the initial slope of the stress-strain curve, PCU displayed a slight flattening effect, and MEN showed an increase in slope (Figure 3.6). During 10 Hz testing, 50/45 displayed a distinct region of rapid creep response preceded and followed by periods of slower creep response (Figure 3.7). MEN and PCU displayed a rapid creep response initially that quickly leveled out for the remainder of the test (Figure 3.7). Both 50/45 and

PCU demonstrated slower ratcheting on a per cycle basis with the 1 Hz testing versus 10 Hz, which is in contrast to MEN, which demonstrated faster ratcheting per cycle at the 1 Hz frequency versus 10 Hz (Figure 3.6).

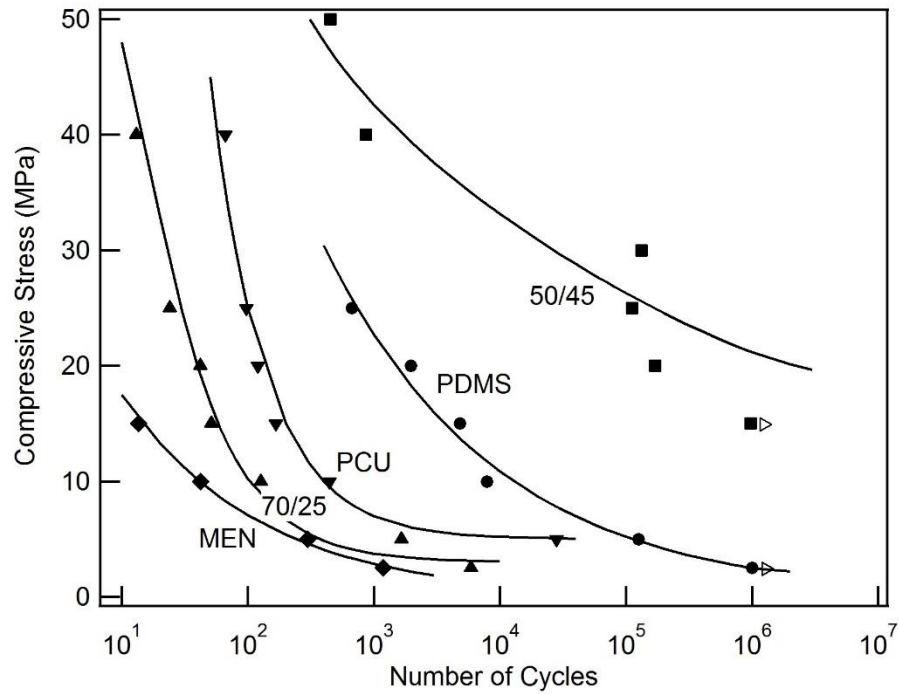


Figure 3.5: Fatigue-life curves. Acrylates 95BA and 95/0 were too weak to represent on this graph with the minimum stress level of 2.5 MPa. Open arrows indicate runout at 1 million cycles.

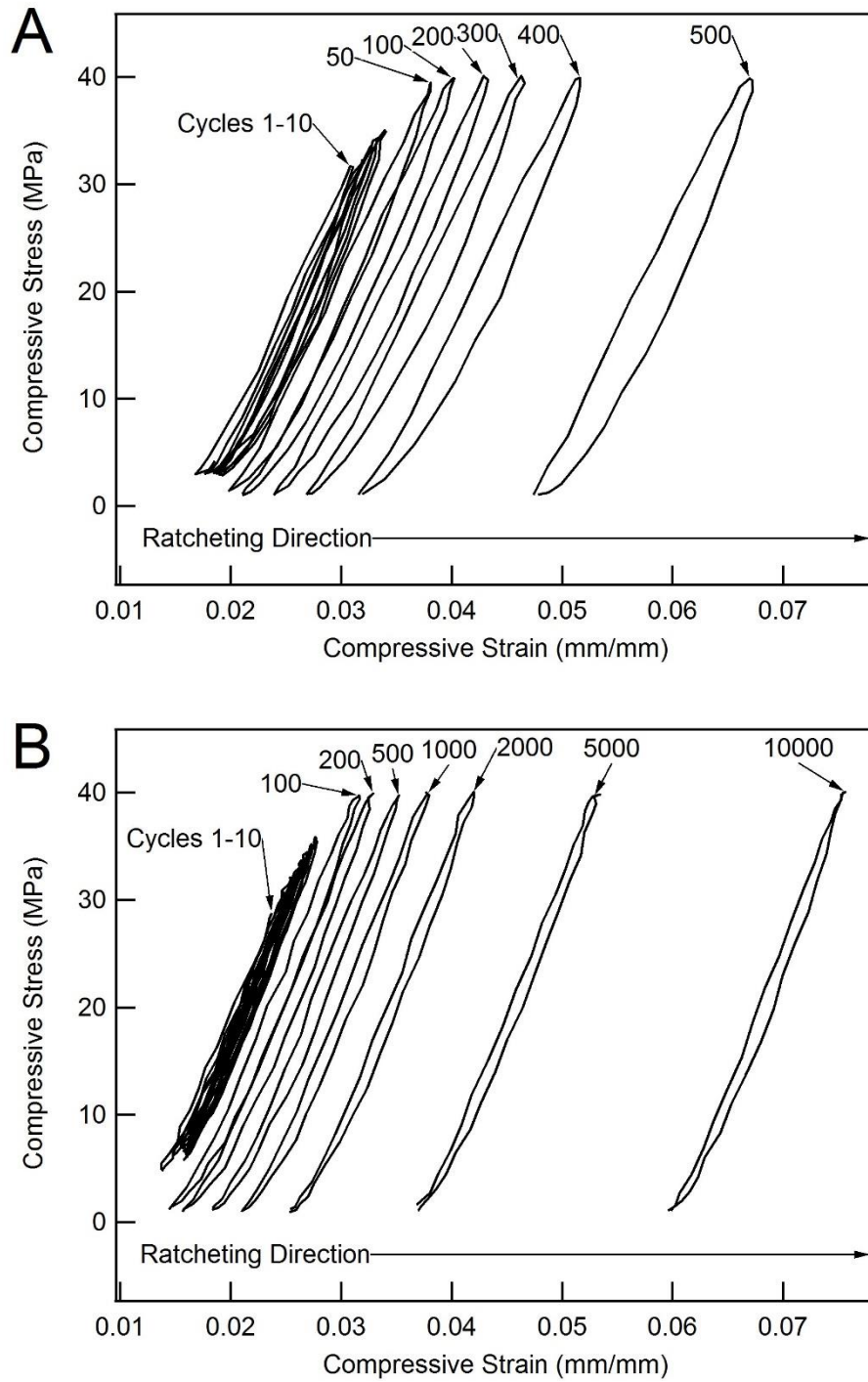


Figure 3.6: Representative ratcheting curves for 50/45 (A & B), PCU (C & D), and bovine meniscal tissue (E & F) during cyclic tests. Plots show comparison of behavior at 10 Hz (A, C, E) versus 1 Hz (B, D, F).



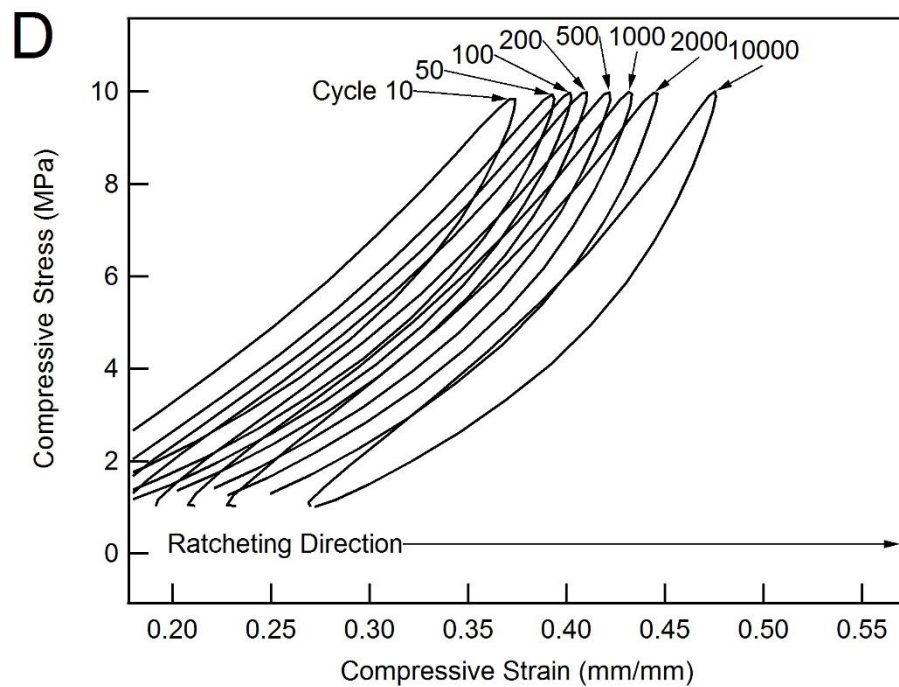
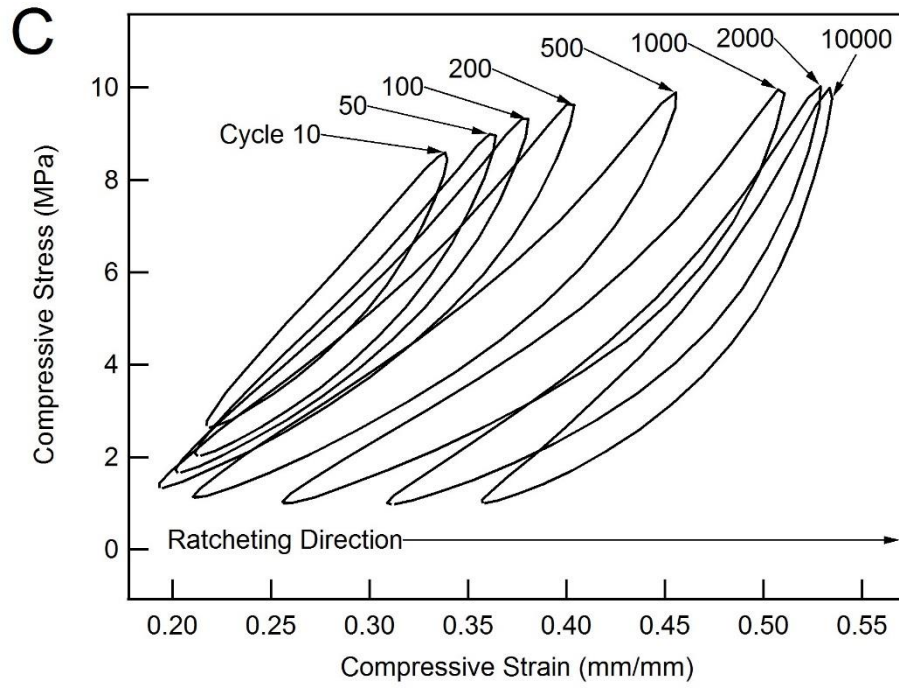


Figure 3.6: Continued

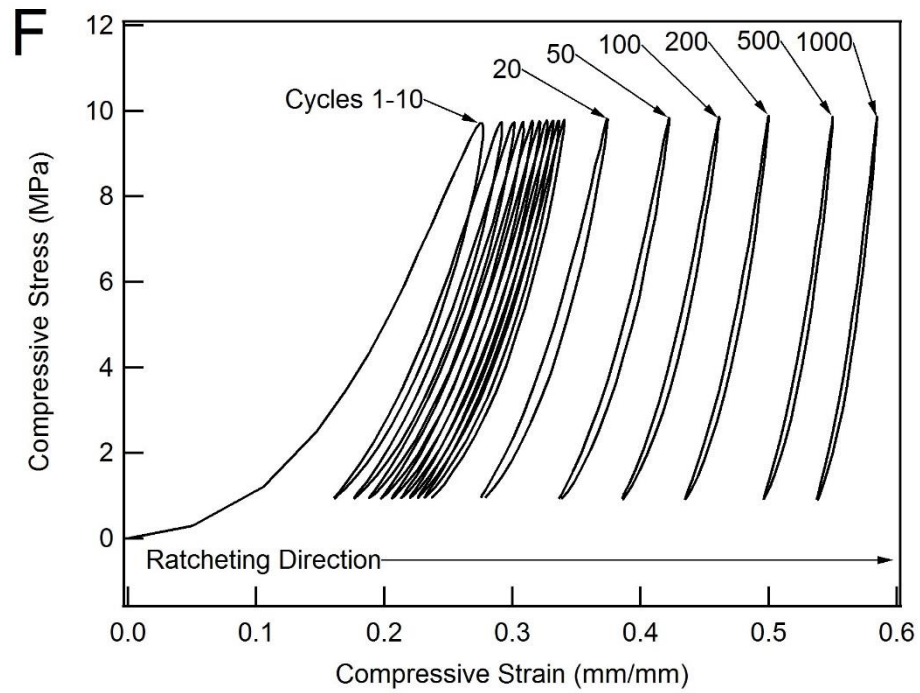
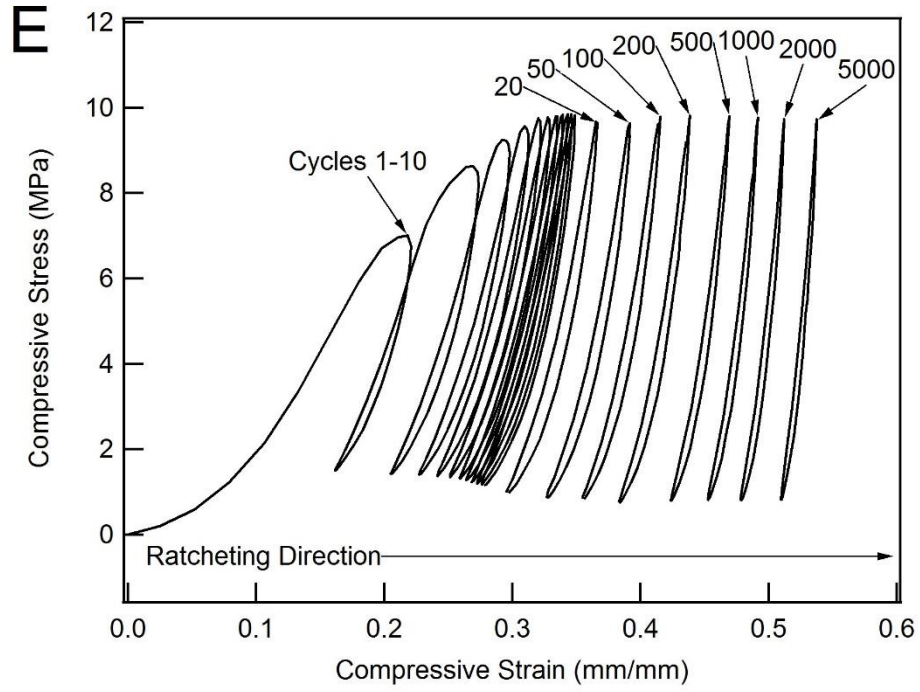


Figure 3.6: Continued

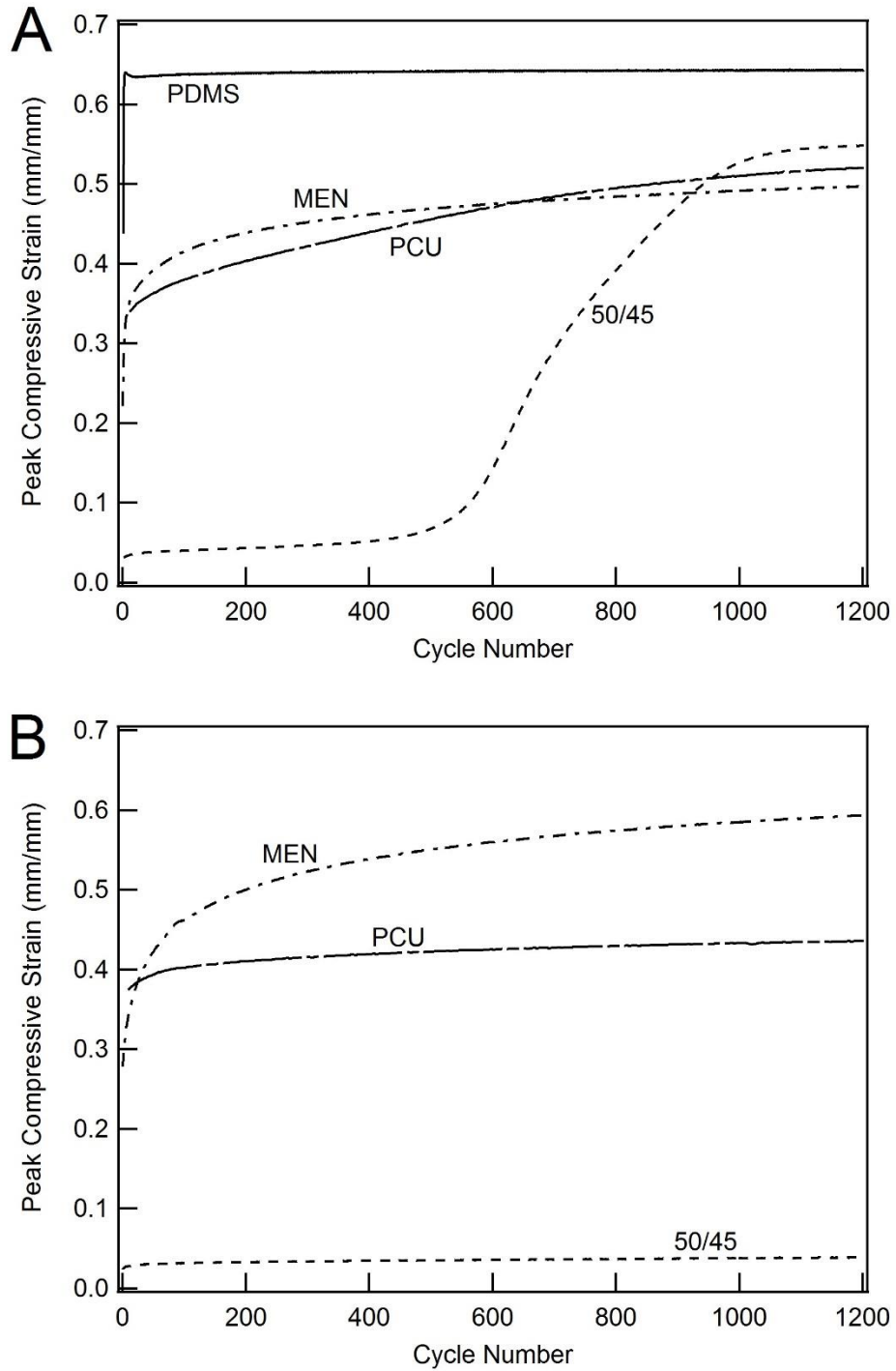


Figure 3.7: Peak cycle compressive strain versus cycle number for 50/45, PCU, and bovine meniscal tissue at 10 Hz (A) and 1 Hz (B). PDMS added for comparison. 50/45 data shown for a cyclic compression test to a peak compressive stress of 40 MPa. PCU and meniscal tissue data shown for cyclic compression tests to a peak compressive stress of 10 MPa.

### 3.3.3 Strain recovery

Strain recovery results for 50/45 and PCU are shown in Figure 3.8. As mentioned, cyclic tests were run until the 10% additional strain criteria was met, with matching monotonic tests then performed to an equal maximum strain. This corresponded to compressive strains of approximately 0.20 mm/mm for 50/45 and 0.45 mm/mm for PCU. As seen in Figure 3.8, PCU samples immediately recovered over 90% of the maximum strain reached during testing with cyclic samples lagging slightly behind monotonically loaded samples. However, both monotonic and cyclic PCU samples approach a full recovery at a similar rate. 50/45 samples showed a much less pronounced initial strain recovery versus PCU, again with the cyclic samples lagging slightly behind the monotonically loaded samples. As with the PCU samples, the monotonically and cyclically loaded 50/45 samples demonstrated similar recovery rates following the initial unloading.

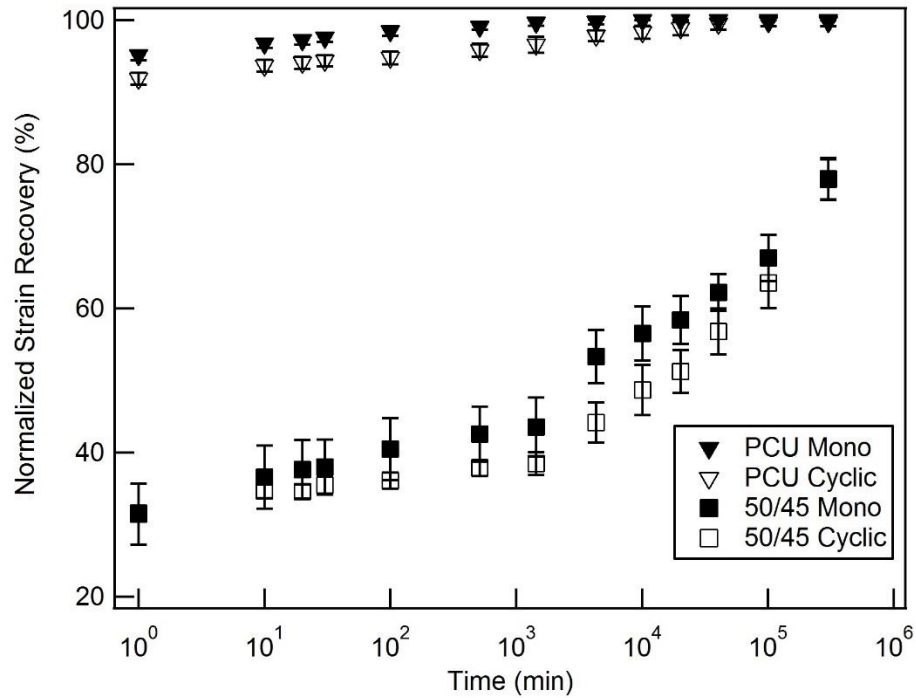


Figure 3.8: Strain recovery data for 50/45 and PCU ( $n \geq 3$ ).

### 3.4 Discussion

The fatigue of materials is a complex process that differs at macroscopic and microscopic levels depending on material type, loading profile, and environmental conditions. Native materials in the human body are subjected to continual cyclic stresses and depending on the function of the material and the level of the stresses, the human body can sometimes counteract cyclic loading and fatigue. Tissues such as bone and muscle are known to be very effective at repairing fatigue damage [204-206]. Whereas other tissues such as spinal disks, cartilage, and meniscal tissue are generally thought to be challenged by fatigue or even monotonic damage leading to degradation, pain, and eventual failure [1, 4]. These soft tissues are designed to primarily absorb and manage cyclic compressive

loads transferred throughout the body. In addition to fatigue damage, repeated compressive loads can lead to acute changes in the thickness of the material even throughout a day of use [200], and over chronic timeframes, lead to severe thinning and complete loss of capacity to support necessary physiological loads. Although tissue engineering holds promise to rebuild damaged tissues by the use of cell scaffolding, in some instances, the severity of cyclic loading profiles and the need for instant load bearing capacity will challenge this approach. Moreover, continual advancements in the chemistry, synthesis, and toughness of synthetic polymers raises the question: Can synthetic soft polymers eventually be designed to match or outperform natural tissues over a relevant timeframe?

Here we have aimed to evaluate and understand the fundamental cyclic compressive behavior of various soft synthetic polymers that have potential for replacing the function of degraded soft tissues within the human body. We hypothesized that thermo-mechanical transitions in polymers would have implications on their performance under cyclic compressive loading, and our results show trends that support this hypothesis. Our first observation is that classic fatigue fracture is expected under cyclic loading (even under pure compressive loading) when the material has an insufficient dissipation mechanism at the testing temperature. The tan delta plot (Figure 3.3B) can be used to assess the relative dissipation mechanisms amongst the materials, though it is worth noting that the DMA data presented in Figure 3.3 is representative of dry samples, whereas the cyclic compression testing was performed in solution. Water uptake has been shown to cause shifts in tan delta peaks as well as decrease peak values [207]; however, this effect is likely small due to the demonstrated low water uptake of materials used in this study and thus should not alter the following overall relationships that will be discussed. At the testing temperature (room

temperature -- approximately 23°C), one can see the relative order of tan delta values, from highest to lowest, is as follows: 95/0, meniscal tissue, 70/25, PCU, 50/45, PDMS, and 95BA. The materials with the two lowest tan delta values, PDMS and 95BA, were the only materials to exhibit classic fatigue fracture during cyclic loading. 95BA, with a tan delta value of 0.02 at 23°C, was unable to withstand a single cycle at the lowest stress level for our cyclic tests; as a result 95BA is not shown on the fatigue life plot (Figure 3.5). PDMS, having a higher tan delta of 0.09 at 23°C, performed better relative to 95BA under our cyclic testing protocol. Despite the relative improvement, PDMS still exhibited fracture, yielding the fatigue life curve shown in Figure 3.5. The comparison between 95BA and PDMS is of particular interest due to their nearly identical elastic modulus values and yet different tan delta behaviors. 95BA exhibits a relatively large tan delta peak near -30°C which quickly dissipates to the smallest tan delta value, among our tested polymers, at room temperature. This would obviously indicate a dissipation mechanism that is relatively sensitive to temperature when compared to PDMS, which displays a smaller tan delta peak but retains a higher tan delta value over a much broader range of temperatures.

Continuing along the trend of increasing tan delta values at the testing temperature brings one to a second observation: the presence of a sufficient dissipation mechanism within the material results in a toughening of the material, preventing fracture during cyclic loading. No fracturing was observed during cyclic tests of 95/0, meniscal tissue, 70/25, PCU, or 50/45. Instead, testing on these samples was ended when they reached a 10% increase in strain under peak cycle loads compared to initial values. This observation is supported by the strain recovery tests on 50/45 and PCU shown in Figure 3.8. Within the timeframe of this study, the PCU samples made a full recovery of the residual strain after

both monotonic and cyclic tests. Likewise, 50/45 samples display a trend towards full recovery, albeit at a much slower rate. In addition to the strain recovery tests, the hysteresis curves shown in Figure 3.6 indicate that the samples maintain the slope and shape of their loading curves throughout testing. Taken together, these results indicate that minimal permanent damage has occurred during the cyclic testing protocol. Our observations regarding the relationship between dissipation mechanisms and fatigue fracture are in general agreement with several previously published studies [208-210]. While these materials exhibited similar behavior under cyclic compressive loading, the mechanisms behind their toughness likely differ. The toughness of polycarbonate urethanes is primarily attributed to hydrogen bonding between hard segments as well as between hard and soft segments. In fact, the hard segment content, and consequently degree of hydrogen bonding, has been found to be directly related to the material's monotonic toughness [84, 88]. Conversely, for the acrylates, toughness is attributed to the onset of their glass transition. The relative motion, stretching, and disentanglement of chains near the material's glass transition allows for the dissipation of energy [132, 159, 160]. In contrast to the synthetic materials, the meniscal tissue demonstrates vastly different behavior at the molecular level. The viscous nature of such tissue has been attributed to its' high water content (63-75% [211]), which flows under applied stresses and is resisted by the negatively charged glycosaminoglycans contained within the matrix, dissipating energy of dynamic loading [212].

As a corollary to our second observation, our third observation is that the presence of sufficient dissipation mechanism within a material to prevent fracture will result in ratcheting under pure cyclic compression and a continued increase in mean strain. As stated



earlier, the materials with higher tan delta values at the testing temperature exhibited a ratcheting type failure. Taken a step further, Figure 3.5 indicates that the materials with the highest tan delta values tended to ratchet the fastest. At the testing temperature, one can see that 95/0 has a tan delta value around 2.0, at least an order of magnitude larger than the remaining materials. As a result, 95/0 could not be shown on Figure 3.5 due to the fact that the samples ratcheted so abruptly that the testing machine was unable to reach the proper load levels to provide valid results. Continuing from left to right across Figure 3.5 yields meniscal tissue, 70/25, PCU, and finally 50/45, which also corresponds to decreasing tan delta values at the testing temperature.

The relationship between dissipation mechanisms and cyclic ratcheting leads us to our last observation, which is that the bovine meniscal tissue demonstrated nearly identical ratcheting behavior, and a lack of fatigue fracture, as our toughened polymers. This observation is illustrated by the curves shown in Figure 3.7, which are representative curves depicting peak strain as a function of cycle number for meniscal tissue, PCU, and 50/45. The meniscal tissue displays a slightly more abrupt ratcheting response than that of PCU, whereas 50/45 is a bit more gradual. It is important to note that the abrupt portion of the ratcheting curve for 50/45 shown in Figure 3.7A was deemed to be a temperature effect. Tests utilizing thermocouples embedded in 50/45 samples revealed an exponential increase in sample temperature corresponding to the abrupt ratcheting behavior, an effect that was only observed at 10 Hz and not at 1 Hz. This temperature increase occurred without detectable changes in the bath temperature due to the large thermal mass of the bath relative to the sample. Considering that increases in temperature from room temperature would put 50/45 closer to its' tan delta peak and  $T_g$ , this result is not surprising. While loading at 10

Hz may not be as physiologically relevant as loading at lower frequencies, this effect does illustrate the importance of the stability of the material response near the temperature of its' intended use. Based on our observations, had the cyclic tests been conducted at body temperature (roughly 13°C higher than room temperature), it would be expected that both 50/45 and 70/25 would ratchet significantly faster, both being softer and closer to their tan delta peak. PDMS and 95BA would have exhibited marginally lower tan delta values, possibly making them even more susceptible to fracture under cyclic load. PCU would also exhibit a decreased tan delta value, however the effect on results would be small due to the relatively stable behavior of PCU near this temperature (Figure 3.3A & B). Likewise, the bovine meniscal tissue exhibited remarkably flat tan delta behavior from 5°C to 80°C, which is perhaps an important characteristic of natural load-bearing tissues where small temperature fluctuations may occur. As a result, we would expect the cyclic loading results at temperatures near body temperature to be similar to those presented in this study for both PCU and meniscal tissue.

In general, the meniscal tissue and toughened polymers exhibit similar ratcheting behavior under cyclic loads; however, the effect of frequency differs amongst meniscal tissue, PCU, and 50/45. This effect is illustrated in Figures 3.6 and 3.7. As discussed, 50/45 undergoes a period of abrupt ratcheting at 10 Hz due to thermal effects, an effect that does not occur at slower frequencies. The increased temperature leads to an exponentially increasing tan delta value and decreasing modulus, which explains the drastic increase in ratcheting rate. Likewise, PCU displays an increase in overall ratcheting rate with an increase in loading frequency (Figure 3.6C & D), despite the fact that a temperature increase would lead to a tan delta decrease. It is postulated that this effect is due to a

decreasing modulus as well as diminished time for strain recovery between cycles at higher frequency testing, an effect that has been documented for thermoplastics [213, 214]. Finally, unlike PCU and 50/45, the bovine meniscal tissue displays an apparent increase in ratcheting rate with a decrease in loading frequency. Due to the high water content of meniscal tissue, it is postulated that this effect is due to the increased time under load causing more fluid to flow from the sample per cycle. This result is on par with previous studies, which have found that both articular cartilage and meniscal tissue exhibit larger hysteresis loops and peak strains at slower frequencies of loading, an effect that would lead to faster cyclic ratcheting [212, 215, 216]. Careful examination of Figure 3.6E & F also indicates that the 1 Hz loading results in a lower dynamic modulus than the 10 Hz loading for meniscal tissue, an effect that was also documented in previous studies and attributed to the buildup of interstitial pressure under more rapid loading [212, 215, 216]. This effect is credited for not only protecting the tissue from damage, but also enabling it to support and redistribute the wide array of loadings it may encounter [216, 217]. While the viscoelastic nature of meniscal tissue has been documented before [211, 212, 218-224], the authors were unable to find studies documenting the cyclic ratcheting and fatigue behavior of meniscal tissue under physiological loads or in the high cycle regime.

### **3.5 Conclusions**

We have investigated the fatigue properties and general response to cyclic loading of a range of soft, synthetic polymers with systematically varied thermo-mechanical transformation behavior. The following are the conclusions of the work.

1. Classic fatigue fracture under cyclic loading occurs when the polymer is devoid of a dissipation mechanism at the test temperature. Fatigue fracture was

experienced by PDMS and 95BA, both of which have little dissipation on their thermo-mechanical transition curve at the testing temperature. The fatigue fracture of PDMS followed a classic stress life curve.

2. Introduction of a dissipation mechanism, as evidenced by the thermo-mechanical transition behavior at the test temperature, can prevent damage due to cyclic loading and significantly toughen a soft polymer. Materials with sufficient dissipation mechanisms did not experience fatigue fracture under cyclic compression in both the low cycle and high cycle regime.
3. A polymer with sufficient dissipation mechanism to circumvent fatigue fracture experiences cyclic ratcheting during pure compression fatigue, resulting in continued increase in the compressive mean strain in the sample without fracture.
4. Bovine meniscal tissue display nearly identical ratcheting behavior, and lack of fatigue fracture, under cyclic compressive stresses as the toughened polymers indicating that such polymers may have potential as artificial soft tissue.

Potential limitations of this study includes the use of meniscus samples that were cut and isolated from their native surrounding tissue. Doing so allowed the use of samples of the same geometry for the sake of direct material comparisons; however, this may also have affected native tissue properties due to the sample's unconfined nature and simplified loading state. Additional limitations include the accelerated testing frequency of 10 Hz and the failure criteria of 10% additional strain. As discussed, testing frequency can have significant effects on fatigue results that differ amongst materials, and defining a point of failure for materials that exhibit extensive ratcheting can be somewhat arbitrary. Finally,

the use of a buffered saline bath, devoid of proteins and other small biomolecules found in the human body, represents another limitation. Nevertheless, the results allow for some valuable comparisons between native soft tissue and synthetic analogues.

## CHAPTER 4

### EFFECTS OF POLYMER STRUCTURE AND 3D PRINTING ON THE MECHANICAL PROPERTIES AND FATIGUE PERFORMANCE OF PCU

#### 4.1 Introduction

While short-term trials and preclinical tests have proven successful for several PCU devices, their long-term success will depend in part on fatigue behavior. The structure-fatigue properties of PCUs represent an understudied area that can potentially provide valuable information for materials optimization. In addition, the convenience of 3D printing techniques has much to offer in terms of device design and manufacturing, but its effects on fatigue properties are also largely understudied. As such, the objectives of this study are twofold:

1. Examine the fatigue behavior of soft PCUs with systematically varied hardness to develop an understanding of the relationship between material structure and fatigue response.
2. Compare the fatigue behavior of 3D printed (FDM) PCUs with those of traditional, injection molded PCUs to develop an understanding of the effects of such processing on the fatigue behavior of the materials.

It is our hypothesis that PCU hardness, which is indicative of hard segment content and consequently degree of hydrogen bonding and energy dissipation, will have implications on material fatigue performance. Specifically, increased hard segment content will lead to improvements in fatigue performance (i.e. higher cycles to failure). In addition, we hypothesize that the layer-by-layer addition process of FDM will have detrimental impacts on the fatigue performance (i.e. lower cycles to failure) and mechanical properties

(i.e. diminished tensile failure stress, tensile failure strain, and shear stress) of PCUs due to the inclusion of voids and weak interlayer bonding.

## **4.2 Materials and Methods**

### 4.2.1 Materials and processing

Carbothanes AC-4075A (75A), AC-4085A (85A), and AC-4095A (95A) were obtained from Lubrizol in pellet form. Processing methods utilized in this study include: compression molded (CM), injection molded (IM), and 3D printed (FDM). Compression molded sheets were formed by first drying the pellets in a vacuum oven at 95°C and -25 inHg for a minimum of 2 hours. Dried PCU pellets were then placed in a hot press (Carver, Model 3851-0) (200°C for 75A and 85A, 210°C for 95A, 500 lbs pressure, 10 minutes) and pressed into sheets of approximately 1.5 and 6 mm in thickness. For injection molded sheets, PCU pellets were sent to Lansen Mold Co. Inc., and injection molded into 6 mm thick sheet stock. To form the sheet stock, the pellets were first dried for 2 hours at 95°C. The dried pellets were then melted and injected at a velocity of approximately 4 cm/sec using the mold, nozzle, front, middle, and rear temperatures as provided by Lubrizol documentation (18°C, 195°C, 200°C, 200°C, 195°C respectively for 75A and 85A; 18°C, 215°C, 210°C, 210°C, 205°C respectively for 95A). 3D printer filament was formed by sending the PCU pellets to 3D Filament Manufacturing Co. for extrusion into 3 mm diameter filament. Phosphate buffered saline (PBS) was obtained from Sigma-Aldrich.

### 4.2.2 3D printing and quality control

All FDM samples were printed using a Lulzbot TAZ 5 3D printer (Aleph Objects, Inc.) equipped with a Flexystruder V1 tool head having a 0.5 mm nozzle. To assist with removal of the printed sample, the printing surface was coated with a uniform layer of acid

free glue stick which was allowed to dry. Prior to printing, the PCU filament was dried in a vacuum oven for a minimum of 2 hours at 95°C and -25 inHg. While FDM printers have a large number of parameters (nozzle temperature, print speed, method of infill, etc.) which can ultimately impact the properties of the printed part, a thorough investigation of these parameters was not the focus of this study. Instead, preliminary studies were carried out to determine the most optimal parameters for our purpose of investigating the effects of 3D printing on the structure and resultant mechanical properties of PCU. Slic3r software was used to generate the G-code printing files as it was found to give the greatest control over the print. All FDM samples were printed with a 0.15 mm layer height, 0.30 mm extrusion width, and 100% rectilinear infill alternating +/- 45° with the specimen axis where applicable. Tensile monotonic and fatigue dogbone sample layers were printed with three concentric perimeters before the rectilinear infill which overlapped 75% with the perimeters. Tensile and fatigue dogbone samples were printed one at a time, in a “laying down” fashion, with layers parallel to the specimen axis and specimen width. Compression monotonic and shear cylindrical samples were printed with a single perimeter before the rectilinear infill which overlapped 15% with the perimeter. Compression and shear cylindrical samples were printed six at a time, in a “standing up” fashion, with layers perpendicular to the specimen axis. Due to their small size, six compression and shear samples were printed at a time to allow adequate time for the previous layers to cool, making their interlayer bonding more consistent with fatigue and monotonic tension samples. The nozzle temperature was set at 225°C and bed temperature at 40°C for all three grades of PCU. Printing speeds for tensile monotonic and fatigue samples were 7.5, 9, and 9 mm/sec for 75A, 85A, and 95A respectively. First layers and external perimeters were



printed at 50% speed. Compression monotonic and shear samples were printed at a 50% multiple of the given speeds. Extrusion multipliers were set at 1.30, 1.20, and 1.25 for 75A, 85A, and 95A respectively. Care should also be taken in leveling the print bed and setting the z-axis home position as per the instruction manual. Unfortunately for the Lulzbot TAZ 5 this is a manual operation, and if not done correctly, can have a profound impact on the quality of the print. Unless otherwise noted, all FDM samples used in this study were allowed to rest a minimum of 1 week at room temperature before testing (see Sections 4.2.3.5 and 4.3.1.5). Although the authors did not complete an exhaustive study of each parameter, the above listed values were found to result in high quality prints that were nearly 100% solid, samples of which are shown in Figure 4.1. The use of the concentric perimeter(s) with +/- 45° rectilinear infill is supported in the limited available literature as it was found that laminae parallel to the loading axis were best for tensile strength while both parallel and alternating +/- 45° laminae were superior in fatigue performance for FDM ABS [163, 165]. The infill pattern used in this study represents a combination of parallel and +/- 45° laminae that was independently found to result in good tensile monotonic properties. It should be noted that FDM printing with flexible filaments is particularly challenging as most FDM tool heads rely on the filament's own stiffness to create pressure within the nozzle for extrusion. As such, the use of tool heads specifically designed for flexible filaments (ex. Flexystruder) is recommended, in addition to printing at slow speeds such as those specified.

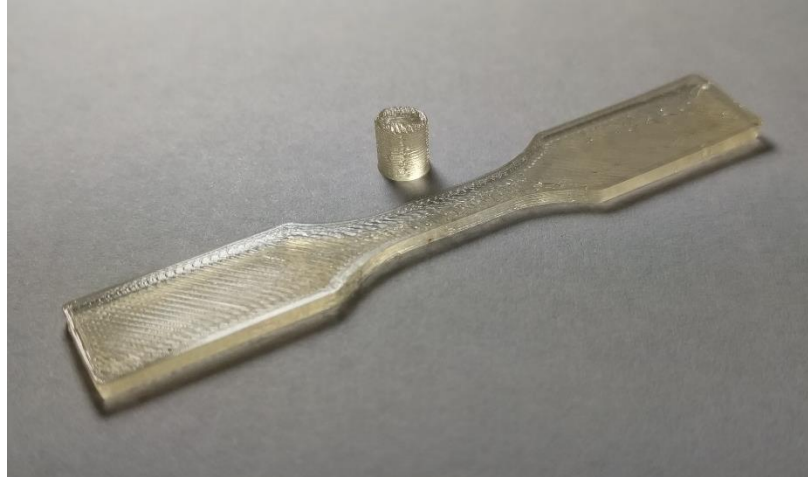


Figure 4.1: Representative FDM tension monotonic and shear samples.

While the listed parameters routinely resulted in high quality printed samples, some degree of variation is to be expected, and indeed variability was observed during this study. Perhaps due to the slight differences in z-axis height at different locations on the print plate, or due to variations in the printing filament itself, it was visibly clear that some samples contained more voids than others. In addition, due to factors such as slight variations in filament diameter or overtightened screws of the tool head, the Flexystruder would on occasion have difficulty feeding and extruding at the proper rate. This could result in anything from samples with a dramatic criss-cross patterning of voids to a complete blockage of the tool head causing a failure to print. As such, it was necessary to develop a quality control standard so that samples could be accepted or rejected based on an objective criteria. To establish these criteria, 10 dogbone samples (ASTM D638, Type V) of each grade were printed according to the procedure and parameters given in this section. The voids in each dogbone sample gage section were then quantified through microCT ( $\mu$ CT 50, Scanco Medical) with a 10  $\mu$ m voxel size and scanner voltage and current of 55 kVp

and 200  $\mu\text{A}$  respectively. Void fraction and size distribution was then evaluated using a threshold kept constant throughout this study. Finally, samples were tested in monotonic tension until failure in accordance with ASTM D638 at a rate of 10 mm/min. Results show dogbone solid fraction ranging from 0.9876 to 0.9995, with voids ranging in size to a maximum of 130  $\mu\text{m}$ . For reference, the same microCT scan was performed on three IM dogbones of each grade, finding an average solid fraction of over 0.9999. Figure 4.2 shows the distribution of solid fractions for the FDM samples which were similar across the three grades. In addition, Figure 4.2 shows representative 3D images of the voids for several samples. Results showed slight variations in failure stress and strain across the 10 samples in each grade, which is shown in Table 4.1.

While there was considerable variation in the visual appearance of the tensile dogbone samples, no strong trends were obvious relating either solid fraction or largest void size to failure stress or strain. This is perhaps due to the narrow distribution of solid fractions, since even the worst sample was over 98.7% solid. In the interest of having an objective quality control standard, the cutoff criterion was set at a solid fraction of 0.99. Fatigue and shear samples below this solid fraction were not included in this study. For reference, Figure 4.3 shows a plot of all 10 monotonic tests for the 95A grade. The solid lines represent samples above the 0.99 solid fraction cutoff, whereas the two dashed lines represent those below. As is shown, the samples below the cutoff are nearly indistinguishable from the rest in terms of monotonic tension performance.

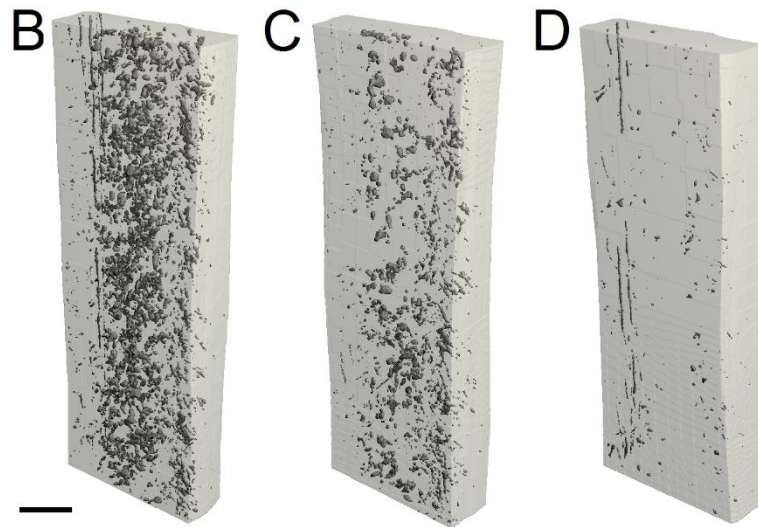
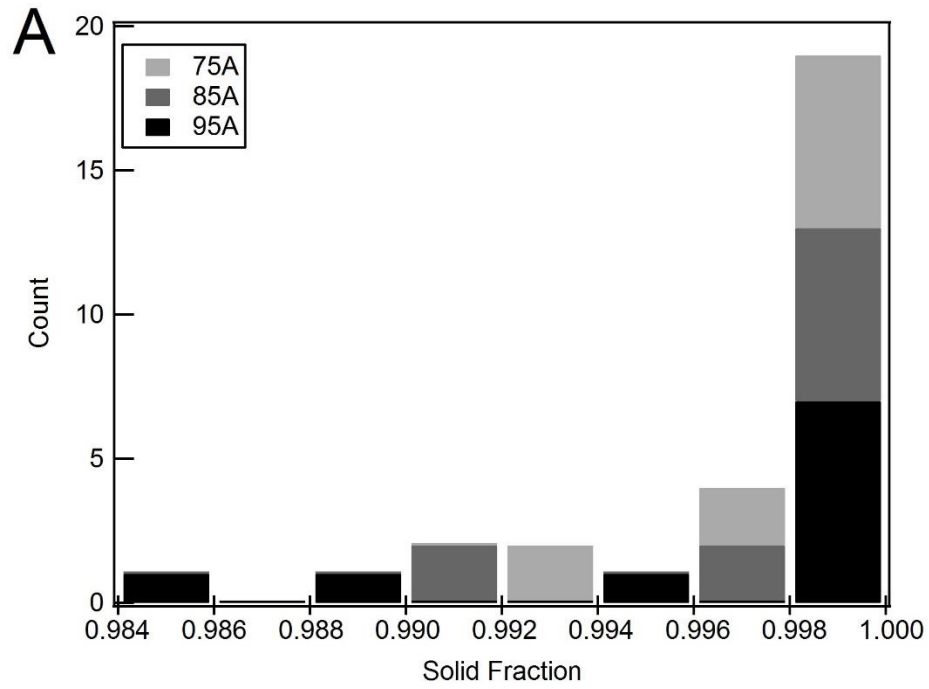


Figure 4.2: Histogram of dogbone sample solid fraction (A). 3D images showing void distribution for grade 95A with solid fractions of 0.9876 (B), 0.9956 (C), and 0.9993 (D). Scale bar represents 1 mm.

Table 4.1: Tabulated data from FDM quality control tests.

Sample	75A				85A				95A			
	Solid Fraction	Largest Void (mm)	Failure Stress (MPa)	Failure Strain (mm/mm)	Solid Fraction	Largest Void (mm)	Failure Stress (MPa)	Failure Strain (mm/mm)	Solid Fraction	Largest Void (mm)	Failure Stress (MPa)	Failure Strain (mm/mm)
1	0.9988	0.07	55.2	4.66	0.9985	0.05	52.6	4.47	0.9992	0.07	54.2	3.95
2	0.9984	0.06	49.4	4.68	0.9989	0.08	54.5	4.53	0.9992	0.07	56.4	4.24
3	0.9923	0.10	42.1	4.74	0.9981	0.10	49.3	4.57	0.9989	0.08	55.5	4.21
4	0.9981	0.08	54.2	4.61	0.9990	0.09	51.1	4.72	0.9898	0.10	55.5	4.24
5	0.9990	0.07	56.9	4.49	0.9988	0.09	50.8	4.59	0.9995	0.07	49.2	3.62
6	0.9920	0.09	43.7	4.79	0.9911	0.08	66.7	5.00	0.9989	0.08	54.8	4.08
7	0.9960	0.12	55.5	4.84	0.9901	0.12	65.1	5.03	0.9985	0.09	54.5	4.33
8	0.9986	0.06	53.7	4.63	0.9978	0.06	57.1	4.77	0.9956	0.11	52.4	4.16
9	0.9964	0.08	53.7	4.68	0.9979	0.07	61.9	4.90	0.9876	0.13	53.3	4.33
10	0.9988	0.06	52.4	4.47	0.9986	0.09	64.4	4.79	0.9993	0.07	56.7	4.19
Average	0.9968	0.08	51.7	4.66	0.9969	0.08	57.4	4.74	0.9967	0.09	54.3	4.14
STD	0.0025	0.02	4.8	0.11	0.0032	0.02	6.3	0.19	0.0041	0.02	2.1	0.20
Median	0.9983	0.08	53.7	4.67	0.9983	0.09	55.8	4.75	0.9989	0.08	54.7	4.20

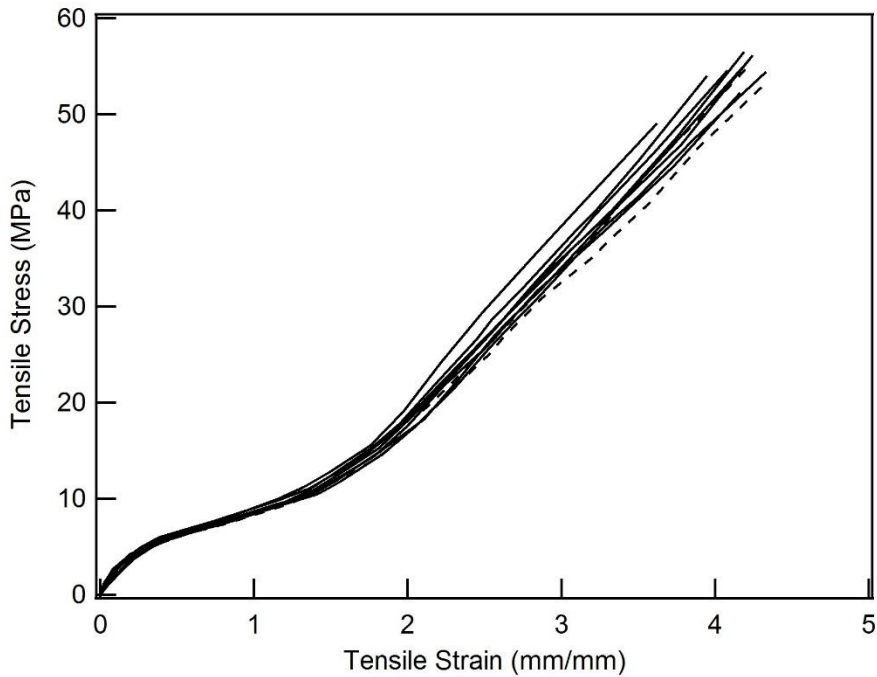


Figure 4.3: Plot of all 10 quality control tensile monotonic tests on 95A samples. Solid lines represent samples above the 0.99 solid fraction cutoff, dashed lines represent samples below the cutoff.

### 4.2.3 Characterization

#### *4.2.3.1 Differential scanning calorimetry*

DSC was performed in a nitrogen environment (TA Instruments Discovery DSC, New Castle, DE) to identify glass transition temperatures ( $T_g$ ) and phase behavior. Disc-shaped samples of both IM and FDM PCUs were weighed prior to testing (mass between 10 and 15 mg). IM samples were cut from IM sheet stock whereas FDM samples were cut from a tensile dogbone printed in accordance with Section 4.2.2. Samples were equilibrated at a temperature of  $-75^\circ\text{C}$ , ramped at  $10^\circ\text{C}/\text{min}$  to a temperature of  $250^\circ\text{C}$ , held isothermal for 2 minutes, cooled to  $-75^\circ\text{C}$ , held isothermal for 2 minutes, and finally heated again to  $250^\circ\text{C}$  at a rate of  $10^\circ\text{C}/\text{min}$ . The glass transition temperature was denoted as a second order transition on the DSC curve and the midpoint temperature is reported for both the initial heating ( $T_{gs1}$ ) and the second pass ( $T_{gs2}$ ). Temperature  $T_1$ , which is an enthalpy relaxation likely involving hard segment diisocyanate not associated with a chain extender, is reported as the peak temperature of the endothermic transition occurring around  $65^\circ\text{C}$ . Temperature  $T_c$  is reported as the peak temperature of an exothermic transition along the cooling cycle likely associated with hard segment reassociation. Finally, a temperature range is reported ( $T_{mh}$ ) which encompasses endothermic transitions occurring around 130 to  $215^\circ\text{C}$ , where such transitions are evident, and are attributed to multiple melting endotherms of the hard domains [88]. The average and standard deviation of each listed temperature was calculated for each material ( $n = 3$  for each grade and processing method).

#### *4.2.3.2 Dynamic mechanical analysis*

The storage modulus and loss modulus were determined through a temperature sweep by DMA (TA Instruments Q800, New Castle, DE). Rectangular IM samples were

cut from IM sheet stock, while FDM samples of the same geometry were printed using the parameters for tensile monotonic dogbones given in Section 4.2.2. All samples were measured using digital calipers prior to testing (approximately 1 mm by 6 mm in cross-section). Samples were then loaded into the tensile clamps and tested at a frequency of 1 Hz and strain of 0.1%. Samples were equilibrated at a temperature of  $-75^{\circ}\text{C}$ , held isothermal for 2 minutes, and ramped at  $5^{\circ}\text{C}/\text{min}$  to a final temperature of  $180^{\circ}\text{C}$ . The storage and loss moduli were plotted as a function of temperature. Tan delta curve peaks (not shown) were taken as the glass transition temperatures and reported as  $T_{\text{gDMA}}$  ( $n = 3$  for each grade).

#### *4.2.3.3 $^1\text{H}$ Nuclear magnetic resonance spectroscopy*

$^1\text{H}$  NMR was utilized to verify the chemical structure of the PCU. Samples consisted of raw material obtained from Lubrizol. An Agilent DD-1 500 MHz NMR was used to verify the chemical structure of the PCU in deuterated dimethylformamide. Each spectrum was analyzed via ACD NMR Processor software to determine chemical structure.

#### *4.2.3.4 Fourier transform infrared spectroscopy*

FTIR was utilized to examine differences in phase interaction and organization between the different grades of PCU as well as between IM and FDM samples. IM samples were cut from IM sheet stock. FDM samples were cut from a tensile dogbone printed in accordance with Section 4.2.2. A Nicolet FTIR is50 FT-IR (Thermo Scientific) with Smart iTR diamond attenuated total reflectance (ATR) module was used to analyze the degree of phase separation of each PCU. For each spectrum, 16 scans were taken at resolution of  $1\text{ cm}^{-1}$  and ATR correction. Backgrounds scans were taken before each spectrum. Each material was scanned in triplicate. To determine degree of phase separation, the carbonyl

peak was deconvoluted into three peaks using a Gaussian-Lorentzian fit with the Omnic software (Thermo Scientific). The peaks at approximately 1700, 1720, and 1740  $\text{cm}^{-1}$  represent the hydrogen-bonded urethane carbonyl, an overlapping combination of the free urethane carbonyl with the hydrogen-bonded carbonate carbonyl, and the free carbonate carbonyl, respectively [63]. A measure of the degree of phase separation (DPS) was determined following Equation 4.1 [225]. Here, the total area of all three peaks was used due to the overlap of peaks at 1720  $\text{cm}^{-1}$ .

$$\text{Equation 4.1: } DPS = \frac{C_{bonded}}{C_{bonded} + C_{free}} = \frac{A_{1700}}{A_{1700} + A_{1720} + A_{1740}}$$

#### 4.2.3.5 FDM rest time testing

Early monotonic tests on FDM samples identified a need to characterize the phase mixing and subsequent separation that occurs when PCU filament is heated and extruded through the tool head and then allowed to cool and rest at room temperature. To examine this effect, PCU dogbone samples (ASTM D638, Type V) of each grade were printed in accordance with Section 4.2.2, however were not allowed to rest for the specified one week at room temperature. Instead, samples were tested in monotonic tension at six time points after printing: 10 minutes, 1 hour, 8 hours, 1 day, 2 days, and 1 week. Samples were tested until failure at a rate of 10 mm/min. All monotonic samples were measured using digital calipers immediately prior to testing and all tests were performed on an Instron materials testing machine (Model 5567) ( $n = 3$  for each grade and time point). To further probe this effect,



the 75A grade of PCU was examined using FTIR at time points of 10 minutes, 1 hour, and 7 days after printing in accordance with the procedures given in Section 4.2.2.

#### 4.2.4 Monotonic testing

Compression and tensile monotonic tests were utilized to determine the stress-strain behavior of each material. Compression samples consisted of cylinders of approximately 6 mm in diameter and 6 mm in height. CM and IM samples were laser cut (Hermes LS500XL CO2 Laser, 50% power, 25% speed, 36 passes) from the corresponding CM and IM sheet stock, while FDM samples were printed as described in Section 4.2.2. The compression samples were compressed to 90% strain over 10 seconds utilizing a strain-controlled test.

Tensile samples were of dogbone shape in accordance with ASTM D638 (Type V). CM samples were punched from 1.5 mm sheet stock using a standard sample die. IM samples were supplied directly from the manufacturer (Lubrizol). FDM tensile monotonic data was taken from the quality control tests described in Section 4.2.2, which utilized the same dogbone geometry. Tensile samples were tested until failure at a rate of 10 mm/min, also in accordance with ASTM D638. All monotonic samples were measured using digital calipers immediately prior to testing and all tests were performed on an Instron materials testing machine (Model 5567) ( $n \geq 3$  for each grade and processing method).

#### 4.2.5 Shear testing

Shear tests were performed to find the shear strength of each material and test the bonding between layers of FDM samples. Shear samples consisted 4.65 mm diameter ( $\pm 0.025$  mm) cylinders. IM shear samples were laser cut (Hermes LS500XL CO2 Laser,

50% power, 25% speed, 36 passes) from IM sheet stock, while FDM shear samples were printed in accordance with the parameters given in Section 4.2.2. FDM shear samples were scanned via microCT ( $\mu$ CT 50, Scanco Medical) to ensure compliance with the 0.99 solid fraction criteria set in Section 4.2.2. For reference, the IM shear samples were also scanned via microCT. All samples were measured using digital calipers immediately prior to testing. Shear force was applied perpendicular to the cylinder axis (parallel to the layers in the case of FDM samples). Samples were tested at a rate of 1.5 mm/min until complete shearing of cross-section and all tests were performed on an Instron materials testing machine (Model 5567). The maximum shear stress was recorded for each test ( $n = 6$  for each grade and processing method).

#### 4.2.6 Fatigue testing

Cyclic tests were performed in order to develop fatigue life curves for each material. Fatigue tests were performed in a displacement-controlled, zero-to-tension manner on the custom dogbone shape shown in Figure 4.4. Attempts were made to follow sample geometry given in specifications such as ASTM E606 and D4482, however the sample geometries proved too slender for the PCUs considered in this study. Unlike conventional rubbers, PCU exhibits considerable viscoelasticity and will relax under strain-controlled cyclic loading. This leads to the development of compressive stresses upon returning to zero strain and ultimately can lead to buckling if the sample is too slender. Instead, ASTM E606 and D4482 were used as guidelines in developing the custom shape shown in Figure 4.4. The design was developed through iterations in an effort to prevent buckling and promote failure through the gage length, as well as provide a reasonable shape for injection molding, laser cutting, and 3D printing. IM samples were laser cut (Hermes

LS500XL CO2 Laser, 50% power, 25% speed, 36 passes) from 6 mm thick IM sheet stock, while FDM samples were printed as detailed in Section 4.2.2. FDM fatigue samples were scanned via microCT ( $\mu$ CT 50, Scanco Medical) to ensure compliance with the 0.99 solid fraction criteria set in Section 4.2.2. For reference, three IM fatigue samples of each grade were also scanned via microCT. Samples were tested at 5 Hz in a room temperature PBS bath, and were allowed to soak in PBS for a minimum of 24 hours before testing. Specimen dimensions were recorded using digital calipers immediately prior to testing. Tests were recorded via video camera to determine the exact strain amplitude reached during testing, and strain amplitudes ranged from approximately 20% to 150% to develop the fatigue life curves. Fatigue data is plotted against strain amplitude as well as the stress amplitude at each sample's median life. Median life stress amplitude was used due to the stress relaxation exhibited by these materials under strain-controlled loading. All fatigue tests were performed using an MTS Bionix machine with a 15 kN load cell and were run until complete rupture of the cross section or they reached 1 million cycles. A minimum of 20 samples was used to develop the curves for each material, with two samples reaching runout at 1 million cycles. For reference, an SEM image of the fracture surface was taken at 20x magnification for one sample of both IM and FDM varieties of the 85A grade (Hitachi S-3700N SEM).

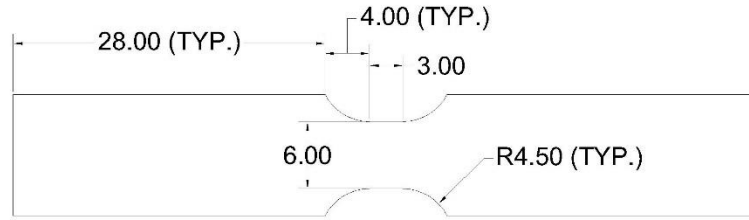


Figure 4.4: Custom dogbone shape used in fatigue tests, all dimensions in millimeters. Samples were approximately 6 mm thick.

#### 4.2.7 Statistical analysis

Comparisons between the degree of phase separation, compressive moduli, tensile failure strain, tensile failure stress, shear stiffness, and shear strength of the materials were performed with a Student's t-test. Comparisons between material fatigue performances were performed via linear regression with a dummy variable, similar to that performed by Bizal et al. [226], on the fatigue data based on median life stress amplitude. This analysis returns the coefficients of a linear formula (Equation 4.2) to determine the logarithm of cycles to failure based on the logarithm of stress amplitude and a dummy variable (DV) to differentiate between sample types. For example, the DV was set to a value of 0 for IM samples and 1 for FDM samples. The analysis also returns the significance of the effects of the DV on the intercept and slope of the resulting line. Runouts were not included in the analysis due to not representing actual sample failure. As shown in Equation 4.2, the variables  $A_0$  and  $A_1$  represent the intercept (x-axis) and slope of the fit line, respectively, for the control samples (i.e. when the DV is equal to 0). Variables  $A_2$  and  $A_3$  represent modifications to the intercept and slope, respectively, to fit the data of the samples of interest (i.e. the samples for which the DV is equal to 1).

$$\text{Equation 4.2: } \log \textit{Cycles} = A_0 + (A_1 * \log \textit{ML Stress}) \\ + (A_2 * DV) + (A_3 * DV * \log \textit{ML Stress})$$

## 4.3 Results

### 4.3.1 Characterization

#### *4.3.1.1 Differential scanning calorimetry*

Figure 4.5 shows representative DSC curves for the tested PCUs, Table 4.2 shows tabulated transition temperatures for each material calculated from both DSC as well as DMA results. Figure 4.5 includes the full first cycle, heating and cooling, on top and then the subsequent heating cycle below for each grade. Each material shows a clear glass transition temperature between -20°C and -30°C on the initial heating ramp ( $T_{gs1}$ ) with the 95A grade being approximately 6°C higher than both 75A and 85A. Upon the second heating cycle, all three grades show a rightward shift in glass transition ( $T_{gs2}$ ) of approximately 10°C, 14°C, and 4°C for 75A, 85A, and 95A, respectively. This shift could perhaps indicate a residual mixing of phases from the initial heating cycle. All three grades consistently show  $T_1$  near 66°C, with 75A and 85A showing a more pronounced endothermic reaction than 95A. The  $T_c$  peak varies between approximately 50°C and 100°C among the three grades, with 95A clearly showing the most pronounced exothermic reaction, followed by 85A, and then 75A which is only detectable in the raw data. The hard domain melting endotherms are given only as an approximate range in Table 2 ( $T_{mh1}$  and  $T_{mh2}$ ). The endotherms for IM 75A were not detectable, however FDM 75A samples displayed very slight transitions which were only detectable in the raw data. The hard domain melting transitions are much more pronounced in 85A and 95A, with 95A

displaying three distinct endotherms within the range. As described by Eceiza et al., these endotherms correspond to dissociation of long range ordering as well as melting of the crystalline regions in continuous hard microdomains [88]. In addition, these hard segment transitions show a clear rightward shift with increasing material hardness which indicates a higher hard segment content [88].

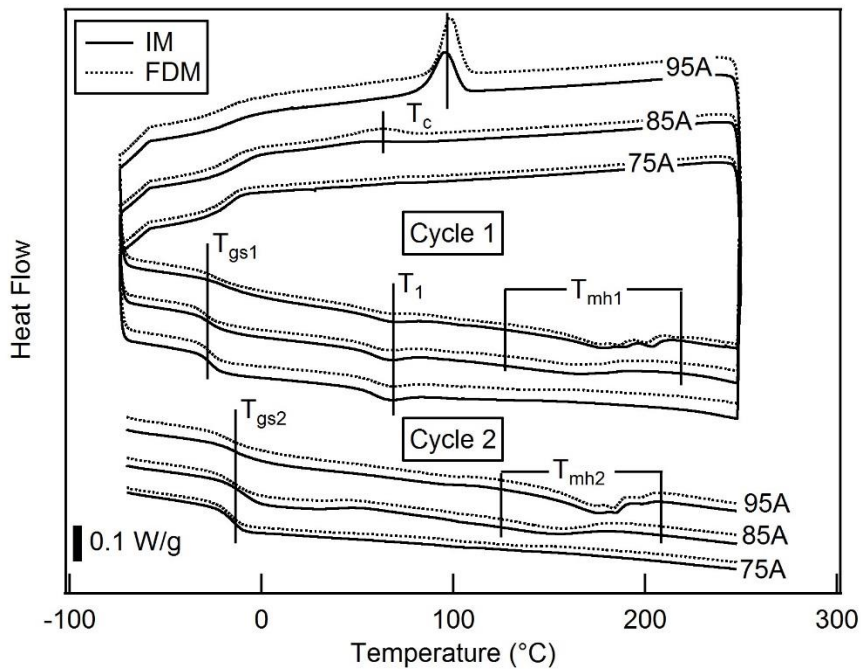


Figure 4.5: Representative DSC curves for each material. Endothermic reactions shown in the downward direction. Initial heating and cooling (Cycle 1) shown on top with subsequent heating cycle shown below (Cycle 2).

Table 4.2: Tabulated transition temperatures from DSC and DMA data, ND denotes not detectable (n = 3 for each grade and processing method).

Grade	Processing	T <sub>gs1</sub> (°C)	T <sub>gs2</sub> (°C)	T <sub>1</sub> (°C)	T <sub>c</sub> (°C)	T <sub>mh1</sub> (°C)	T <sub>mh2</sub> (°C)	T <sub>gDMA</sub> (°C)
		Average ± STD	Average ± STD	Average ± STD	Average ± STD	Range	Range	Average ± STD
75A	IM	-26.1 ± 0.1	-16.1 ± 0.2	66.3 ± 0.2	70.8 ± 0.2	ND	ND	-5.6 ± 0.7
	FDM	-26.7 ± 0.4	-17.2 ± 0.4	67.5 ± 0.3	75.8 ± 1.0	125 - 150	125 - 150	-6.3 ± 1.1
85A	IM	-26.4 ± 0.6	-12.0 ± 0.6	66.2 ± 0.2	53.6 ± 1.1	135 - 190	130 - 175	-1.4 ± 0.7
	FDM	-28.4 ± 1.5	-15.0 ± 1.5	64.8 ± 0.1	58.6 ± 2.7	135 - 190	130 - 175	-8.0 ± 0.5
95A	IM	-20.4 ± 0.5	-16.9 ± 0.5	66.3 ± 0.7	95.9 ± 0.6	145 - 215	140 - 205	17.0 ± 1.1
	FDM	-24.1 ± 0.6	-18.2 ± 0.6	64.2 ± 0.3	97.2 ± 0.9	145 - 210	140 - 205	8.1 ± 1.7

#### 4.3.1.2 Dynamic mechanical analysis

Figure 4.6 shows representative storage modulus and loss modulus curves for the PCUs. The T<sub>g</sub> determined from the tan delta peak (Table 4.2) consistently reported 20-40°C higher than DSC, an expected result due to fundamental differences between DMA and DSC [157]. The curves demonstrate a clear trend of increasing loss modulus with an increase in material hardness between approximately 0°C and 100°C. The storage modulus versus temperature curves show the expected glassy to rubbery transition behavior with the rubbery modulus increasing with material hardness. FDM samples demonstrated subtle, yet consistent, differences from IM samples. Both FDM 75A and 85A show a faster drop off in rubbery modulus than their IM counterparts. FDM 85A and 95A show a slight leftward shift in T<sub>g</sub> which is supported by tan delta peak data (Table 4.2).

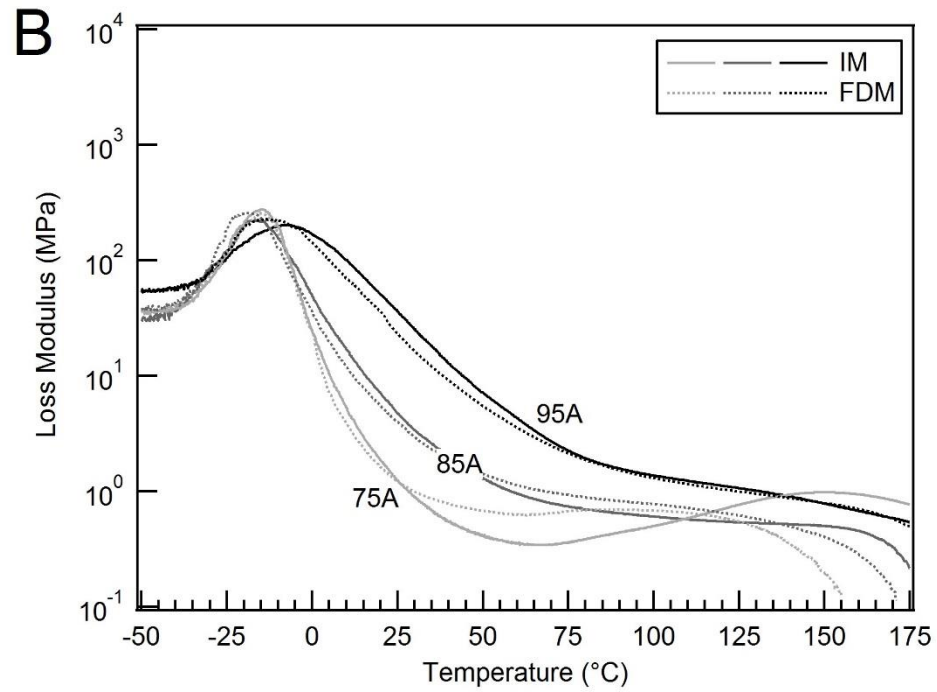
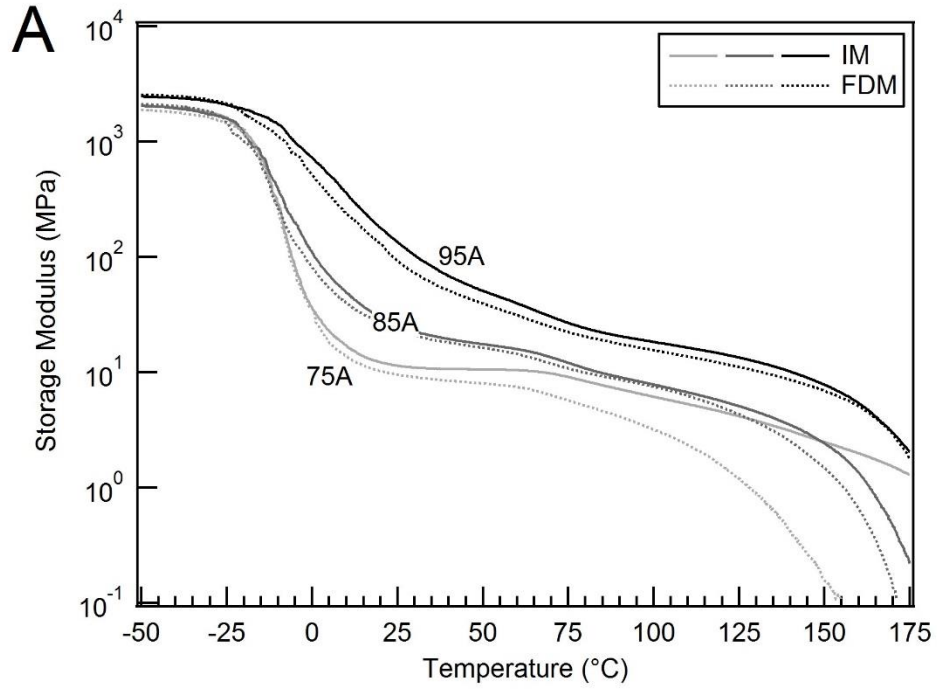


Figure 4.6: Representative storage modulus (A) and loss modulus (B) curves for each grade of PCU.



#### 4.3.1.3 $^1\text{H}$ Nuclear magnetic resonance spectroscopy

A representative NMR spectrum is shown in Figure 4.7 and corresponding chemical structure in Figure 4.8 with labels a-g. The use of MDI is confirmed with peaks 'a', 'b', 'c', and 'd'. BDO is the most commonly used chain extender and represented by peaks 'e' and 'f'. The polycarbonate diol is based on polyhexamethylene carbonate diol with a peak at 'g' in particular that represents the methylene that neighbors the methylene adjacent to the carbonate group. In addition, the peak at 'h', ~1.43 ppm, is found in polyhexamethylene carbonate diol, as previously reported by Tanaka [227]. There was significant overlap of the peaks at 'e', which represent the methylene group adjacent to the carbonate and urethane groups.

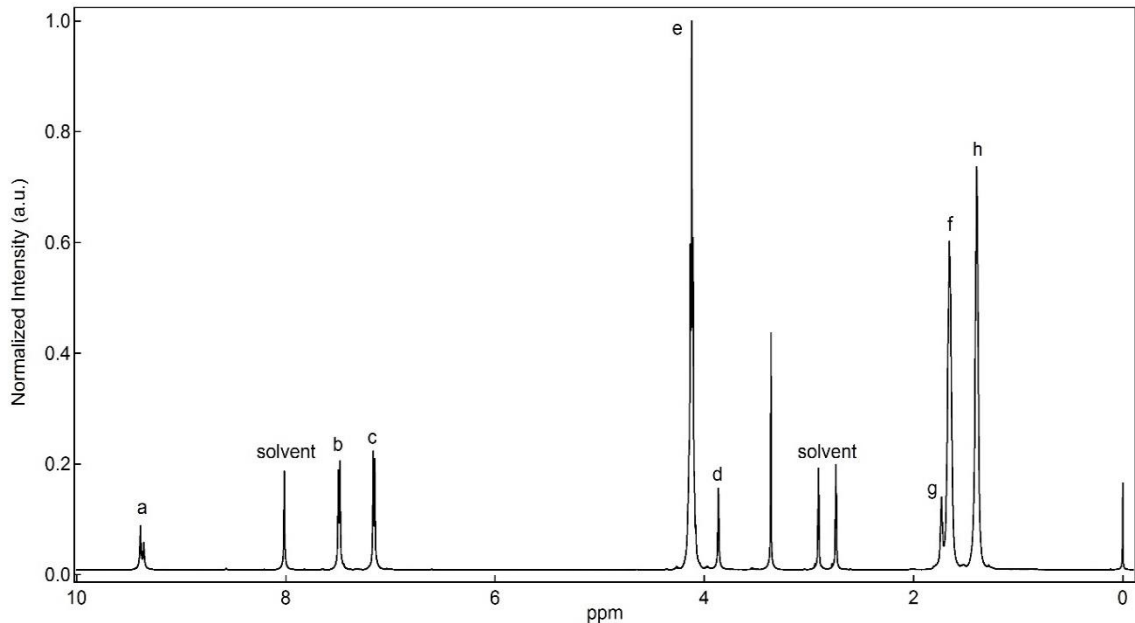


Figure 4.7: Representative NMR spectrum of 85A grade, labels correspond to moieties given in Figure 4.8.

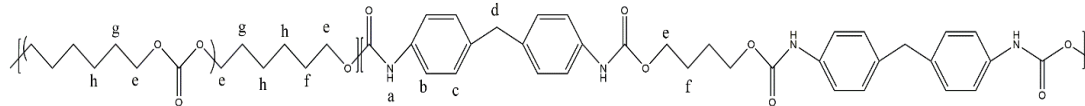


Figure 4.8: Chemical structure of PCU material, labels correspond to peaks in Figure 4.7.

#### 4.3.1.4 Fourier transform infrared spectroscopy

Representative FTIR spectra for each grade and processing method can be found in Figure 4.9. The most obvious differences between the three grades of PCU are found at the carbonyl peaks near  $1700\text{-}1740\text{ cm}^{-1}$ . To quantify these changes, the DPS for each grade and processing method are given in Table 4.3. The DPS significantly increased as the grade changed from 75A to 85A to 95A ( $p < 0.01$ ). There was no significant difference for the DPS between IM and FDM for any grade of PCU.

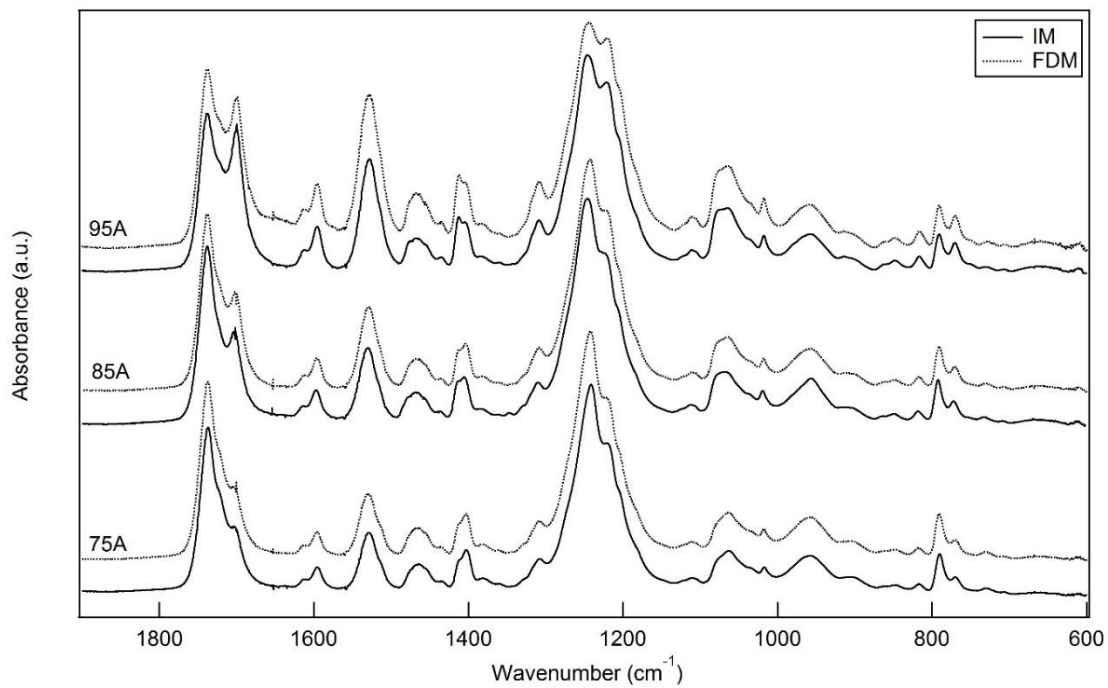


Figure 4.9: Representative FTIR spectra for each grade of PCU for both IM and FDM samples.

Table 4.3: Degree of phase separation as determine from Equation 4.1. No significant differences were found between IM and FDM samples of the same grade.

Grade	DPS (%)	
	IM	FDM
75A	18.99 ± 2.12	18.64 ± 1.52
85A	27.94 ± 0.39	27.8 ± 0.65
95A	43.57 ± 1.86	41.07 ± 3.62

#### 4.3.1.5 FDM rest time testing

Representative curves for each grade and time point are shown in Figure 4.10 with IM curves included in the plots for reference. The 75A curves show a clear trend towards increasing failure stress, decreasing failure strain, and increasing overall stiffness between the 10 minute and 7 day time points. The effect is much less pronounced with the tested time points for both 85A and 95A. Differences in failure strain between the 2 day and 7 day time points are not statistically significant for any grade of PCU. This is also illustrated in Figure 4.11, which shows the average failure strain across all three tests for each time point and grade. Despite the stabilization in response after 2 days, all three grades of FDM samples still exhibit larger failure strains than their IM counterparts. Based on these results, a 7 day minimum rest period at room temperature was implemented for the other tests in this study. Representative FTIR curves of the carbonyl peak at 1700-1740  $\text{cm}^{-1}$  for the 75A grade at time points of 10 minutes, 1 hour, and 7 days are shown in Figure 4.12. As time passed, the peak at 1700  $\text{cm}^{-1}$  became more prominent and defined, while the peak at 1720  $\text{cm}^{-1}$  decreased relative to the peak at 1700  $\text{cm}^{-1}$ , which indicates that the concentration of hydrogen bonded urethane carbonyl is increasing and that phase separation is occurring post printing [228].

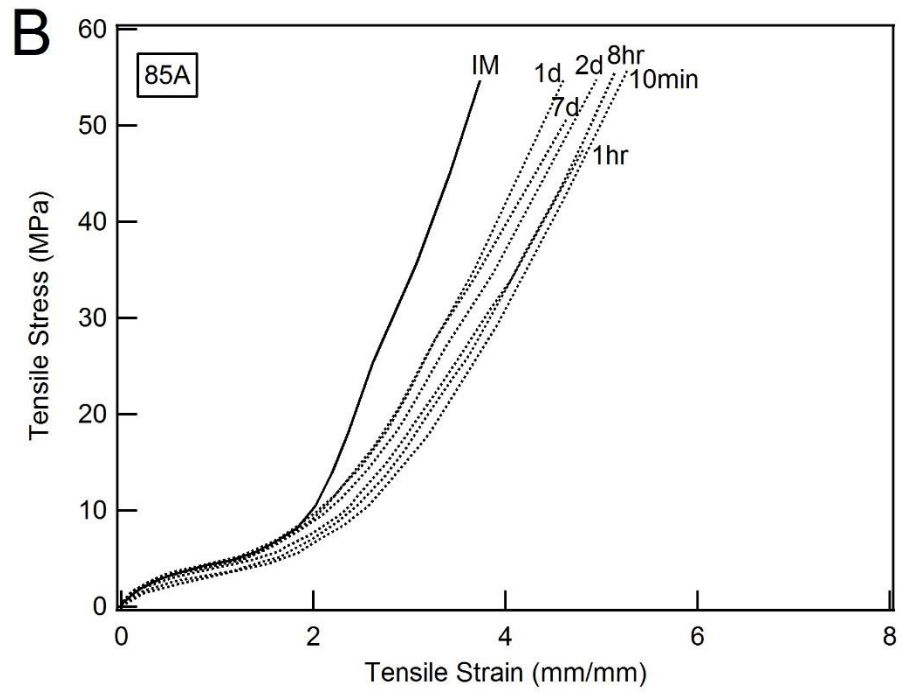
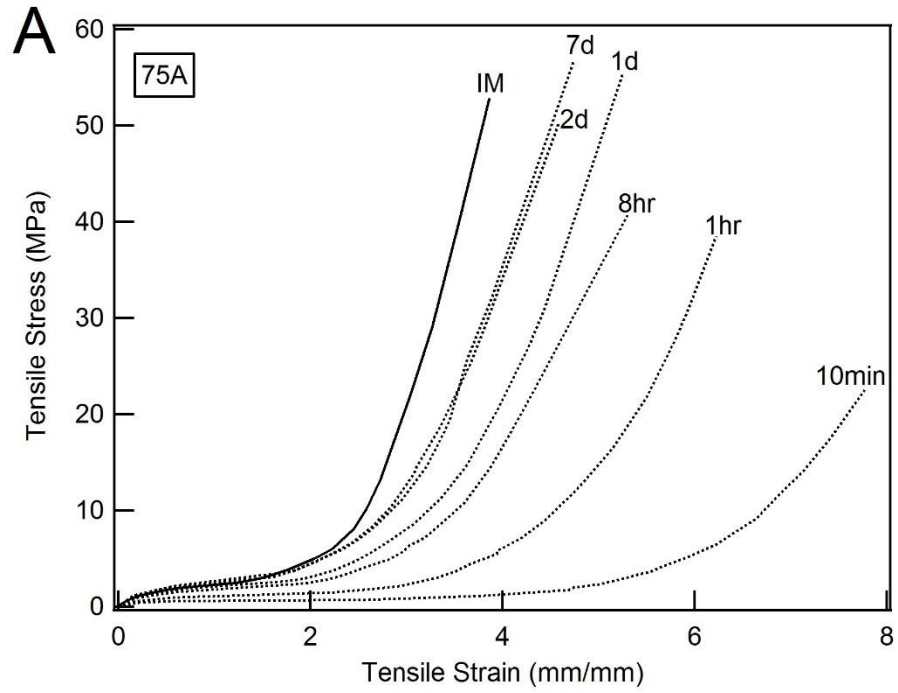


Figure 4.10: Representative curves for monotonic tension tests at various times points after printing for 75A (A), 85A (B), and 95A (C).

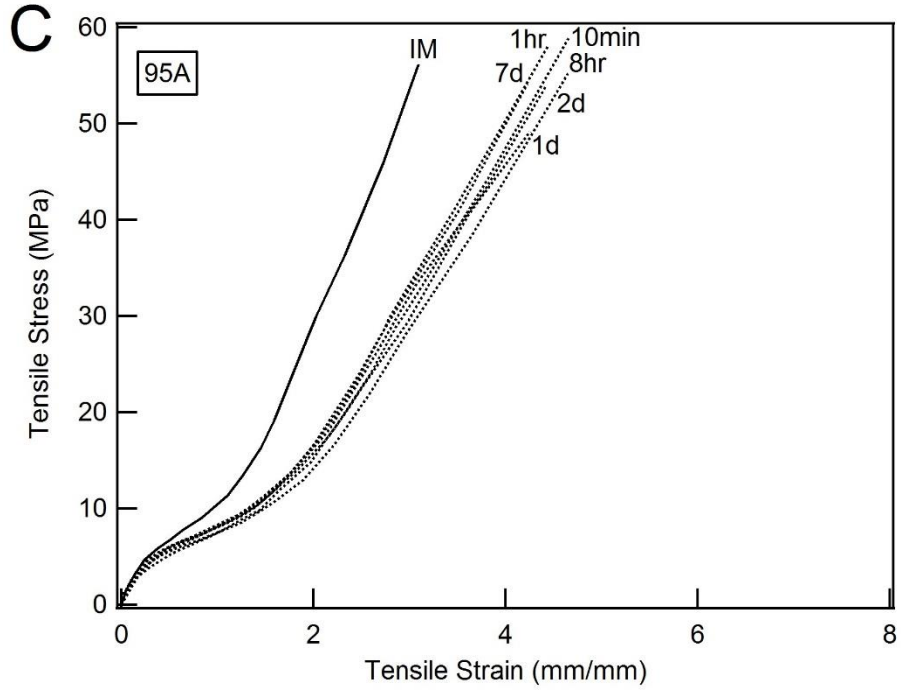


Figure 4.10: Continued

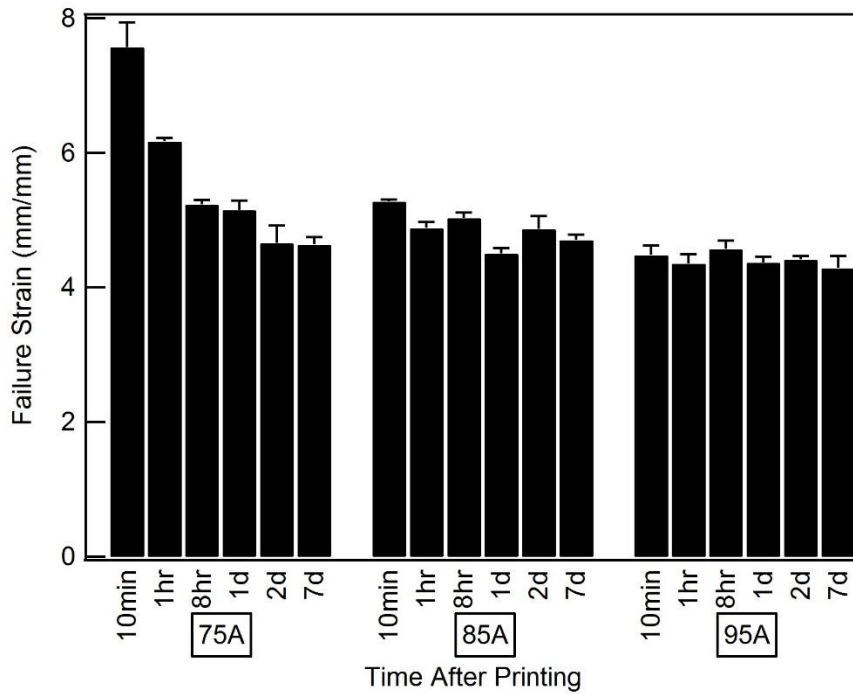


Figure 4.11: Average failure strain of FDM samples by grade and time after printing, error bars indicate standard deviation (n = 3 for each grade and time point). No significant differences were found between 2d and 7d time points for any grade.

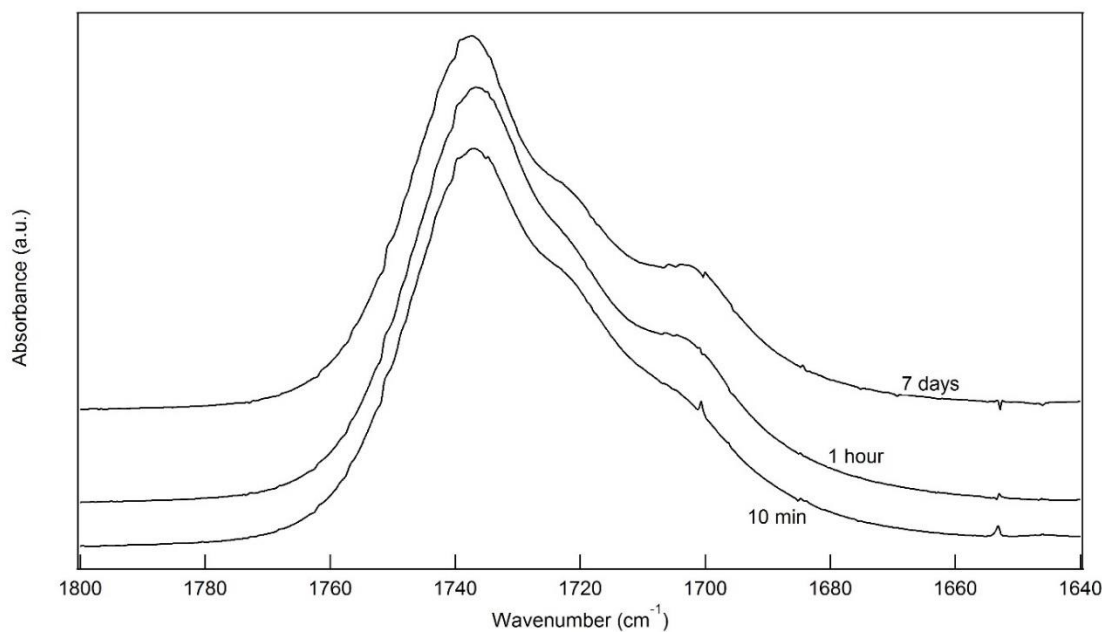


Figure 4.12: Representative FTIR curves of the carbonyl peak of FDM 75A at 10 minutes, 1 hour, and 7 days after printing.

#### 4.3.2 Monotonic testing

Representative monotonic tension and compression curves for each grade and processing method are shown in Figure 4.13. All tensile plots represent a median sample based on failure stress, and FDM data is taken from the quality control tests detailed in Section 4.2.2. The materials demonstrate statistically significant increases in modulus with increasing hard segment content as expected ( $p < 0.0001$  for IM compressive modulus, between all 3 grades). The materials also demonstrate classic elastomeric behavior, however comparing the tensile curves across grades indicates that an increasing hard segment content begins to eliminate the characteristic plateau region. The difference in failure strain between IM 75A and 85A was not significantly different, however both showed significantly larger failure strains than 95A ( $p = 0.0011, 0.0018$ , for IM 75A and

85A, respectively). Differences in failure stress among the three IM grades were not significantly different. FDM samples demonstrated significantly larger failure strains in tension compared to IM counterparts ( $p < 0.0001$  for all grades) despite remarkably maintaining failure stress that was not significantly different. Figure 4.14 displays a representative image of each sample variety immediately before failure in monotonic tension. The FDM samples for the 75A and 85A grades showed a noticeable difference in opacity compared to their IM counterparts, perhaps indicating better strain crystallization, despite the stresses for all the shown samples being very similar (ranging from 51.1 to 56.7 MPa). Examination of monotonic tension videos reveals that this increased opacity is evident in FDM samples even before reaching the failure strain of their IM counterparts, suggesting that the strain crystallization is not simply a result of increased strain. As indicated in Table 4.1, there was some variation in the tensile failure stress among FDM samples. Table 4.4 shows tabulated data on tensile failure stress and strain for FDM and IM samples.



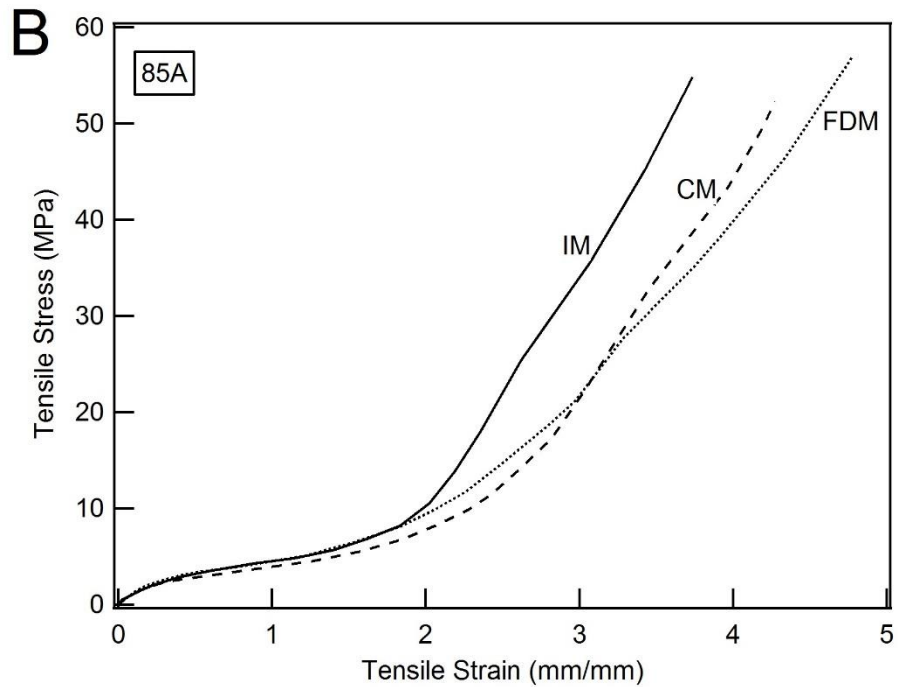
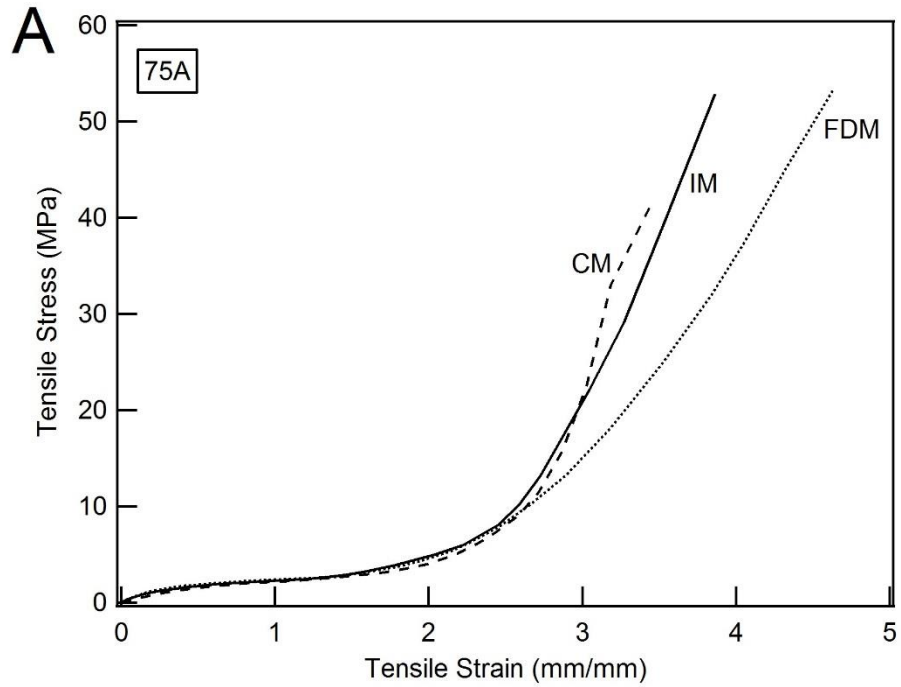


Figure 4.13: Representative monotonic tension curves for 75A (A), 85A (B), and 95A (C) as well as representative monotonic compression curves (D). FDM tensile samples show significantly increased failure strain vs. IM samples with no difference in failure stress. Increased HSC leads to significantly increased compressive modulus ( $p < 0.0001$  for all).

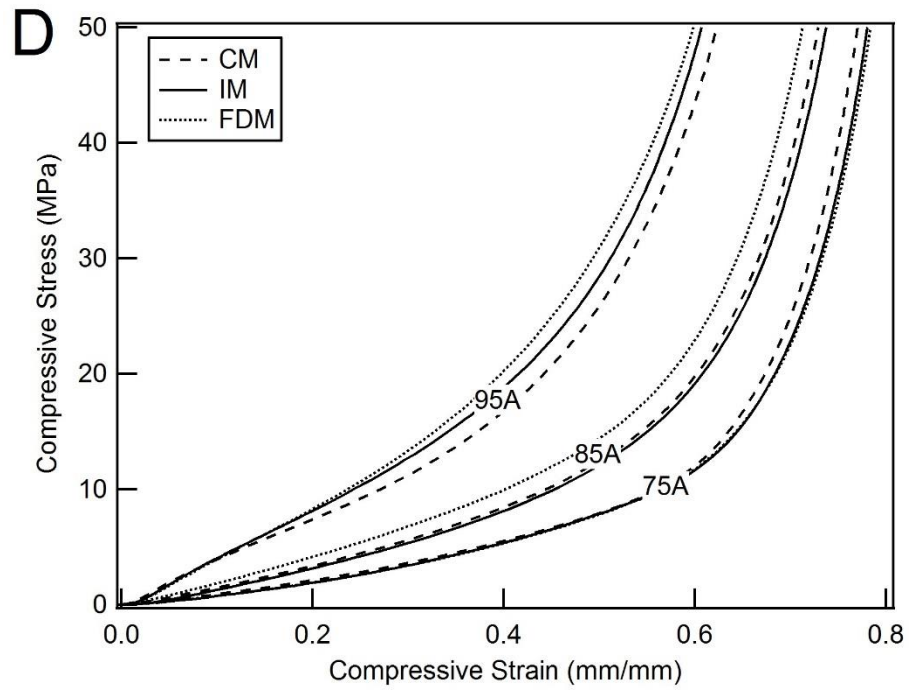
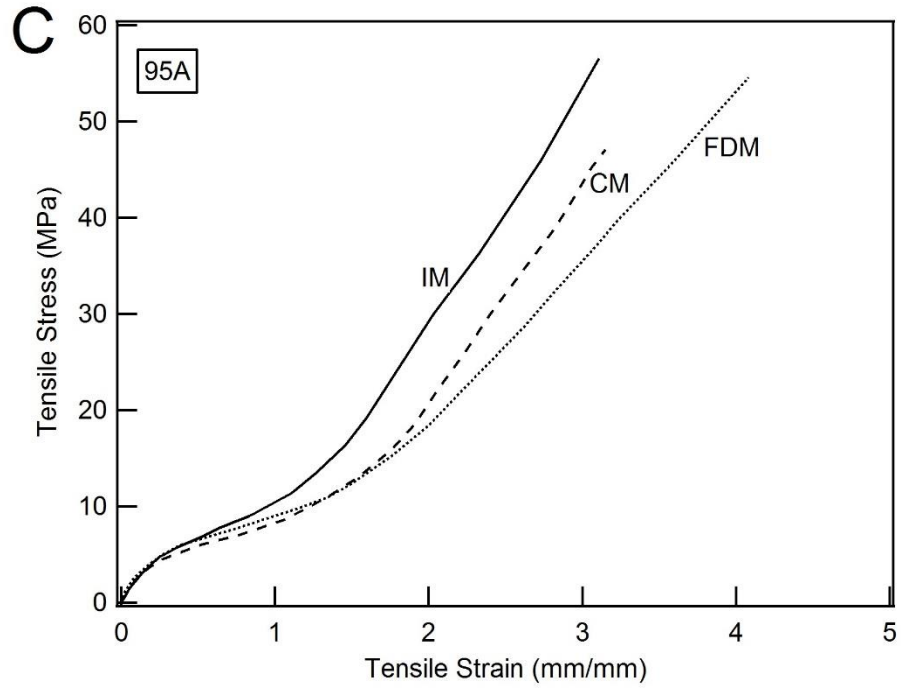


Figure 4.13: Continued

Table 4.4: Tabulated tensile failure stress and strain for FDM and IM samples (n = 10 for FDM, n = 3 for IM).

Grade	Processing	Failure Stress (Mpa)			Failure Strain (mm/mm)		
		Range	Average $\pm$ STD	Median	Range	Average $\pm$ STD	Median
75A	IM	43.7 - 55.2	50.6 $\pm$ 4.9	52.9	3.64 - 3.86	3.75 $\pm$ 0.09	3.76
	FDM	42.1 - 56.9	51.7 $\pm$ 4.8	53.7	4.47 - 4.84	4.66 $\pm$ 0.11	4.67
85A	IM	51.9 - 57.9	54.9 $\pm$ 2.5	54.8	3.74 - 4.05	3.87 $\pm$ 0.13	3.82
	FDM	49.3 - 66.7	57.4 $\pm$ 6.3	55.8	4.47 - 5.03	4.74 $\pm$ 0.19	4.75
95A	IM	56.3 - 57.7	56.8 $\pm$ 0.6	56.5	3.11 - 3.20	3.15 $\pm$ 0.04	3.15
	FDM	49.2 - 56.7	54.3 $\pm$ 2.1	54.7	3.62 - 4.33	4.14 $\pm$ 0.20	4.20

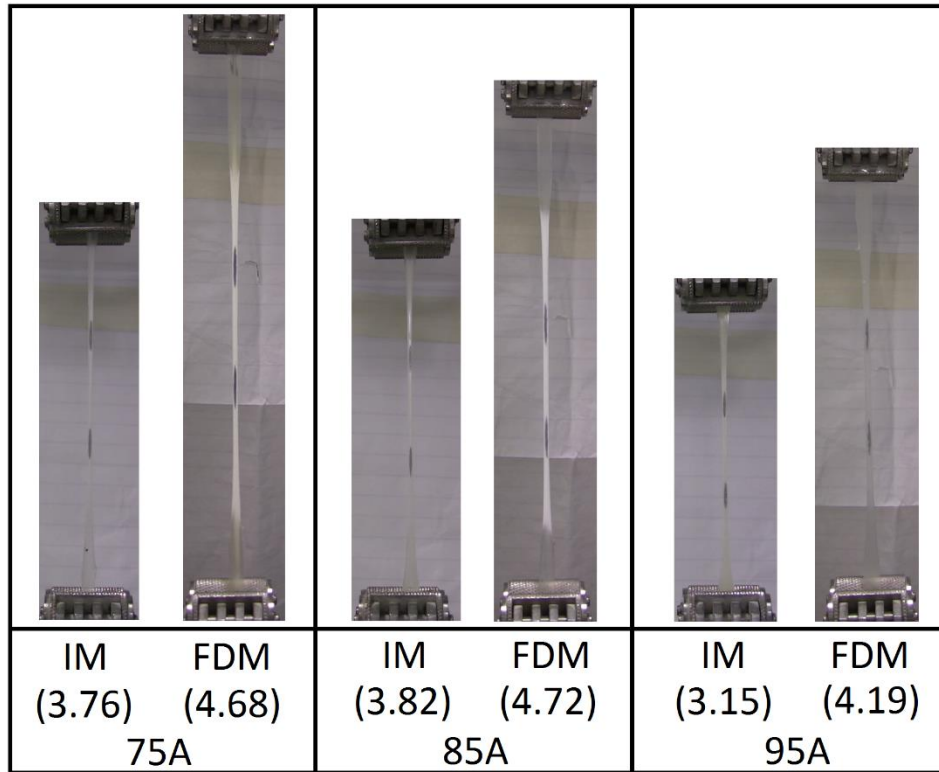


Figure 4.14: Representative images of tensile tests for IM and FDM varieties of each grade, immediately before sample failure, showing differences in opacity. Strain readings shown in parentheses, units in mm/mm. Failure stress for all samples shown ranged between 51.1 and 56.7 MPa.

### 4.3.3 Shear testing

Shear data is summarized in Figure 4.15. Void fractions from microCT scans of FDM shear samples ranged from 0.9947 to 0.9979 among all three grades. For reference, microCT scans of IM shear samples showed an average solid fraction of over 0.9995. Figure 4.15A shows the median plots (based on maximum shear stress) of shear stress versus extension and indicates an expected, and statistically significant, increase in shear stiffness ( $p < 0.0001$  between all IM grades) and strength ( $p < 0.0001$  between all IM grades) with an increase in hard segment content. In addition, Figure 4.15A demonstrates the nearly identical plot shapes between IM and FDM samples. Figure 4.15B shows the average maximum shear stress across all six samples for each processing method and grade and demonstrates that there is no statistically significant difference between IM and FDM samples in terms of maximum shear strength.

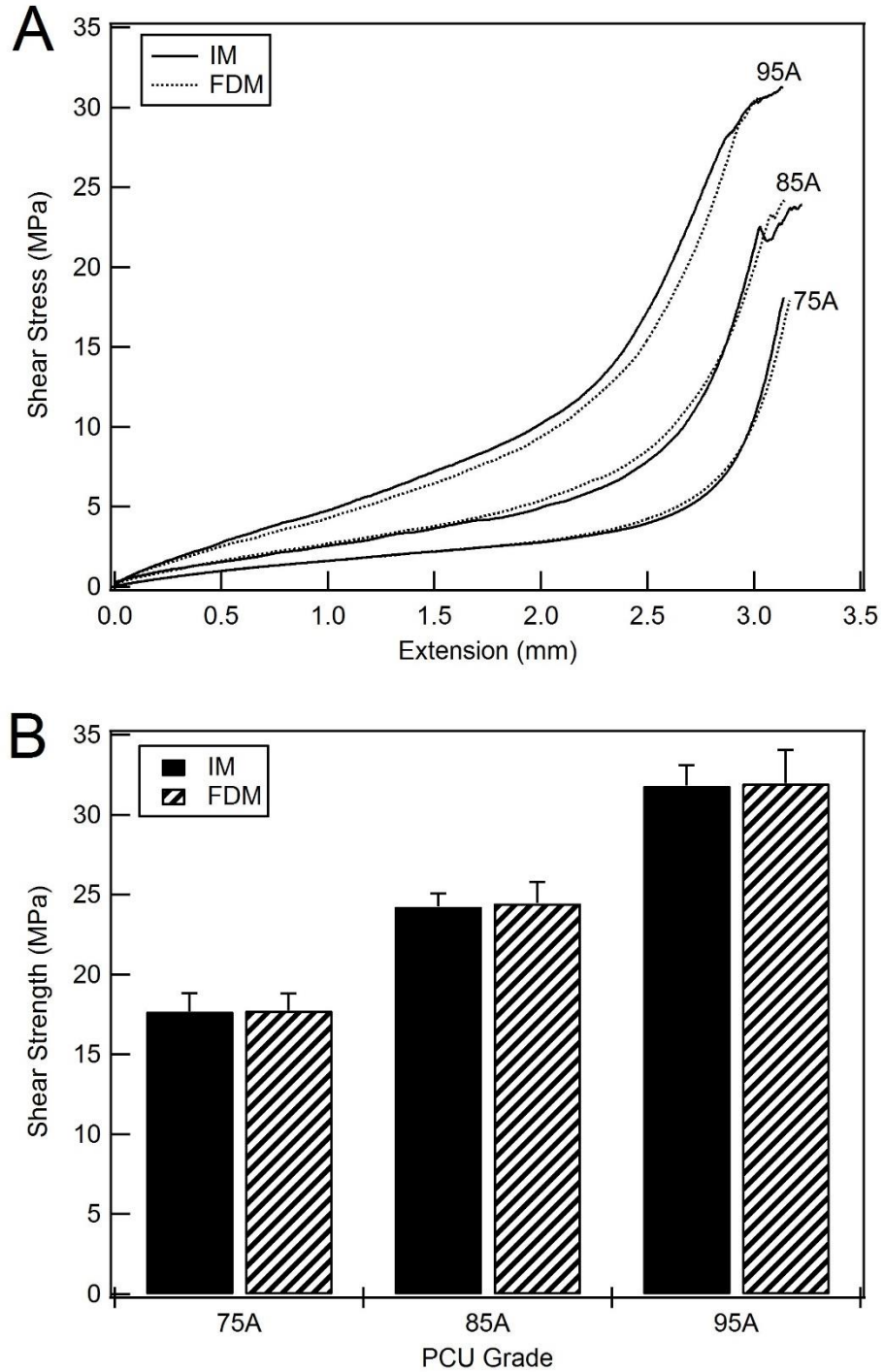


Figure 4.15: Median plots of shear stress versus extension for each grade and processing method (A). Average maximum shear stress for IM and FDM PCU, error bars indicate standard deviation ( $n = 6$  for each grade and processing method) (B). Increased HSC leads to significantly increased shear stiffness and shear strength ( $p < 0.0001$  for all comparisons). No significant differences in strength or stiffness between IM and FDM samples.

#### 4.3.4 Fatigue testing

Fatigue life data for IM samples is shown in Figure 4.16. Figure 4.16A shows the fatigue life data based on strain amplitude and indicates subtle differences between grades suggesting a relative order of performance of 85A followed by 75A and then 95A. This result matches up well with monotonic tensile failure strains for these materials. Runouts at 1 million cycles were successful at strain amplitudes of: 33.3% and 34.5% (75A), 41.7% and 50% (85A), and 18.2% and 26.9% (95A). Figure 4.16B shows the same IM fatigue data plotted against the maximum cyclic tensile stress at each sample's median life. Median life stress was used due to the stress relaxation exhibited by these materials under strain-controlled loading, an example of which is shown for each grade in Figure 4.17. Figure 4.16B clearly shows difference between the grades, with a relative order of performance of 95A followed by 85A and then 75A when plotted against stress amplitude. Median stress values for the runouts at 1 million cycles correspond to: 1.52 and 1.61 MPa (75A), 1.79 and 2.33 MPa (85A), and 2.87 and 3.63 MPa (95A). Figure 4.17, which shows the peak tensile stress as a function of cycle for each grade, illustrates the extent of stress relaxation during cyclic testing. Based on this figure, it is clear that the stress relaxation increases with increasing hard segment content for these three grades of PCU.

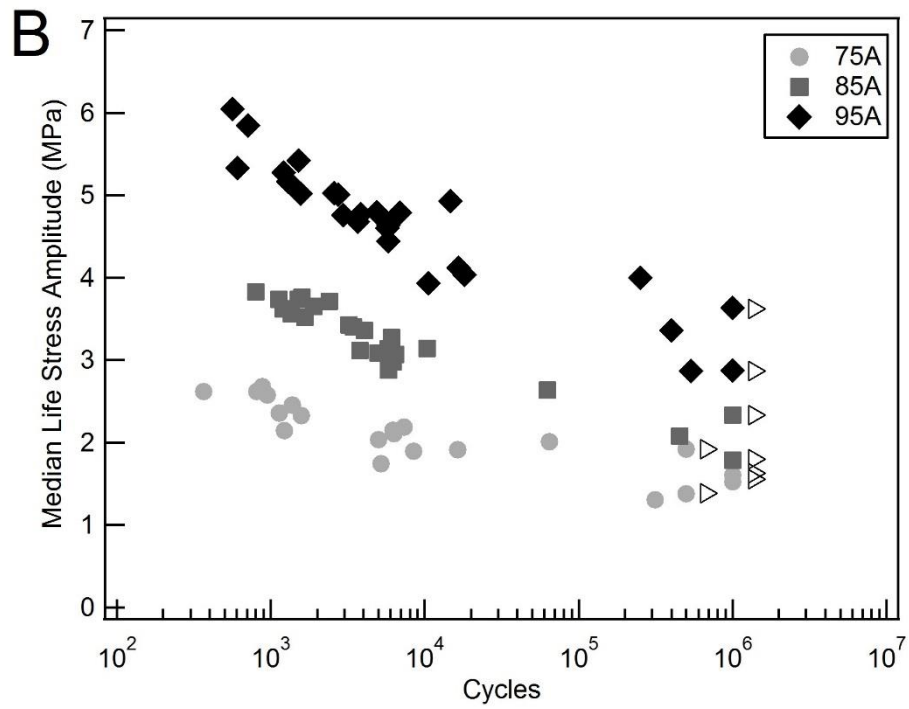
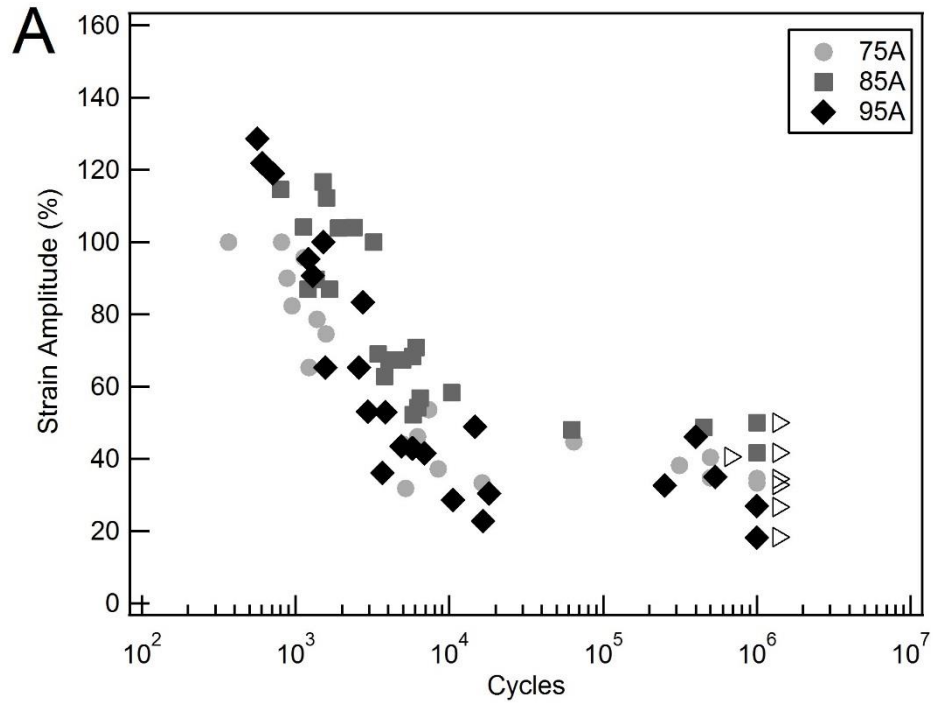


Figure 4.16: IM fatigue data based on strain amplitude (A) and median life tensile stress amplitude (B).

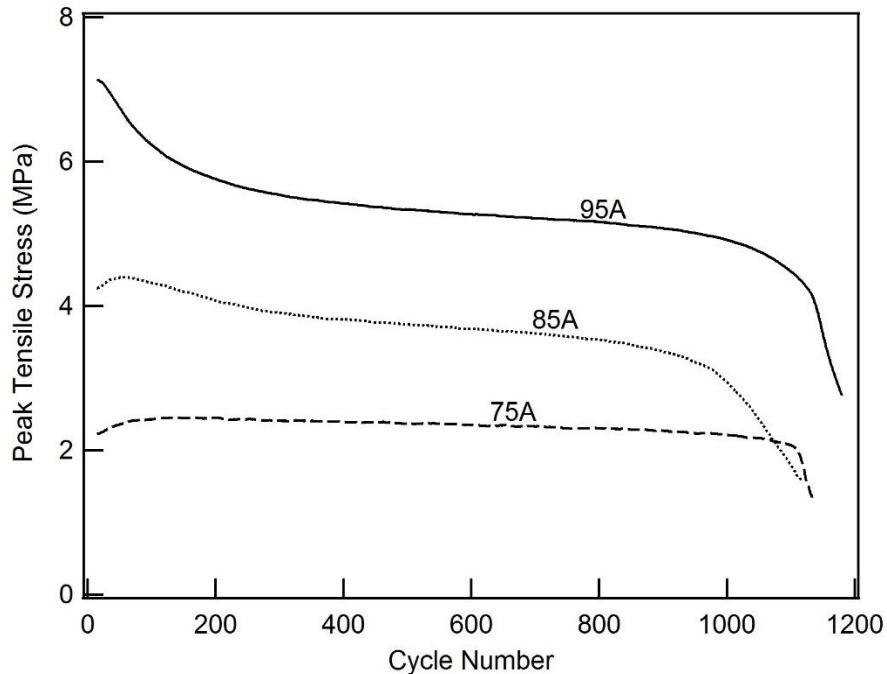


Figure 4.17: Peak tensile stress as a function of cycle number for IM samples of each grade lasting between 1,000 and 1,200 cycles.

Fatigue life data for FDM samples are shown in Figure 4.18 plotted against their IM counterparts. Void fractions from microCT scans of FDM fatigue samples ranged from 0.9937 to 0.9998, and showed a similar distribution as monotonic samples as shown in Figure 4.2. For reference, microCT scans of IM fatigue samples showed an average solid fraction of over 0.9996. Runouts at 1 million cycles for FDM samples were successful at strain amplitudes of: 33.3% and 38.9% (75A), 50% and 60.4% (85A), and 19.6% and 33.3% (95A). These correspond to runouts at median life stress amplitudes of: 1.78 and 1.78 MPa (75A), 2.28 and 2.77 MPa (85A), and 3.35 and 3.66 MPa (95A). Figures 4.18 A, B, and C indicate that FDM samples not only matched IM, but in some cases outperformed IM samples in fatigue based on strain amplitude. While the increased failure strain of monotonic tension results may provide foundation for this, the result is still surprising as



many of the FDM fatigue samples contained voids. Figure 4.18D shows the fatigue data for all samples plotted against median life stress amplitude. Stress-life data on a log-log scale was analyzed via linear regression with a dummy variable as explained in Section 4.2.7. The dummy variable was set to a value of 0 for IM samples and 1 for FDM samples. The resulting dummy variable coefficients for intercept (x-axis) were positive (1.3, 5.5, and 5.7 for 75A, 85A, and 95A, respectively). Dummy variable coefficients for slope were negative (-2.8, -10.1, and -7.8 for 75A, 85A, and 95A, respectively). These results indicate that FDM sample data is not only shifted to higher cycles but also shows a lower slope on the stress-life fatigue plot within the range analyzed. However, the coefficient values were significant only for the 85A and 95A grades ( $p < 0.0001$ , both coefficients, 85A and 95A). SEM images of the fracture surfaces for IM and FDM samples are shown in Figure 4.19. Both samples had a fatigue life between 400,000 and 500,000 cycles, and the fracture surfaces look remarkably similar despite the surface roughness evident on the side of the FDM sample.

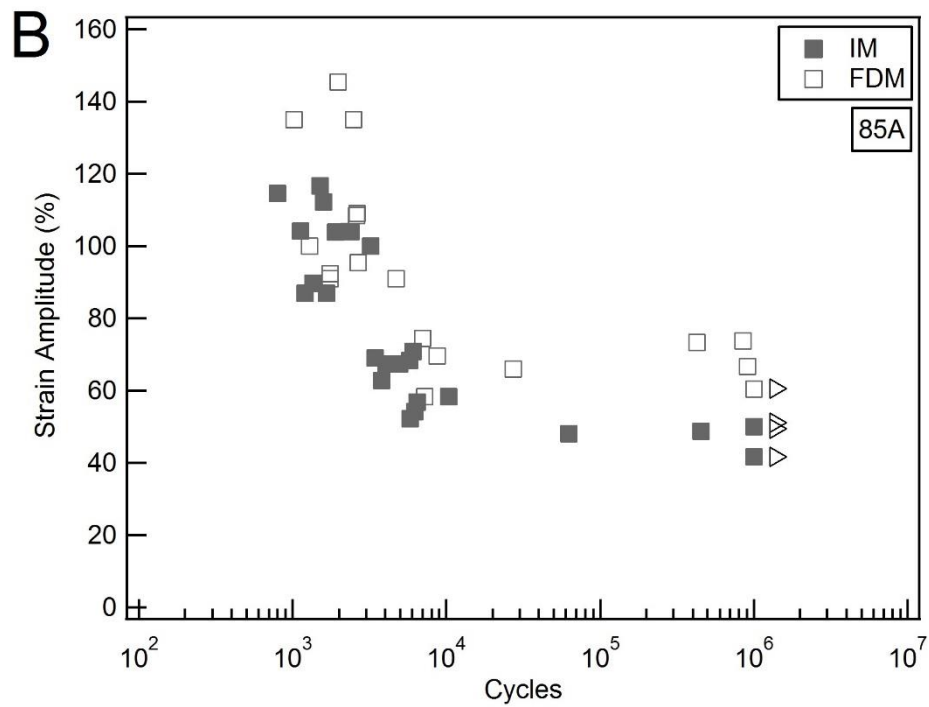
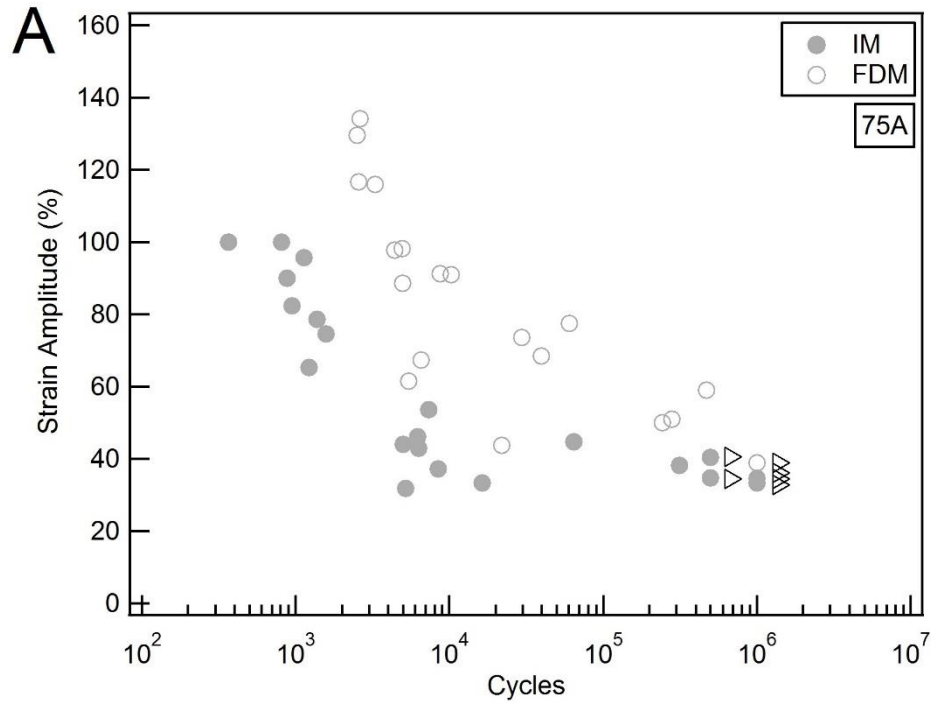


Figure 4.18: FDM fatigue data shown against IM counterparts for 75A (A & D), 85A (B & D), and 95A (C & D). Plotted against strain amplitude (A, B, C) and against median life stress amplitude (D). FDM 85A and 95A stress-based data (D) show significantly greater x-axis intercepts and lower slopes vs. IM varieties ( $p < 0.0001$  for all).

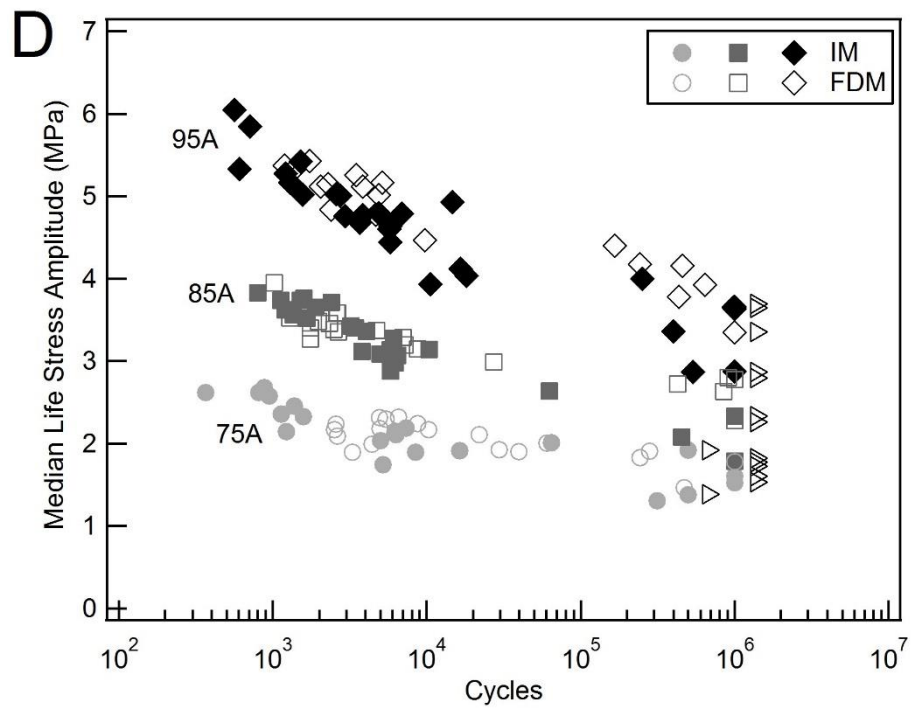
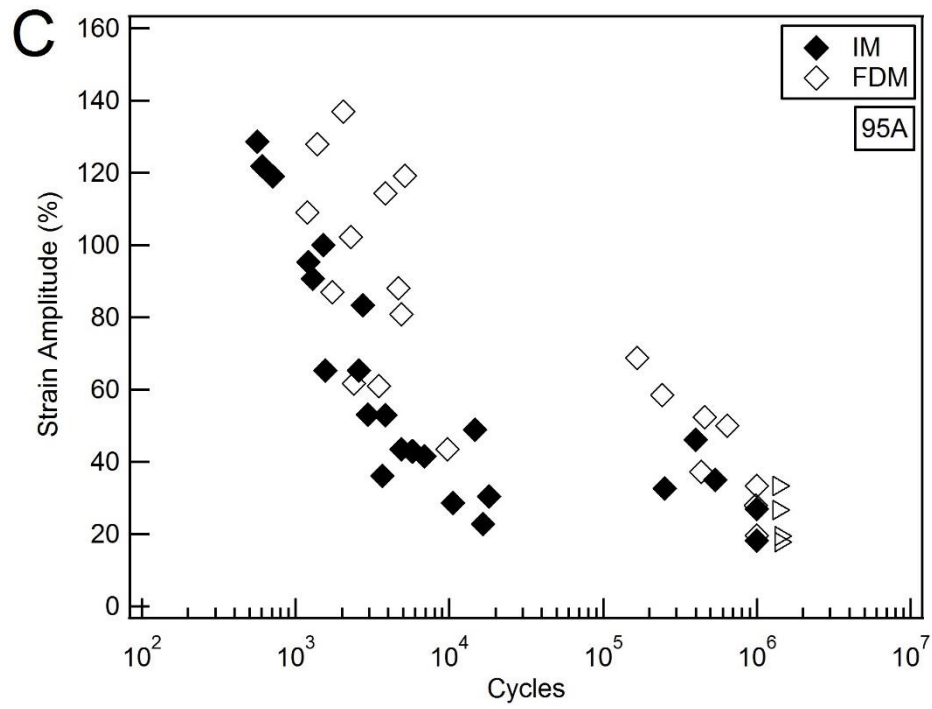


Figure 4.18: Continued

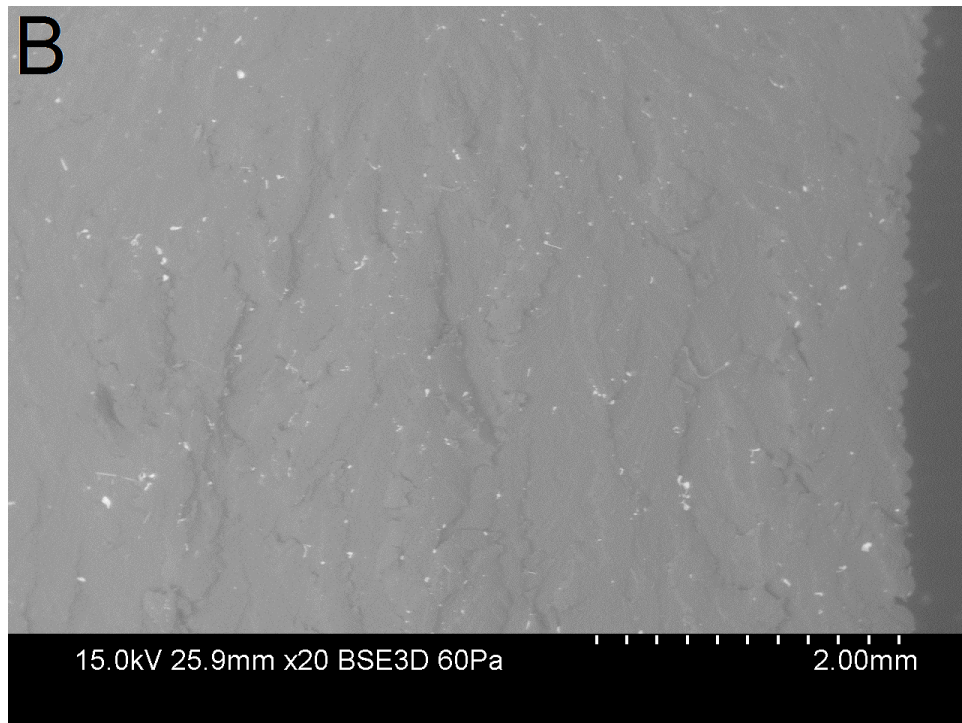
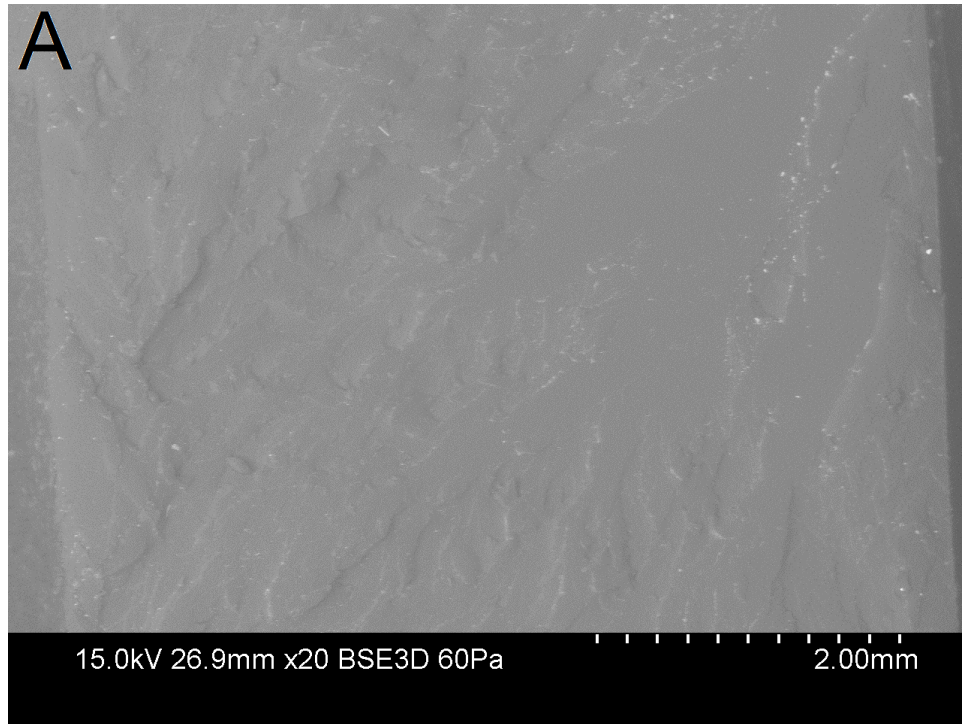


Figure 4.19: SEM images of fatigue sample fracture surfaces for IM (A) and FDM (B) samples.

#### 4.4 Discussion

PCU has shown promise in a number of applications in recent years including many load-bearing, orthopedic applications such as intervertebral disc and meniscus replacements. Some of these devices are currently in US clinical trials, while many are already in use in Europe, such as the: TriboFit® Hip System, Elastic Spine Pad® disc replacements, and NUsurface® Meniscus Implant. Preclinical testing and early clinical results for these devices have been promising, however long term results have yet to be seen and will depend in part on the material's fatigue resistance. While preclinical device testing may suggest suitability of these devices in meeting the load-bearing demands *in vivo*, the work does little to advance the fundamental science and understanding of how PCU structure relates to performance. In fact, fundamental studies relating PCU structure, or even TPU structure in general, to fatigue performance represents a surprisingly understudied field in the published literature. Fundamental knowledge of this sort would allow for optimization of materials and may potentially give these devices a better chance of success in the long-term. As such, one objective of this work was to better understand the relationship between PCU structure and mechanical performance, particularly fatigue, through testing of PCUs with systematically varied hardness. In addition, we studied the effects of FDM on the mechanical properties of PCU due to the potential benefits such processing could offer, such as custom device design and complex porous structures.

The results allow us to draw several observations in relation to these objectives; however first, it is prudent to adequately characterize the structure and make-up of each PCU grade tested. This can be accomplished by comparing results with those obtained by Eceiza et al. in which PCUs of varying hard segment content and soft segment molecular

weight were extensively characterized through DSC and DMA [88].  $^1\text{H}$  NMR results (Section 4.3.1.3) have confirmed the use of the same hard and soft segments as used by Eceiza et al., and while their testing parameters were somewhat different than the present study, the comparison will nevertheless allow for approximate material structural and chemical characterization. First, comparing tan delta peak location (Table 4.2 of the present study and Table 2 of Eceiza et al.) suggests a soft segment molecular weight (MW) of roughly 1K for 95A and between 1K and 2K for 75A and 85A. The lack of soft segment melting transitions on DSC plots ( $T_{ms}$ , Eceiza Fig. 3) indicates that 75A and 85A do not likely use 2K MW and confirms a MW between 1K and 2K. This is further confirmed by a lack of  $\alpha_c$  inflection on tan delta plots (not shown), which indicates that none of the studied PCUs show soft segment crystallinity. Tan delta peak values in the present study were roughly 0.84, 0.47, and 0.29 for the 75A, 85A, and 95A grades of PCU, respectively. Comparison with Figure 2 of Eceiza et al. indicates these values correspond to hard segment contents (HSCs) of less than 30% for both 75A and 85A, and roughly 48% for 95A. Careful comparison of modulus data (Fig. 4.6A of present work, Fig. 2a of Eceiza et al.) as well as Shore hardness (Table 4 of Eceiza et al.), indicates a HSC of 37% to 48% for 95A. Comparing Shore hardness data for 85A and 75A indicate HSCs of roughly 20% and less than 20%, respectively. As discussed in Section 4.3.1.1, DSC data confirms the relative order of HSC of: 75A, 85A, and then 95A with the highest. With this characterization, we are able to draw the following observations from the results of the present work.

Our first observation is that an increase in PCU HSC leads to an increase in monotonic stiffness, increase in shear failure stress, and improvements in tensile fatigue

from a stress-based standpoint despite lacking a strong effect on monotonic tensile strength for the examined hardnesses. Effects of HSC on tensile failure strain, and strain-based fatigue performance, were more complex and seemingly influenced by interaction between phases. The monotonic stiffness observation is somewhat obvious, and is illustrated in Figure 4.13D as well as by comparison of Figure 4.13 A, B, and C. As the HSC increases, the initial slope upon loading, as well as the plateau modulus for tensile tests, both increase. Comparison of Figure 4.13 A, B, and C also indicates that the length of the plateau region decreases with increasing HSC. This indicates a diminished ability for reorientation of soft segment chains under load with increasing HSC, and therefore diminished elastomeric behavior. Interestingly, when comparing the tensile performance of 75A and 85A (Table 4.4, Figure 4.13 A & B), the difference in HSC did not result in a significant difference in either tensile failure stress or strain. This is perhaps due to the small difference in HSC between these grades. However, careful comparison of Figure 4.13 A & B reveals that the general tensile behavior is different. The 75A grade demonstrates a lower initial and plateau modulus, however exhibits the most dramatic (highest slope) strain-induced hardening of all three grades. This likely indicates soft segments chains that are relatively free to reorient and crystallize upon loading due to low HSC when compared to 85A and 95A. While the failure stress and strain of 85A are not significantly different from 75A, the net effect of the difference in loading behavior means 85A has a higher monotonic toughness than 75A. Compared to 75A and 85A, the 95A grade had a significantly lower tensile failure strain as expected, but a tensile failure stress that was not significantly different than either. As mentioned by Eceiza et al., whose monotonic results are in general agreement, greater phase separation (confirmed in Section 4.3.1.4) can lead to sharper

phase boundaries and a localization of stress which seems to balance out the improvement due to increased HSC [88]. In contrast to the tensile failure stress, which was not significantly different between the three grades tested, the shear failure stress shows clear, and significant differences between grades. Average shear failure stress values were 17.7 MPa, 24.2 MPa, and 31.3 MPa for 75A, 85A, and 95A, respectively. Results were consistent and support the observation that increased HSC leads to increased shear failure stress for PCU. In comparison with the tensile data, this suggests that the soft segments are less capable of reorienting and improving the strength of the initially soft (low HSC) materials under shear loading.

While results indicate that the tensile failure strain of the 75A and 85A grades of PCU were not significantly different, fatigue results (Figure 4.16A) suggest that 85A outperforms 75A in terms of strain-based tensile fatigue. This result is somewhat surprising considering the similarity in monotonic results, as well as the beneficial effects of strain crystallization on fatigue properties of TPUs [229]. It is likely this difference is due to energy dissipation mechanisms as the 85A grade has a higher loss modulus (Figure 4.6B) at the testing temperature than the 75A grade. Energy dissipation in PCUs is often attributed to hydrogen bonding and the degree of hydrogen bonding in PCUs is largely affected by hard segment content due to presence of urethane groups [52, 84, 88]. Comparing the strain-based fatigue performance of 85A to 95A indicates that again 85A has slightly better fatigue resistance, despite 95A having the higher loss modulus. However, this result is not surprising considering the significant reduction in tensile failure strain of the 95A grade compared to 85A. Close examination of data from Eceiza et al. (Table 4) indicates that tensile failure strain is largely driven by HSC and not soft segment



MW [88]. Considering this, these results suggest there is a trade-off in strain-based fatigue performance for PCU, and that is that as HSC increases the ability to dissipate energy increases but at the cost of a reduction in strain tolerance. While strain-based fatigue results suggest only slight differences in performance between PCU grades, expressing this data in terms of stress rather than strain shows very clear differences (Figure 4.16B). Since fatigue testing was done in a strain-controlled fashion, and such testing results in considerable stress relaxation for viscoelastic polymers (example shown in Figure 4.17), Figure 4.16B was created by plotting the sample life against the stress amplitude at each samples' median life. From this plot it is clear that the relative order of performance from lowest to highest is 75A, 85A, and then 95A. While this result was expected, it is still interesting considering the insignificant differences between grades in tensile failure stress. Despite the potentially sharper phase boundaries that govern monotonic failure, 95A outperforms 85A and 75A likely due to energy dissipation effects attributed to the hard segment. Also worth noting is the relative extent of stress relaxation between grades as shown in Figure 4.17. From this figure it seems a higher HSC leads to increased stress relaxation, an expected result due to relative viscoelastic behavior.

Our second observation is that FDM represents a very effective processing method for PCU. This observation is based on the relative insensitivity of tensile monotonic properties and tensile fatigue performance to the presence of a small percentage (< 1%) of voids. In addition, shear tests have demonstrated strong interlayer strength for FDM samples on par with IM controls. In fact, FDM samples matched or exceeded IM samples across the board in monotonic tension/compression, shear, and fatigue tests. Comparison of monotonic results between IM and FDM samples (Table 4.4) indicates that while FDM

samples of each grade matched their IM control in terms of failure stress, the failure strain was significantly larger for FDM samples in each case. The increase in tensile failure strain is accompanied by an enhancement in strain crystallization (Figure 4.14) and an apparent improvement in strain-based tensile fatigue (Figure 4.18).

The source of this slight difference between IM and FDM samples is not immediately clear. The simple presence of voids is not a likely cause as monotonic tensile dogbone samples ranged up to 0.9995 solid fraction and demonstrated similar behavior as samples as low as 0.9876 solid fraction. A large-scale alignment effect induced by processing of the FDM samples was suspected; however, tensile tests on dogbones with all lines printed parallel to the loading axis (not shown) demonstrated nearly identical behavior as the  $\pm 45^\circ$  infill samples used in this study. Instead, it is likely the discrepancy is due to subtle phase separation and organizational differences between IM and FDM samples. This assertion is supported by DSC and DMA data (Figures 4.5 & 4.6, Table 4.2). Careful examination of Figure 4.5 shows a very subtle but consistent and statistically significant leftward shift in  $T_{gs1}$  between IM and FDM samples that appears to increase in magnitude with HSC ( $p = 0.0409, 0.0002, <0.0001$  for 75A, 85A, and 95A, respectively). This observation is supported by similar leftward shifts in DMA plots (Figure 4.6) that are more dramatic and again increase in magnitude with HSC. Temperature shifts in tan delta peaks between IM and FDM samples (not shown) are significant for the 85A and 95A grades ( $p = 0.0004, 0.0032$  for 85A and 95A, respectively). These results suggest better phase separation for FDM samples [88], however this assertion is not supported by FTIR data (Section 4.3.1.4). Perhaps the most obvious discrepancy between FDM and IM DMA data is the apparent abbreviation of thermal effects above  $25^\circ\text{C}$  which appears more dramatic

with decreasing HSC. This suggests that hard domains in FDM samples are perhaps smaller or less developed than their IM counterparts, leading to quicker transitions as temperature increases above 25°C and a faster drop in storage modulus. Such an effect could also explain the differences in monotonic tension behavior as smaller and less developed hard domains would be more mobile and able to reorient under loading leading to greater overall chain mobility. This would lessen the strain hardening effect, yielding greater strain for a given stress within the strain hardening region, and apparently enhance strain crystallization as seen in Figure 4.14. Increased chain mobility would also explain the relative improvement in strain-controlled fatigue for FDM versus IM samples, as would an increase in the ability to undergo strain crystallization [229]. This effect on hard domains could potentially be a result of differences in processing temperature, a faster cooling rate, and/or a shorter rest time after processing for FDM versus IM samples [229, 230]. Work by Pompe et al. found that processing temperature, and not method, had a large effect on resulting TPU morphology and tensile failure strain. Higher processing temperatures led to preferential formation of so-called “type I” hard domain crystallites which are smaller than the “type II” crystallites formed at lower processing temperatures [230]. This effect could lead to the differences in failure strain seen in this study as FDM samples were generally printed at temperatures higher than the processing temperatures for IM samples. Another possibility is the difference in cooling rate, as printed FDM lines cool almost immediately upon printing, whereas the 6 mm thick IM sheet stock likely took considerably longer. IM samples were also tested roughly two months following molding, whereas FDM samples were tested one to four weeks following printing. It is possible that the difference in behavior may be recovered following further aging, as the phase separation process has

been found to take up to two months for PCU [231]. However, the behavior of PCUs in this study was found to stabilize just two days after printing (Section 4.3.1.5). In addition, FTIR data shows similar degrees of phase separation between FDM and IM samples after 1 week (Section 4.3.1.4). A follow-up study was conducted (Chapter 6) to determine if FDM samples better match IM samples following changes to printing temperature, aging duration, or annealing.

The difference between IM and FDM samples leads to our last discussion point, which is that while FDM has proven to be a very effective processing method for PCU, additional considerations are warranted as with any new processing method. With FDM PCU, there is a clear structural evolution following printing in which the hard and soft phases separate. The timescale of this process was shown to be highly dependent on hard segment content, with the monotonic behavior of the softest material (75A) taking longest to level out. This process is illustrated by monotonic tension tests shown in Figures 4.10 and 4.11, and was verified to be a phase separation process utilizing FTIR (Figure 4.12). However, despite the seemingly stabilized monotonic tension behavior, FDM samples still exhibited a larger failure strain and improved strain-based fatigue performance compared to IM counterparts. This is likely due to phase separation or organizational differences caused by differences in the processing methods (Chapter 6). Nevertheless, this study has demonstrated that FDM is a viable processing method for PCU in that samples can be printed to perform at least on par with IM controls.

To the best of the authors' knowledge, no prior examples of FDM materials matching injection molded controls currently exist in the literature. The success of FDM samples in this study is certainly due in part to the use of printing parameters which were

carefully tailored to minimize the amount of voids and maximize contact between adjacent lines and layers. This is accomplished by extruding a large volume of material relative to the nozzle height, which allows the extruder nozzle to spread the material into adjacent lines rather than printing round lines which will inherently include voids. Whether PCU has any intrinsic material properties that make it a good candidate for FDM remains yet to be seen as the current body of work on FDM materials is extremely limited.

In closing, it is worth comparing the results of the selected PCUs with other relevant materials. Monotonic tension results are on par with Bionate 80A, another commercially available PCU [56]. Compared with polyether urethanes (PEUs) of similar hardness, PCU demonstrates similar tensile strength but lower failure strain, as soft PEUs typically reach over 500% strain [56, 71]. Compared with polyisobutylene-based thermoplastics and conventional silicone rubber, PCU demonstrates roughly five times the tensile strength but again at a cost of lower failure strain [151]. While some fatigue data exists on TPUs in general, comparisons are difficult to make due to vastly different sample geometries, loading modes, and testing parameters. Similar zero-to-tension, strain-controlled fatigue data was developed for a UV cured, material jetted elastomer. Comparison of fatigue data suggests the three grades of PCU considered in the present work are superior in strain-based tension fatigue [162]. This is especially likely considering that the UV cured polymer did not undergo stress reversal due to the use of slender samples.

#### **4.5 Conclusions**

We have investigated the mechanical properties and fatigue performance of three PCUs with systematically varied hard and soft segment contents, processed using both

injection molding and 3D printing (fused deposition modeling). The following are the conclusions of the work.

1. Increased PCU hard segment content leads to an increase in monotonic stiffness, increase in shear failure stress, and improvements in tensile fatigue from a stress-based standpoint despite lacking a strong effect on monotonic tensile strength for the examined PCUs. Effects of hard segment content on tensile failure strain, and strain-based fatigue performance, were more complex and seemingly influenced by interaction between phases.
2. FDM represents a very effective processing method for PCU based on the apparent insensitivity of tensile monotonic properties and tensile fatigue performance to the presence of a small percentage ( $< 1\%$ ) of voids. FDM samples matched or exceeded injection molded sample performance in terms of monotonic tension, compression, shear, and tensile fatigue likely due in part to favorable printing parameters.
3. Additional considerations are warranted for FDM PCU, as with any new processing method, due to differences in strain behavior. The effect is likely due to differences in microphase separation or organization.

A potential limitation of this study is not including fatigue samples whose layers were perpendicular to the specimen axis. This is often thought of as the worst-case scenario for 3D printed parts and was not included due to an inability to print tall samples in a standing configuration with flexible materials. However, the shear performance of FDM samples presented indicates that the printing parameters resulted in very strong interlayer bonding, and no evidence of layer delamination was seen during testing. In fact, SEM images of IM versus FDM fatigue sample fracture surfaces (Figure 4.19) are nearly

indistinguishable, indicating a very solid infill for FDM samples with adequate bonding between lines and layers. In addition, when printing final parts with FDM, layering direction is often considered and generally layers are not aligned perpendicularly with expected tensile stresses when possible. The use of a buffered saline bath, rather than a more biologically active and relevant solution, represents another limitation. However, the purpose of this study was to develop relationships between PCU structure and fatigue performance. An extensive body of work exists on the degradation of PCU in oxidative and hydrolytic environments, although no fatigue data has been found. A follow-up study investigating the effects of oxidation on the fatigue properties of PCU can be found in Chapter 6. Finally, the use of a laser cutter to form IM fatigue samples introduces another variable when comparing IM to FDM sample fatigue performance and represents another limitation. To address this, a follow-up study investigating the effect of laser cutting on FDM sample fatigue performance is presented in Chapter 6. Results indicated that laser cutting has no significant effect on PCU sample fatigue performance, therefore justifying its use.

## CHAPTER 5

### EFFECT OF PRINTED ARCHITECTURE ON THE MECHANICAL PROPERTIES AND FATIGUE PERFORMANCE OF POLYURETHANES

#### 5.1 Introduction

In our previous studies, we examined the toughness and fatigue performance of a particular PU, polycarbonate urethane (PCU), as a function of both hard segment content and processing via injection molding or 3D printing (fused deposition modeling). The material demonstrated considerable toughness in both compressive and tensile fatigue loading (Chapters 3 & 4). In addition, solid 3D printed samples matched or exceeded the performance of injection molded counterparts in terms of tensile and compressive monotonic properties, shear strength, and tensile fatigue performance (Chapter 4). While the results for the 3D printed solid specimens were on par with injection molded materials, there are many biomedical applications that may require or benefit from the inclusion of pores or three-dimensional architectures.

Recent advancements in fabrication techniques, specifically 3D printing, have enabled the construction of more complex, tailored scaffolds and architectures. Designer scaffolds have been found to sometimes better reproduce the mechanical properties of the associated tissue, as well as provide better biologic results, than those made from traditional methods such as porogen leaching [232]. While the majority of work with these polymer scaffolds pertains to bioresorbable varieties [232-234], permanent implants will also benefit from the addition or use of such architectures. However, the fatigue performance of such scaffolds must first be investigated, as existing work has demonstrated a significant detrimental impact on fatigue performance with the inclusion of pores or architectures in



materials such as PEEK and Ti-6Al-4V. Therefore, the objective of this study is to understand the impact of architecture on the fatigue performance of printed PUs through systematic testing of a variety of biomedically relevant architectures. It is our hypothesis that such printed architectures will be detrimental to fatigue performance and that increased porosity or notch severity (decreased notch radius or increased notch width) will lead to diminished fatigue performance (i.e. lower cycles to failure).

## **5.2 Materials and Methods**

### **5.2.1 Materials**

Materials for this study included the physically crosslinked Carbothane AC-4095A obtained from Lubrizol (95A) in pellet form, as well as a photo-cured, elastomeric, chemically crosslinked polyurethane with 68A hardness obtained from Carbon 3D (EPU40) in liquid resin form. For printed 95A samples, the pellets were first extruded into 3 mm printer filament following Lubrizol documentation. For injection molded (IM) 95A samples, the pellets were sent to Lansen Mold Co. Inc. and injection molded into 6 mm thick sheet stock using the mold, nozzle, front, middle, and rear temperatures as provided by Lubrizol documentation (18°C, 215°C, 210°C, 210°C, 205°C, respectively). EPU40 was used as-received. While the EPU40 material has not yet been demonstrated as a biomaterial in published literature, the Carbon 3D printer provides a distinct advantage in printing complex architectures over conventional fused deposition modeling printers (FDM). In addition, the presumably altered structure of the EPU40 material to accommodate chemical crosslinking, as well as the vastly different printing method, will make for a valuable comparison with the thermoplastic 95A material.

### 5.2.2 Architectures and processing

All tested architectures, for both monotonic and fatigue tests, are summarized in Table 5.1. In order to examine the effects of architecture on the fatigue performance of these materials, it was first necessary to develop monotonic and fatigue data on solid samples for both materials as a control. The fatigue data for IM and solid printed 95A samples, as well as the processing parameters for these samples, are obtained from our previous work (Chapter 4). The remainder of the data presented was developed in this study. Solid printed samples are simply denoted as 95A and EPU, whereas IM 95A samples are denoted as 95A-IM. Simple crosshatch scaffolds, consisting of layers of lines alternating direction by 90° per layer, were included as they represent a basic scaffold design that is popular biomedically due in part to the 100% interconnected porous architecture. In addition, crosshatch scaffolds are perhaps the simplest design to print and therefore are especially popular with FDM printers and bioplotters [235-244]. Crosshatch scaffolds of various line spacings were printed and tested with both materials, all having a constant line width of approximately 500-600 μm (round lines for 95A, square lines for EPU40 due to printing differences). A 500 μm perimeter was required with PCU crosshatch samples to maintain proper sample geometry, and was also included with EPU40 samples for consistency. Several spacings were chosen for each material that spanned the range of minimum to maximum possible values based on material and printing method. For the 95A material, maximum line spacing was limited by slumping of printed lines, while minimum spacing was limited by overlap and contact between lines. For the EPU40 material, maximum line spacing was limited by sample geometry, while minimum spacing was limited by machine resolution. Crosshatch samples are denoted by material type and the

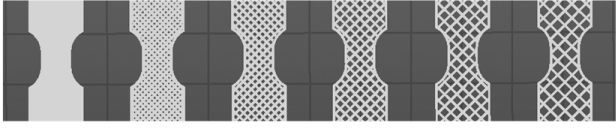
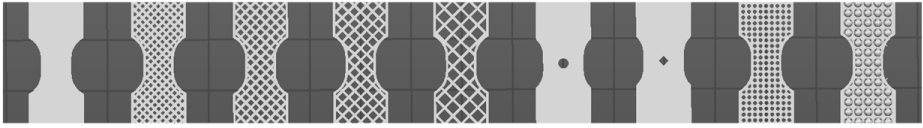
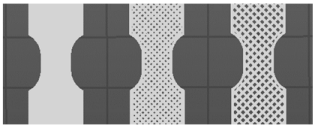
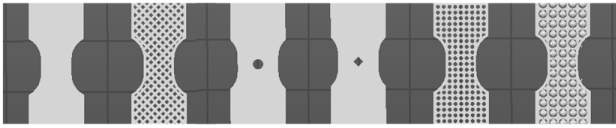
average overall porosity (eg. 95A-52 for crosshatch 95A with 52% porosity). Figure 5.1A shows an image of a crosshatch dogbone for both materials.

Two types of notched specimens were included for the EPU40 material to investigate the effects of pore geometry (Table 5.1 & Figure 5.1B). In this case, the diamond notch with sharp corners represents a more severe notch that is analogous to pores in cases such as simple crosshatches, as well as in samples processed via leaching of cubic salt crystals [179]. The circular notch represents a less severe notch that is analogous to pores in cases such as foamed materials and samples processed via leaching of spherical microbeads [245-247]. As was seen in the limited available research, notch severity can impact fatigue performance of elastomers [193], however in some cases the use of square pores may be unavoidable due to printing limitations. Both notches were designed with a constant 2 mm width. However, in order to match the cross-sectional area of printed solid specimens, the gage section for notched specimens was also widened by 2 mm. Notched samples are denoted as EPU-DIA and EPU-CIR for diamond and circular notches, respectively.

Finally, two additional advanced architectures (Table 5.1 & Figure 5.1B) were included for testing of the EPU40 material as its printing process is more suited for the creation of complex architectures as compared to FDM. The first architecture was made utilizing the so-called cylindrical pore unit cell. The unit cell consists of a cubic shape with cylindrical pores passing completely through in each of the three orthogonal directions. This scaffold design has been found to have superior permeability as compared to conventional spherical pores for a given porosity, and has demonstrated early promise as a bone scaffold [232, 233]. For our samples, we utilized a 1.125 mm cube with 0.75 mm

diameter cylindrical pores. The second advanced architecture was made utilizing a simple body centered cubic (BCC) arrangement of overlapping spherical pores. The BCC pore arrangement is a fundamental and conventional design that is analogous to architectures obtained through leaching of spherical microbeads. While both the BCC and cylindrical pore designs share a round pore geometry, they will provide an interesting comparison as the cylindrical pore geometry was designed to be superior to conventional scaffolds by maximizing mechanical properties and permeability for a given porosity. For our samples, we utilized 1.75 mm diameter spheres at a 0.975 mm spacing between layers giving a total BCC unit cell dimension of 1.95 mm. Both cylindrical pore and BCC specimens included a 500  $\mu\text{m}$  perimeter to maintain consistency with crosshatch specimens. The cylindrical pore samples are denoted as EPU-CP while the spherical BCC samples are denoted as EPU-BCC.

Table 5.1: Summary of tested architectures.

Test	Material	Architectures
Monotonic	95A	 95A    95A-18    95A-31    95A-45    95A-52    95A-59
	EPU40	 EPU    EPU-37    EPU-42    EPU-53    EPU-59    EPU-CIR    EPU-DIA    EPU-CP    EPU-BCC
Fatigue	95A	 95A    95A-18    95A-31
	EPU40	 EPU    EPU-37    EPU-CIR    EPU-DIA    EPU-CP    EPU-BCC

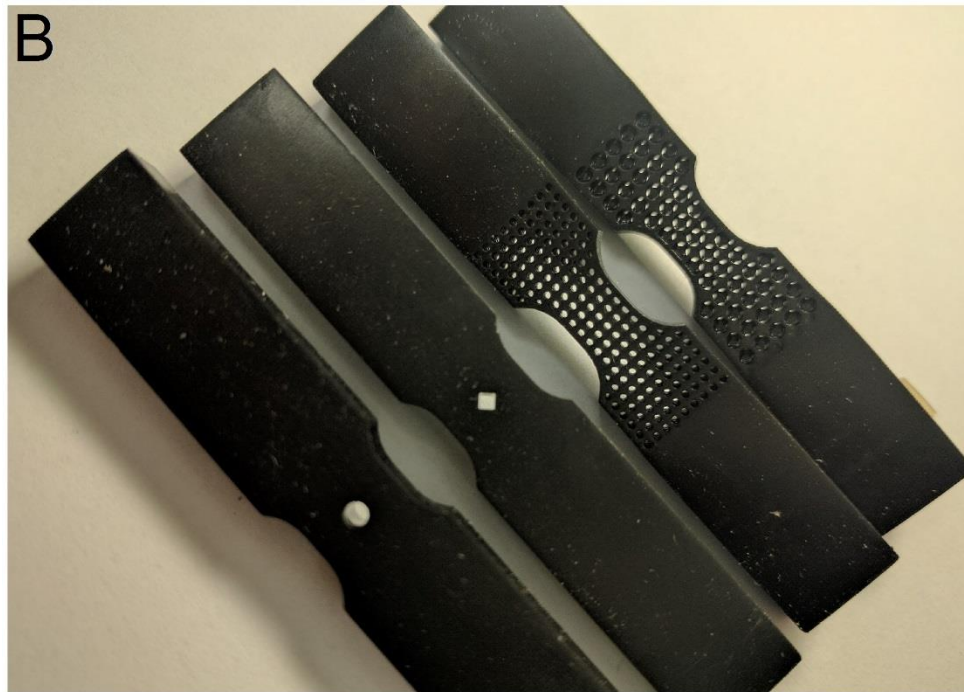
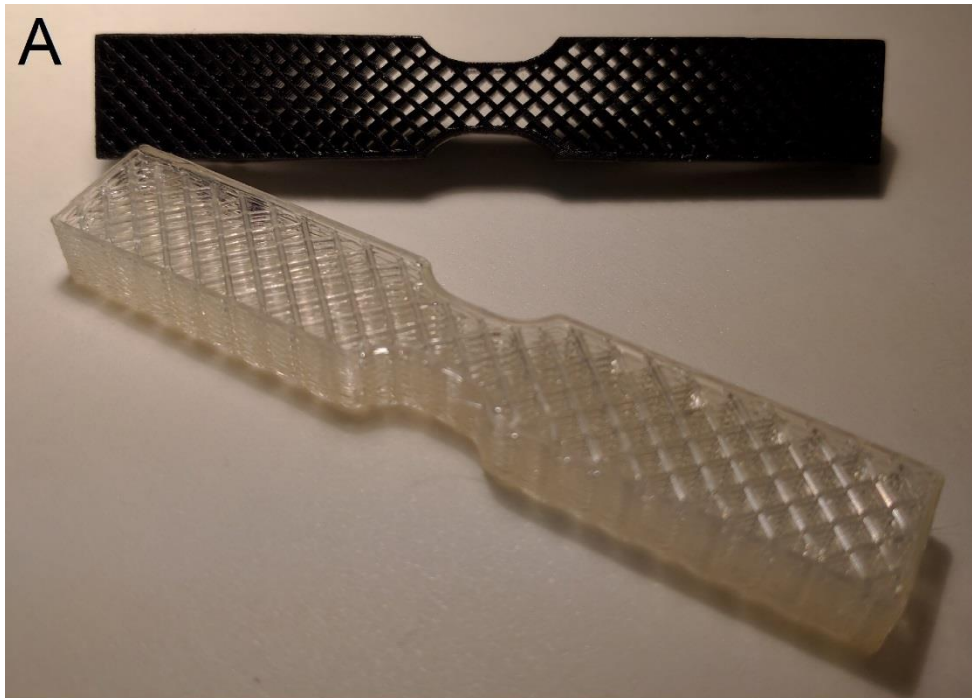


Figure 5.1: Image showing crosshatch samples of 95A and EPU40 (A) and notched as well as cylindrical pore and BCC architectures of EPU40 (B).

The materials were printed with the desired architecture, utilizing the following parameters and procedures, into the overall sample geometry shown in Figure 5.2 (note that dimensions differ for notched samples since the gage section was widened). The sample geometry was developed in our previous work (Chapter 4), and was found to give reliable tensile fatigue failures for compliant materials. For the 95A crosshatch samples, the printing filament was first dried for a minimum of 2 hours in a vacuum oven at 95°C and -25 inHg. The filament was then printed utilizing a Lulzbot TAZ 5 FDM printer (Aleph Objects, Inc.) equipped with a Flexystruder V1 tool head having a 0.5 mm nozzle. The sample model files were converted to G-code files utilizing Slic3r software. All 95A crosshatch scaffold samples were printed in a “lying down” fashion, with layers parallel to the specimen axis and width, and infill lines alternating  $\pm 45^\circ$  with the specimen axis by layer. For each layer, a single perimeter line was first printed to ensure maintenance of desired sample geometry, and infill lines were then printed with a 100% perimeter overlap. Samples were printed with a 0.4 mm layer height, 100% extrusion width, 1.75 extrusion multiplier, nozzle temperature of 205°C, and bed temperature of 40°C. Printing was conducted at a speed of 7 mm/sec, with external perimeters having a speed multiple of 50%. The given parameters were chosen as they consistently resulted in high quality crosshatch scaffolds with continuous lines of approximately 500  $\mu\text{m}$  in diameter and adequate bonding between layers. Nominal infill values varied between 15 and 45% to obtain different line spacings, however the actual infill percentages differed significantly (Section 5.3.1).

For the EPU40 samples, model files were automatically sliced utilizing Carbon 3D’s online software at a 100  $\mu\text{m}$  slice thickness, with samples oriented in a “lying down”

fashion. The EPU40 two-part resin was dispensed and mixed at the predetermined ratio using a dispensing gun. Files were then printed on the Carbon M1 printer utilizing the resin-specific settings for the EPU40 material, printing at a rate of approximately 10 mm/hr. Samples were removed from the build platform, washed in 99% isopropanol for 30 seconds, and then dried utilizing a centrifuge such that parts were not exposed to isopropanol for more than 1 minute. Finally, samples were heat treated in a convection oven at 120°C for 8 hours.

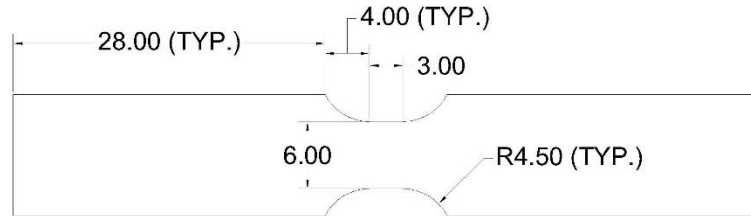


Figure 5.2: Custom dogbone geometry used in monotonic and fatigue tests. Samples were printed 6 mm thick. The gage section of notched specimens was widened by 2 mm to maintain the same cross-sectional area.

### 5.2.3 microCT and sample characterization

The gage section of the solid, crosshatch, and advanced architecture monotonic dogbone samples were scanned via microCT ( $\mu$ CT 50, Scanco Medical) to determine porosity (10  $\mu$ m voxel size, 55 kVp scanner voltage, 200  $\mu$ A current). Porosity was determined utilizing a threshold kept constant across all samples in the study ( $n = 3$  for each material and group). Crosshatch sample line width and clear spacing were analyzed via light microscope. Average porosities, as well as line width and spacing for crosshatch samples, are reported by material and architecture type ( $n = 3$  for all).



#### 5.2.4 Monotonic testing

Tensile monotonic tests were performed to determine the stress-strain behavior for all samples. Monotonic sample geometry is shown in Figure 5.2, and samples were printed as described in Section 5.2.2. Samples were tested until failure at a rate of 10 mm/min. All samples were measured using digital calipers immediately prior to testing and all tests were performed on an Instron materials testing machine (Model 5567). The average and standard deviation of failure stress and strain are reported for each material and architecture ( $n \geq 3$  for all). For notched samples, the strain measurement was taken across a 1 mm section centered on the plane bisecting the notch and represents an approximation due to the nonexistence of a uniform gage section. Stress was measured utilizing the actual load bearing area at the center of the notch and did not include the area of the notch. For the samples with architecture, strain was measured as the bulk strain across the entire sample gage section while stress was calculated using the gross sample area, not accounting for porosity. During the study, it was noted that samples with globally distributed architecture (architecture covering the gage, taper, and grip sections of the sample) performed notably different in fatigue than those with architecture covering solely the gage portion. To investigate this effect, monotonic tests were also performed on EPU40 crosshatch, cylindrical pore, and BCC samples in which the architecture was constrained to the gage section, with and without a perimeter. Localizing the architecture, and removing the perimeter, both serve to effectively soften the gage section relative to the taper and grips sections of the sample. In addition to monotonic tests, microCT scans were also taken of strained samples of global and localized EPU40 crosshatch samples as well as localized cylindrical pore and BCC samples. Scans were made utilizing the same parameters as

Section 5.2.3 with an in situ tensile grip apparatus holding at approximately 50% tensile strain.

#### 5.2.5 Fatigue testing

Cyclic tests were performed to develop fatigue life curves for selected architectures (see Table 5.1) utilizing the same procedures as our previous work (Chapter 4). Tests were performed in a displacement-controlled, zero-to-tension manner on the dogbone sample geometry shown in Figure 5.2. Tests were conducted at 5 Hz in a room temperature bath of phosphate-buffered saline (PBS, Sigma-Aldrich), and samples were allowed to soak in PBS for a minimum of 24 hours prior to testing. Specimen dimensions were recorded using digital calipers immediately prior to testing. All tests were performed on an MTS Bionix testing machine with a 15 kN load cell. Tests were recorded via video camera to determine the exact strain amplitude reached during cyclic loading, and strain amplitudes ranged from approximately 15% to 150% to develop the fatigue life curves. Strain was measured in the same manner as for monotonic tests (Section 5.2.4). Tests were run until complete rupture of the cross section, or runout at 1 million cycles. A total of 20 samples were used to develop each fatigue life curve, with a minimum of two reaching runout. Fatigue data for the IM and solid printed 95A samples is taken from our previous work (Chapter 4). During the study, it was noted that samples with globally distributed architecture (architecture covering the gage, taper, and grip sections of the sample) performed notably different in fatigue than those with architecture covering solely the gage portion. To investigate this effect, a sampling of fatigue tests were also performed on EPU40 crosshatch, cylindrical pore, and BCC samples in which the architecture was constrained to the gage section, with and without a perimeter. Fatigue life data is plotted against both strain amplitude as well

as median life stress amplitude. While the fatigue tests were conducted to a constant strain amplitude, plotting the same data against the stress amplitude at each sample's median life provides a means of comparing fatigue data from a stress-based standpoint.

#### 5.2.6 Statistical analysis

Comparisons between the tensile failure strain and stress of the samples were performed with a Student's t-test. Comparisons between sample fatigue performances were performed via linear regression with a dummy variable, as described in Section 4.2.7, on the fatigue data based on median life stress amplitude.

### **5.3 Results**

#### 5.3.1 microCT and sample characterization

Porosity data for the solid, crosshatch, and advanced architecture samples is summarized in Table 5.2. Average line width and clear spacing between lines is also reported for crosshatch samples. Samples demonstrated consistency in porosity with 95A crosshatch samples ranging from 17.9% to 58.9% porosity and EPU40 crosshatch samples ranging from 37.2% to 58.9% porosity. Solid printed 95A and EPU40 samples averaged below 2% porosity. Cylindrical pore EPU40 specimens reported 44.0% porosity, while the BCC spherical specimens reported 53.6% porosity. Clear line spacing for 95A crosshatch samples ranged from 100  $\mu\text{m}$  up to 1,580  $\mu\text{m}$ , while those for the EPU40 material ranged 740  $\mu\text{m}$  up to 1,680  $\mu\text{m}$ . Parametric views of the gage section of each sample type are shown in Figure 5.3.

Table 5.2: Porosity, crosshatch dimensions, and tensile data for all samples (n = 3).

Material	Sample	Porosity (%) (Average ± STD)	Line Width (μm) (Average ± STD)	Line Spacing (μm) (Average ± STD)	Failure Stress (MPa) (Average ± STD)	Failure Strain (mm/mm) (Average ± STD)
95A	95A	0.6 ± 0.3	N/A		43.5 ± 0.9	3.8 ± 0.1
	95A-18	17.9 ± 1.0	570 ± 30	100 ± 10	21.7 ± 0.4	3.1 ± 0.1
	95A-31	31.0 ± 1.4		320 ± 10	19.2 ± 0.2	3.2 ± 0.2
	95A-45	45.0 ± 0.6		660 ± 10	16.7 ± 0.4	3.2 ± 0.1
	95A-52	52.1 ± 0.2		1070 ± 30	15.8 ± 0.4	3.2 ± 0.1
	95A-59	58.9 ± 0.3		1580 ± 10	13.6 ± 0.6	3.2 ± 0.1
EPU40	EPU	2.0 ± 0.1	N/A		8.9 ± 1.1	3.2 ± 0.2
	EPU-37	37.2 ± 1.6	550 ± 20	740 ± 20	5.0 ± 0.3	2.7 ± 0.2
	EPU-42	41.9 ± 0.7		830 ± 40	5.3 ± 0.3	3.0 ± 0.1
	EPU-53	52.9 ± 1.6		1150 ± 50	4.5 ± 0.5	2.9 ± 0.2
	EPU-59	58.9 ± 0.7		1680 ± 60	3.7 ± 0.9	2.8 ± 0.5
	EPU-CIR	N/A	N/A		8.2 ± 0.4	2.9 ± 0.1
	EPU-DIA	N/A	N/A		7.4 ± 0.4	2.8 ± 0.1
	EPU-CP	44.0 ± 2.3	N/A		5.9 ± 0.6	3.5 ± 0.2
	EPU-BCC	53.6 ± 2.6	N/A		4.9 ± 0.9	2.9 ± 0.3

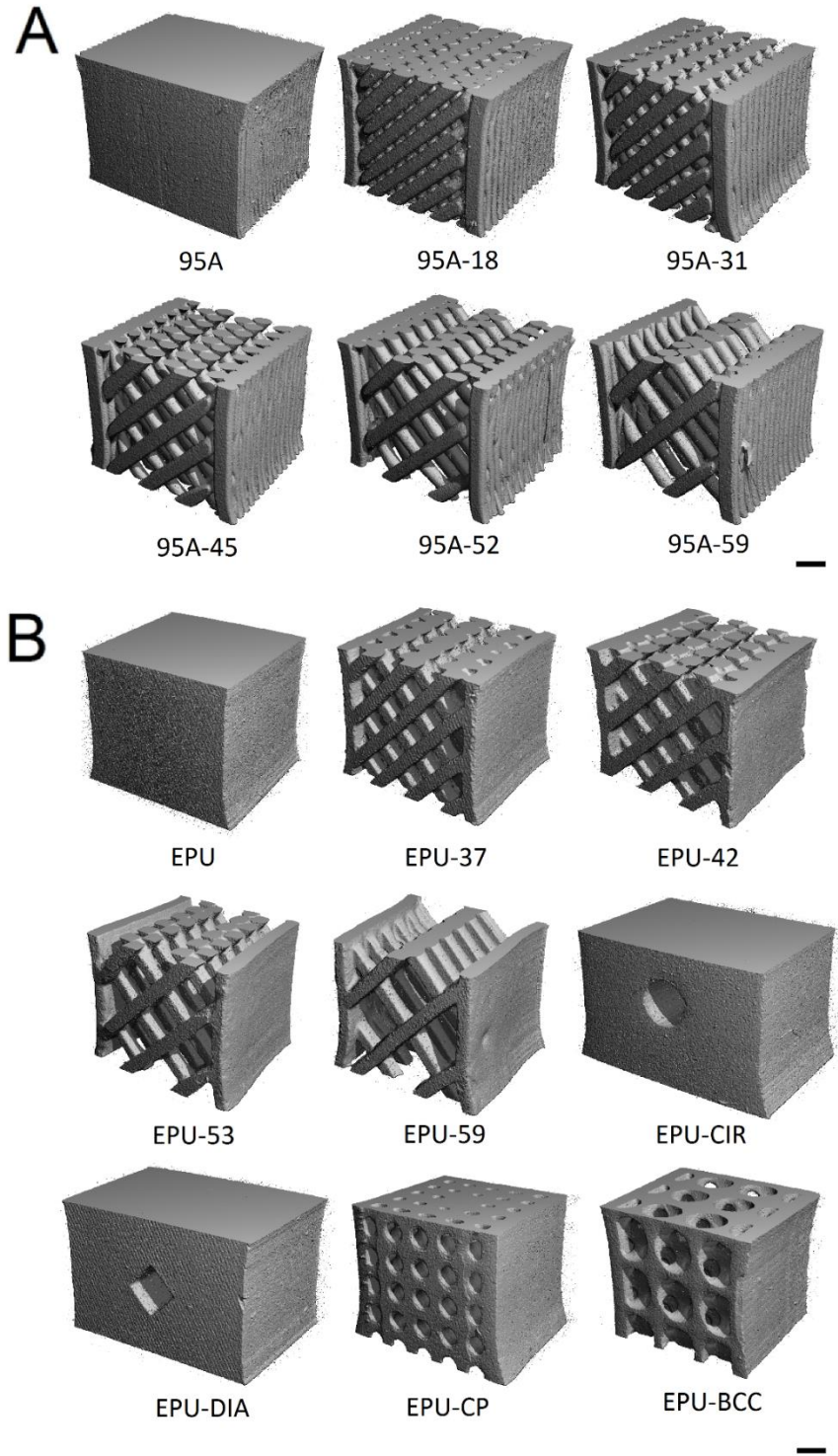


Figure 5.3: CT scan images showing 95A (A) and EPU40 (B) sample gage sections. Scale bar represents 1 mm.

### 5.3.2 Monotonic testing

Monotonic tension stress-strain curves are shown in Figure 5.4, all plots shown represent median plots based on failure stress. Tabulated tensile data is presented in Table 5.2. Similar to our previous work, IM 95A samples demonstrated significantly reduced failure strain as compared to the printed control ( $p = 0.0035$ ) but failure stress was not significantly different (Chapter 4). All 95A crosshatch samples demonstrated significantly reduced tensile failure stress ( $p < 0.0001$  for all) and failure strain ( $p \leq 0.0135$  for all) as compared to the solid printed control. However, as compared to the IM 95A data, only the failure stress was significantly less ( $p \leq 0.0007$  for all). As is illustrated in Figure 5.5, which shows the failure stress of crosshatch samples normalized to the maximum failure stress of the solid samples, failure stress decreased with increasing porosity as expected. However there were no significant differences in failure strain between any groups of 95A crosshatch samples. EPU40 crosshatch samples demonstrated a similar significant reduction in tensile failure stress ( $p \leq 0.0103$  for all) with no significant difference in failure strain as compared to solid samples. Figure 5.5 indicates a similar trend in normalized failure stress as a function of porosity for EPU40 crosshatch samples as compared to 95A. Circular and diamond notched EPU40 samples demonstrated no significant difference in failure stress or strain as compared to solid controls or with each other. EPU-CP and EPU-BCC samples demonstrated significantly reduced failure stress ( $p \leq 0.0274$ ) without a significant reduction in failure strain as compared to solid samples. Figure 5.6 shows representative monotonic tension stress-strain curves for EPU-37, EPU-CP, and EPU-BCC samples with architecture localized to the gage section, with and without a perimeter. The absence of a perimeter seems to reduce the overall stiffness of the EPU-37 and EPU-BCC samples as

expected. EPU-CP samples did not demonstrate a large difference likely due to the minimal difference in material volume the perimeter adds. Only the localized crosshatch samples demonstrated a significant difference in failure strain as compared to the global samples ( $p \leq 0.0263$ ). In addition, perhaps due to high variability, only the crosshatch samples without a perimeter demonstrated significantly reduced failure stress as compared to the two varieties with a perimeter ( $p \leq 0.0043$ ). Figure 5.7 shows CT images of the gage sections of strained global and localized crosshatch samples, as well as localized cylindrical pore and BCC spherical pore samples. Effective bulk Poisson's ratios were calculated as the negative of the ratio of transverse strain to longitudinal strain, and were found to be approximately 0.41, 0.27, and 0.32 for the global, local with perimeter, and local without perimeter crosshatch varieties. However, these numbers represent data from single samples and therefore significance cannot be determined.

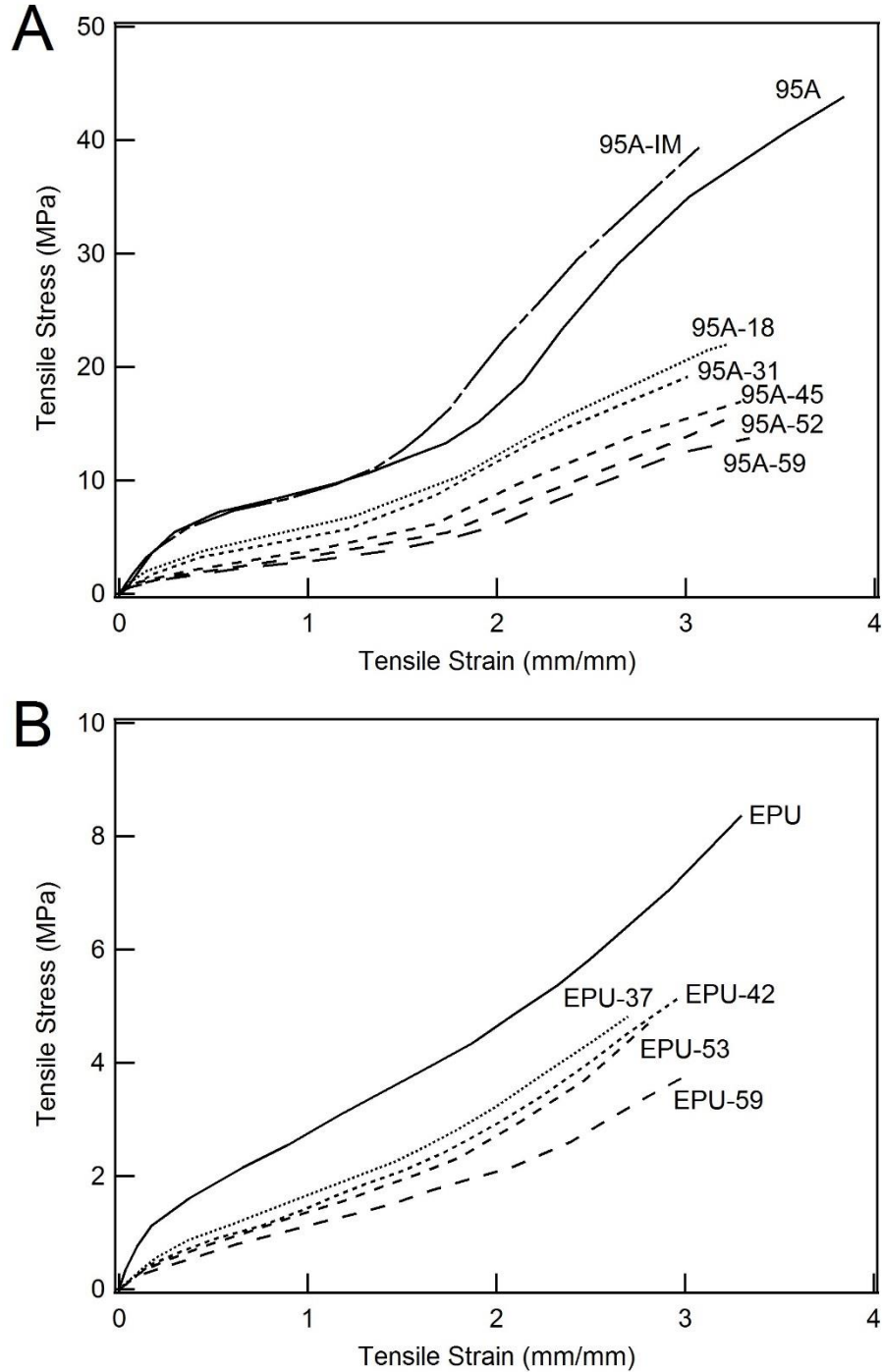


Figure 5.4: Monotonic tension results for 95A crosshatch samples (A), EPU40 crosshatch samples (B), and EPU40 notched and advanced architectures (C). 95A crosshatch samples show significantly reduced failure stress and strain versus solid samples ( $p \leq 0.0135$  for all). EPU crosshatch, EPU-CP, and EPU-BCC samples show significantly reduced failure stress ( $p \leq 0.0274$ ) with no significant difference in failure strain versus solid samples. No significant differences in failure stress or strain for EPU-CIRC or EPU-DIA notched samples versus solid samples.



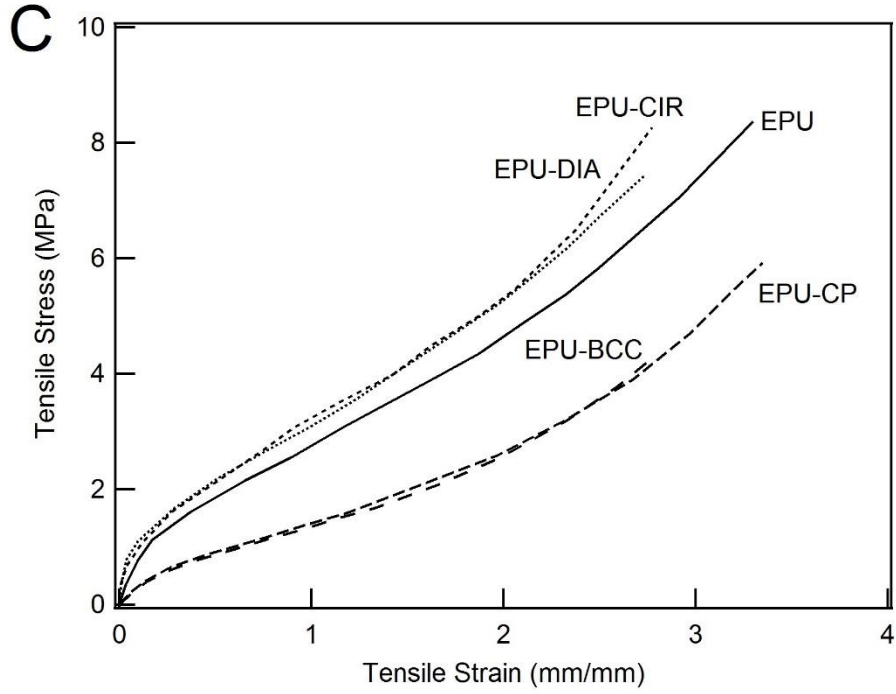


Figure 5.4: Continued

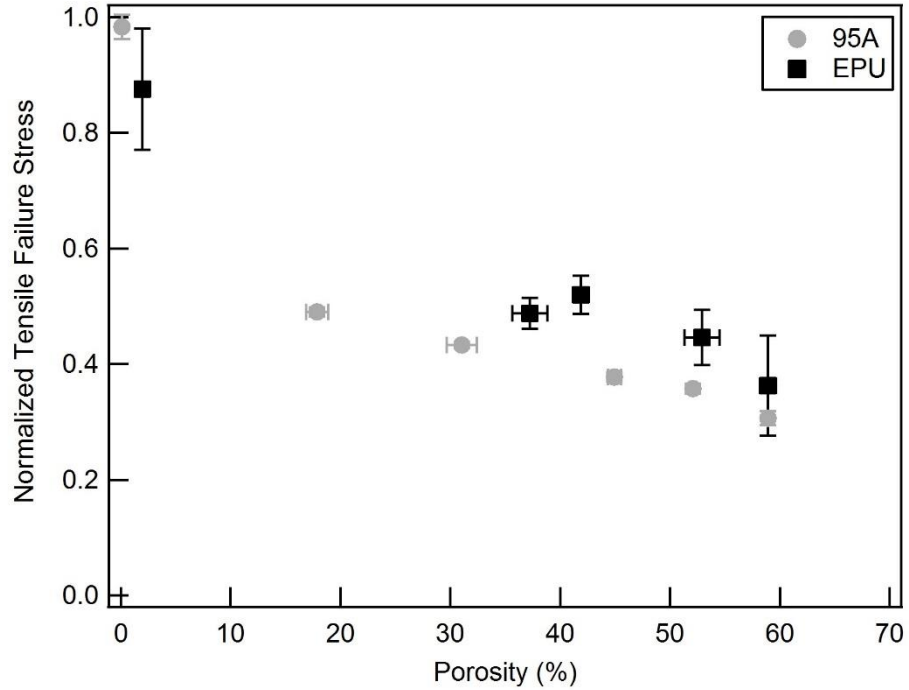


Figure 5.5: Normalized failure stress of crosshatch samples as a function of porosity. Data points represent the average of porosity and normalized failure stress for each sample group while the error bars represent standard deviation.

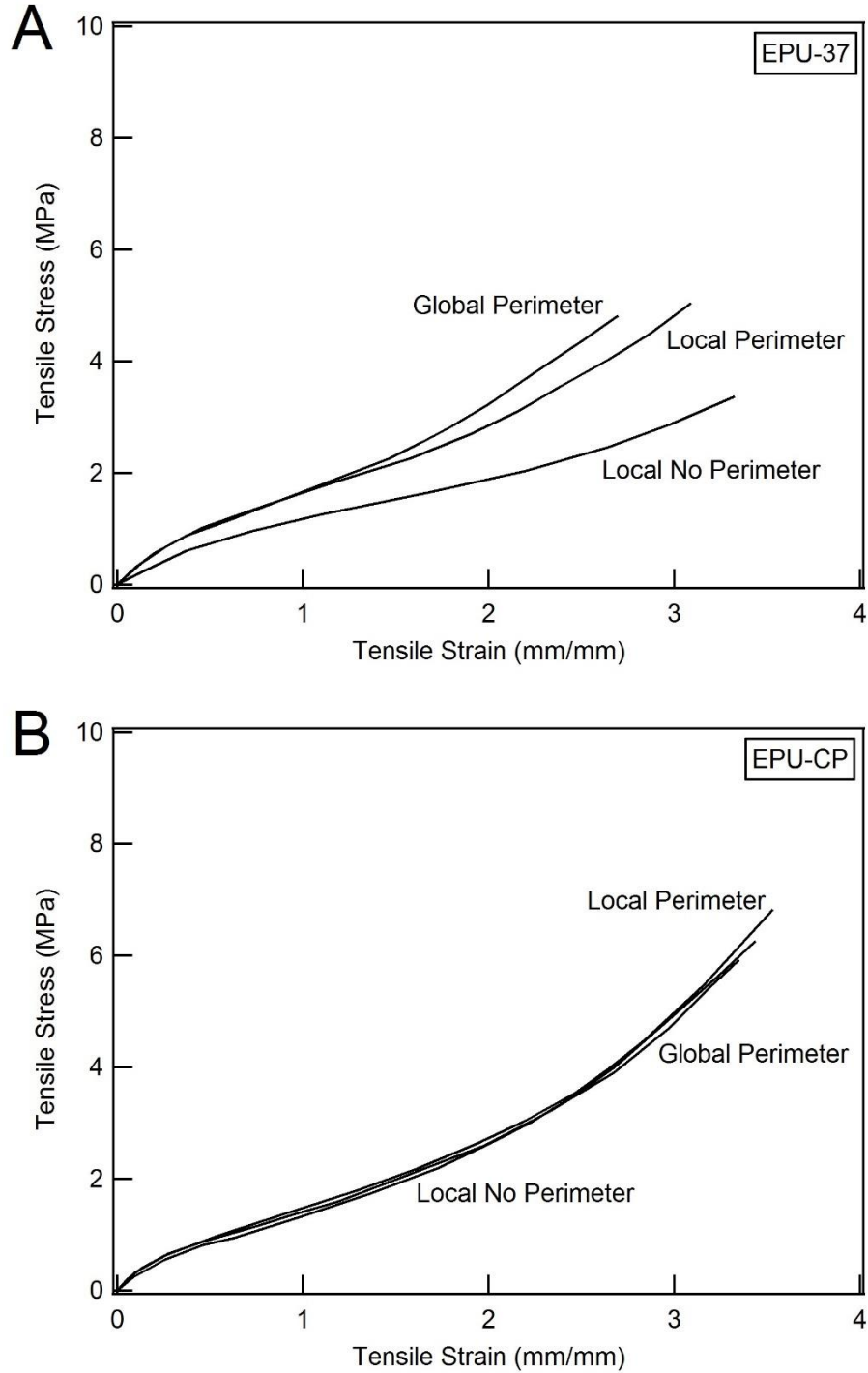


Figure 5.6: Monotonic tension results for EPU-37 (A), EPU-CP (B), and EPU-BCC (C) with architecture printed globally versus localized to the gage section only, with and without a perimeter. Localized EPU-37 samples display significantly increased failure strain versus the global variety ( $p \leq 0.0263$  for both). Local EPU-37 samples without a perimeter display significantly reduced failure stress versus both varieties with a perimeter ( $p \leq 0.0043$  for both).

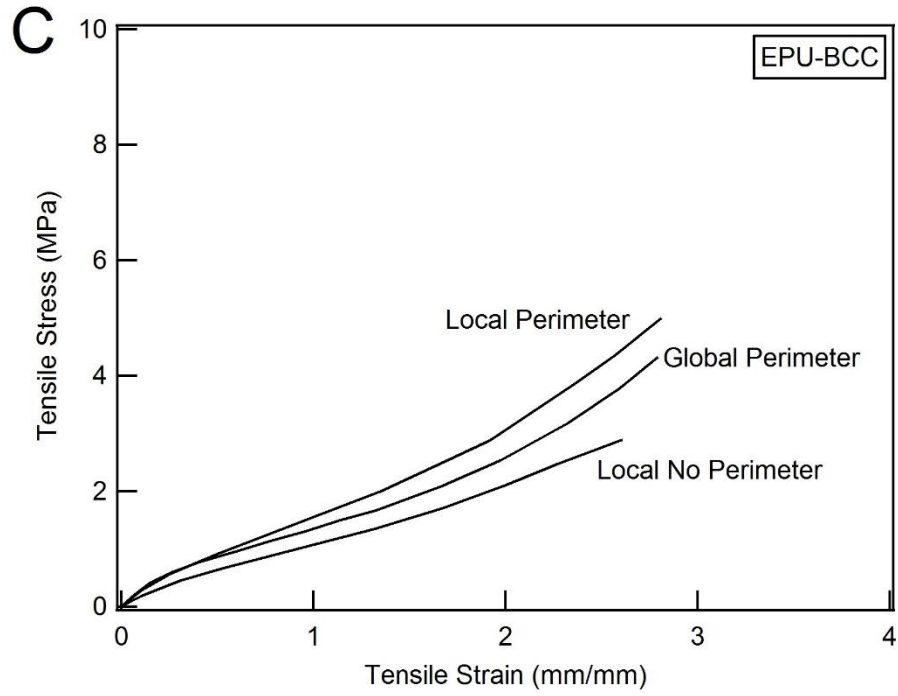


Figure 5.6: Continued

**A**

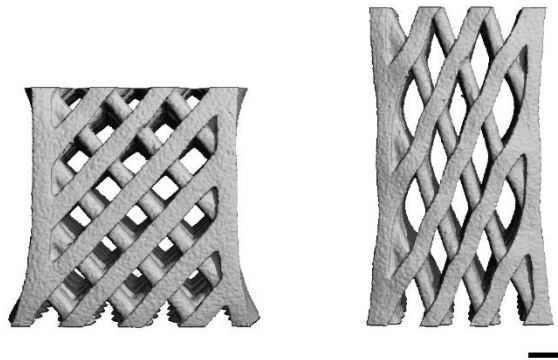
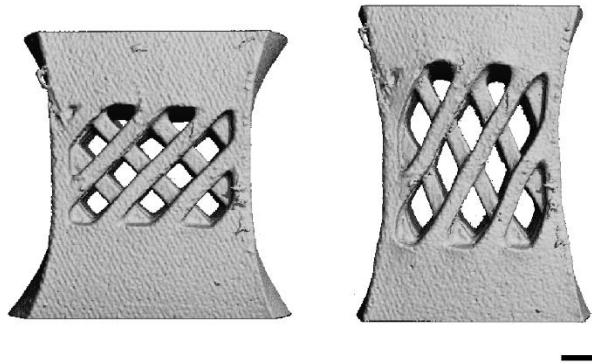
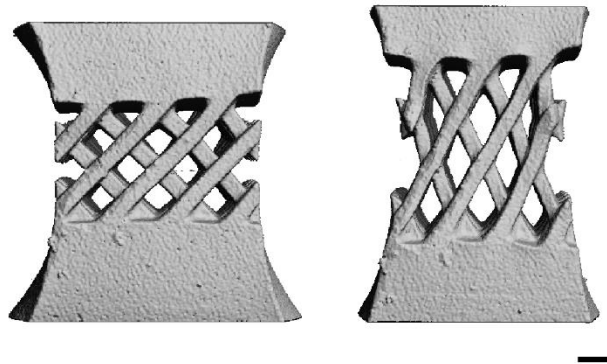


Figure 5.7: CT scan images of EPU40 global crosshatch (A), local crosshatch with perimeter (B) and without (C), cylindrical pore (D), and BCC spherical pore (E) samples at rest and under tensile strain. Strained samples are shown at approximately 50% tensile strain. Scale bar represents 1 mm.

B



C



D

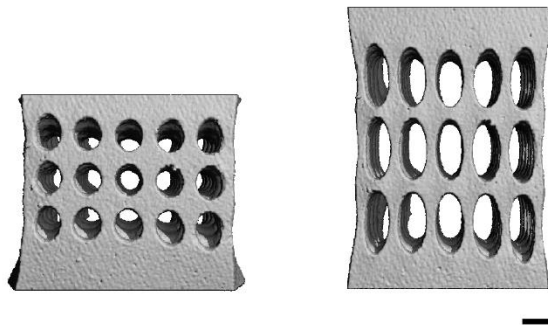


Figure 5.7: Continued

E

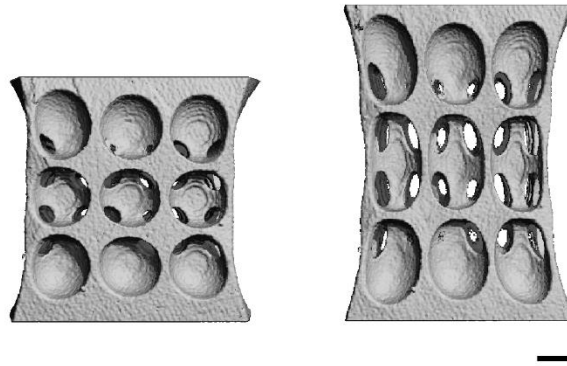


Figure 5.7: Continued

### 5.3.3 Fatigue testing

Fatigue data for the IM, solid printed 95A samples, as well as two crosshatch varieties, is shown in Figure 5.8. Figure 5.8A shows fatigue life versus strain amplitude, and indicates that both crosshatch varieties performed similarly from a strain-based standpoint but did not match the performance of the solid printed control. Interestingly, the strain-based crosshatch sample fatigue data matches closely with the IM data. Runouts at 1 million cycles were successful at strain amplitudes of 17.6% and 18.1% for 95A-31, 16.7% and 17.1% for 95A-18, 18.2% and 26.9% for 95A-IM, and 19.6% and 33.3% for the solid printed 95A.

Figure 5.8B shows the same fatigue data in terms of median life stress amplitude and shows much clearer differences. Comparing the crosshatch stress-life data to the solid printed 95A data via regression analysis returns negative dummy variable coefficients for x-axis intercept (-10.4 and -11.0 for 95A-18 and 95A-31, respectively) and positive dummy variable coefficients for slope (13.1 and 13.6 for 95A-18 and 95A-31, respectively). These

results indicate that crosshatch samples are not only shifted to lower cycles, but also show a steeper slope on the stress-life fatigue plot within the analyzed range ( $p < 0.0001$  for all coefficients). Comparing 95A-31 to 95A-18 returns a negative dummy variable coefficient on x-axis intercept ( $-0.6$ ,  $p = 0.0137$ ), indicating that 95A-31 demonstrates a significant shift towards lower cycles, but no significant effect on slope of the data. Runouts at 1 million cycles were successful at median life stress amplitudes of 0.95 MPa and 0.98 MPa for 95A-31, 1.12 MPa and 1.31 MPa for 95A-18, 2.87 MPa and 3.63 MPa for 95A-IM, and 3.35 MPa and 3.66 MPa for the solid printed 95A. Figure 5.8C shows the stress-life fatigue data with the crosshatch samples now adjusted by their solid fraction percentages. For example, the 17.9% porous 95A-18 data points were adjusted by dividing the stress amplitude by 82.1%. The plot indicates a modest, but incomplete recovery of the crosshatch fatigue data towards the solid printed control. Regression analysis still indicates significantly negative dummy variable coefficients on x-axis intercepts ( $-9.9$  and  $-10.2$  for 95A-18 and 95A-31, respectively,  $p < 0.0001$  for both) which confirms that adjusted crosshatch data still exhibits a shift towards lower cycles versus the solid control. However, comparing the two crosshatch varieties indicates that there is now no significant difference in intercept or slope between the two adjusted data sets.

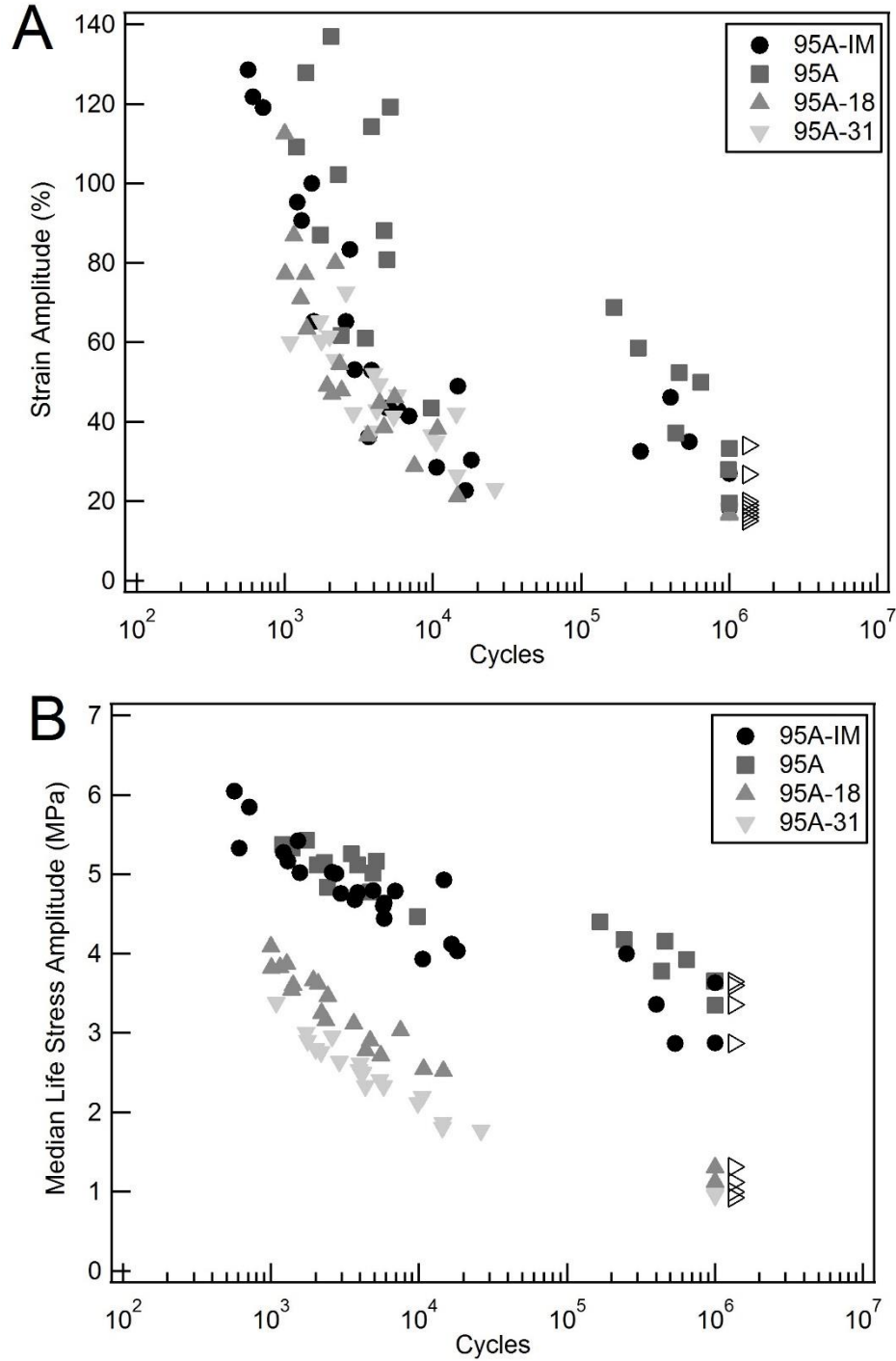


Figure 5.8: Fatigue data for solid and crosshatch 95A samples in terms of strain amplitude (A) and median life stress amplitude (B). C shows median life stress amplitude fatigue data after adjusting for crosshatch sample solid fraction percentages. Crosshatch varieties demonstrate significantly decreased x-axis intercept and increased slope for stress-based data (B) when compared to solid samples ( $p < 0.0001$  for all), even when adjusted by solid fraction (C) ( $p < 0.0001$  for all).

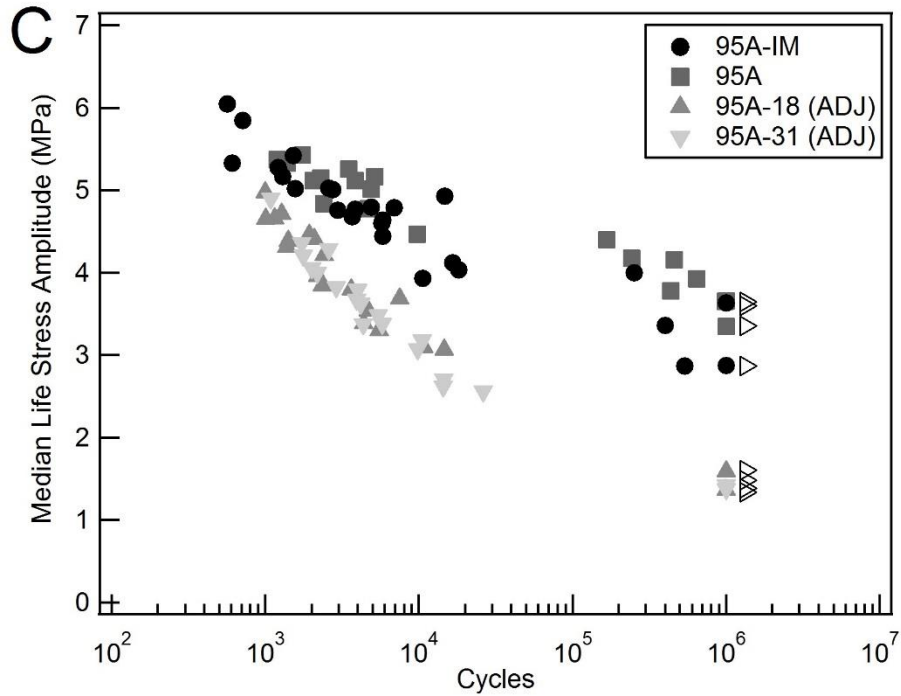


Figure 5.8: Continued

Fatigue data for the notched EPU40 specimens is shown in Figure 5.9 plotted against the solid printed control. Figure 5.9A shows the fatigue data plotted against strain amplitude and indicates that the circular notch performed on par with the solid control, while the presence of a diamond notch may have proven detrimental to strain-based fatigue performance. However, caution is warranted when interpreting the strain-based fatigue data due to the lack of a uniform gage length for notched samples. Measured strain amplitudes represent a reasonable approximation that may differ from the actual strain amplitude reached in the plane of the notch. Runouts at 1 million cycles were successful at strain amplitudes of 44.6% and 51.9% for the circular notch, 29.6% and 31.8% for the diamond notch, and 57.4% and 59.6% for the solid printed control. Figure 5.9B shows the



notched specimen fatigue data plotted against median life stress amplitude and indicates similar performance for all three sample types. Comparing the data via linear regression reveals no significant difference in intercept or slope for either type of notch as compared to the solid printed control. Runouts at 1 million cycles were successful at median life stress amplitudes of 0.87 MPa and 0.94 MPa for the circular notch, 0.74 MPa and 0.88 MPa for the diamond notch, and 0.76 MPa and 0.82 MPa for the solid printed control.

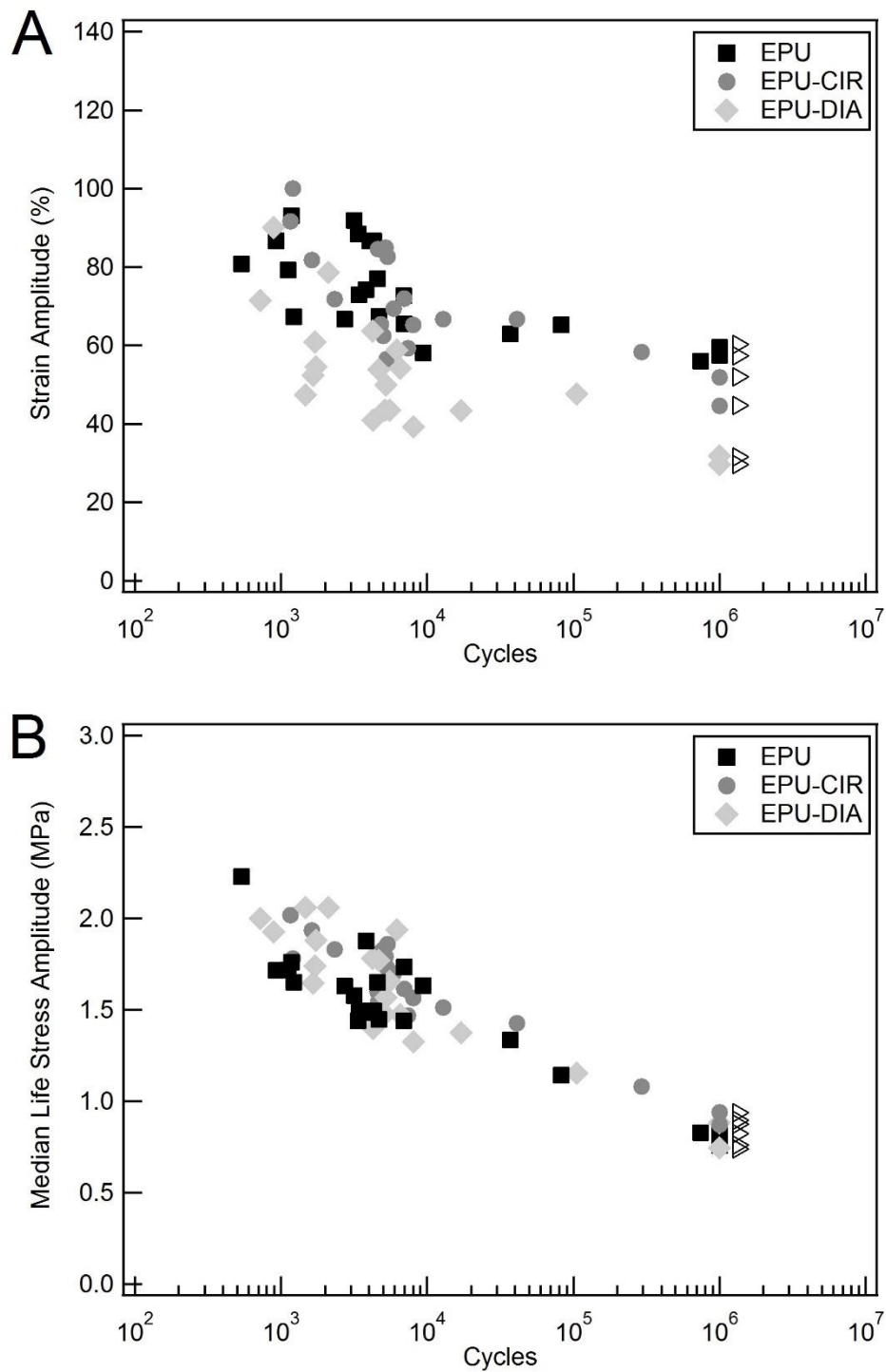


Figure 5.9: Fatigue data for notched specimens of EPU40 versus solid control in terms of strain amplitude (A) and median life stress amplitude (B). No significant differences in intercept or slope of stress-based data (B) were found for either notched sample versus the solid samples.

Fatigue data for the crosshatch, cylindrical pore, and BCC spherical pore EPU40 specimens is shown in Figure 5.10 plotted against the solid printed control. Figure 5.10A shows the fatigue data plotted against strain amplitude and indicates that the crosshatch architecture may have had a detrimental impact on strain-based fatigue while the cylindrical pore and BCC architectures seemingly had less of an effect, if any. Runouts at 1 million cycles were successful at strain amplitudes of 34.5% and 42.9% for the crosshatch sample, 46.6% and 53.7% for the cylindrical pore, and 36.6% and 43.0% for the BCC architecture. Figure 5.10B shows the fatigue data in terms of median life stress amplitude and indicates that all architectures had a detrimental impact on fatigue from a stress-based standpoint. Comparing the data to solid controls via linear regression returns a significant ( $p < 0.0001$ ), negative dummy variable coefficient on x-axis intercept for all (-1.50, -1.49, and -1.79 for EPU-37, EPU-CP, and EPU-BCC, respectively) and a significant, positive dummy variable coefficient on slope for only EPU-37 (2.72,  $p = 0.0111$ ). This indicates that the fatigue performance of all architectures is shifted to lower cycles as compared to solid samples, and additionally that the crosshatch samples show significantly increased slope within the analyzed range. Runouts at 1 million cycles were successful at median life stress amplitudes of 0.37 MPa and 0.41 MPa for the crosshatch sample, 0.33 MPa and 0.48 MPa for the cylindrical pore, and 0.29 MPa and 0.37 MPa for the BCC architecture. Figure 5.10C shows the stress-life fatigue data with the porous samples now adjusted by their solid fraction percentages. The plot indicates a recovery of the fatigue data to that of the solid printed control, and indeed regression analysis on the adjusted stress data indicates no significant difference in x-axis intercept between the solid samples and crosshatch,

cylindrical pore, or BCC samples. However, the adjustment does not affect any differences in slope.

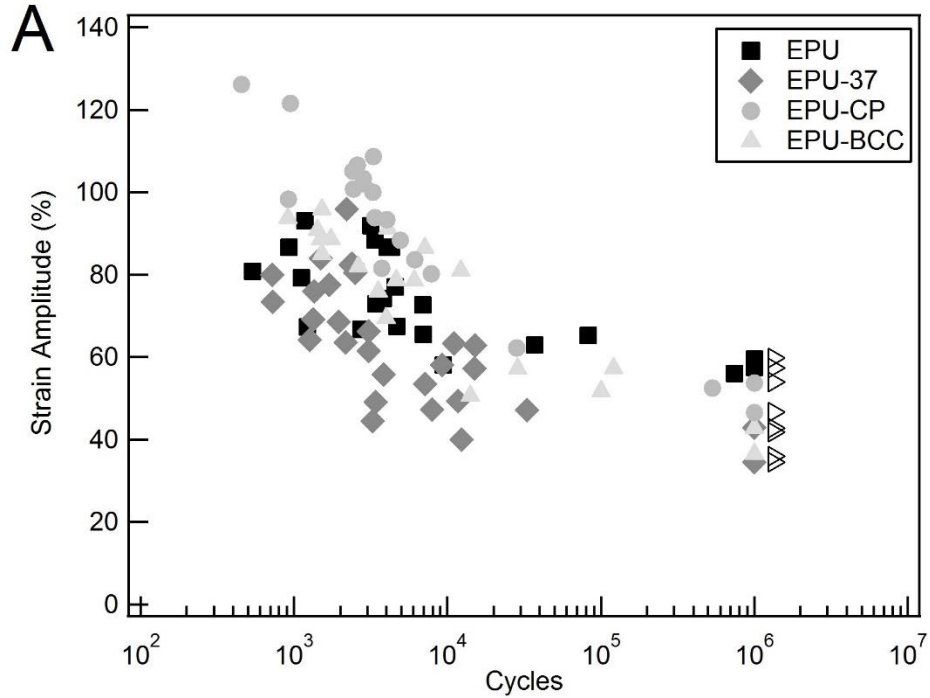


Figure 5.10: Fatigue data for solid, crosshatch, cylindrical pore, and BCC spherical pore EPU40 samples in terms of strain amplitude (A) and median life stress amplitude (B). C shows median life stress amplitude fatigue data after adjusting for sample solid fraction percentages. Stress-based data (B) shows significantly reduced x-axis intercepts for all architectures ( $p < 0.0001$ ) and significantly increased slope for EPU-37 samples ( $p = 0.0111$ ) when compared to solid samples. When adjusted by solid fraction (C), stress-based data shows no significant difference in slope or intercept for EPU-CP and EPU-BCC samples versus solid samples, however EPU-37 samples still demonstrate significantly increased slope.

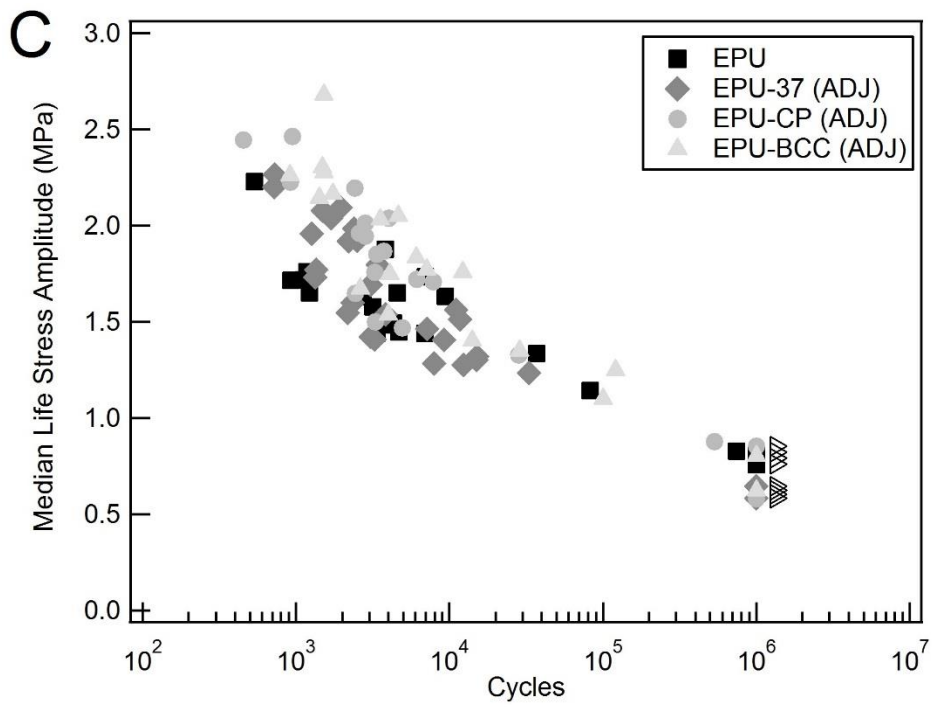
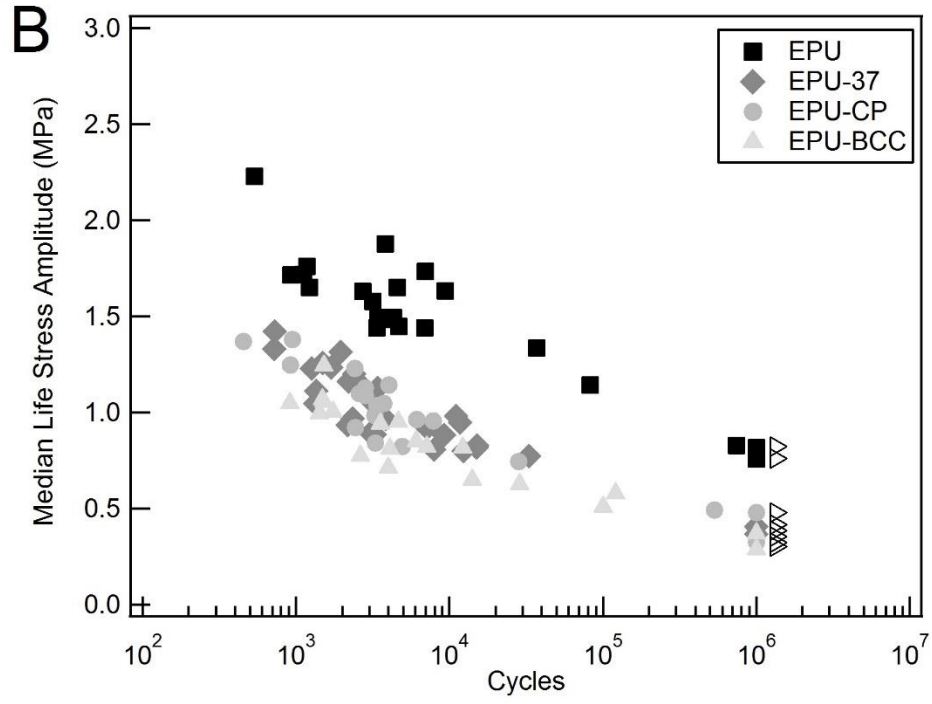


Figure 5.10: Continued

Strain-based fatigue data for EPU40 crosshatch, cylindrical pore, and BCC spherical pore specimens with architecture printed only within the gage section are shown in Figure 5.11. All three architectures show a trend of seemingly increased strain-based fatigue performance when the architecture is localized to the gage section instead of globally distributed throughout the sample gage, taper, and grip sections. In addition, removal of the perimeter from the local architecture samples seems to lead to a further increase in strain-based fatigue performance.

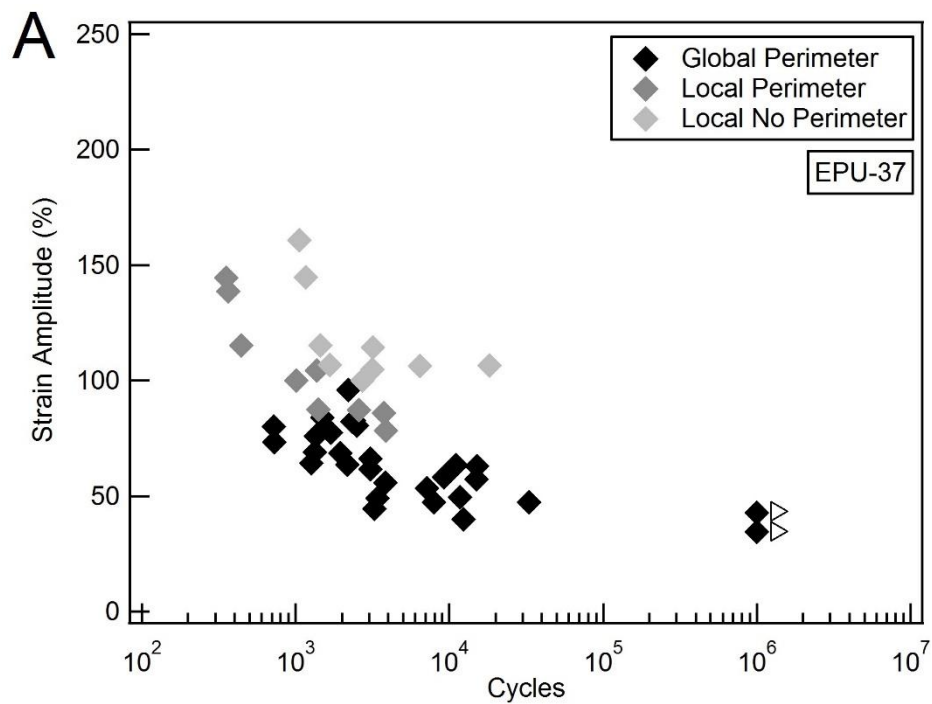


Figure 5.11: Strain amplitude fatigue data for crosshatch (A), cylindrical pore (B), and BCC spherical pore (C) EPU40 samples with global architecture and a perimeter as compared to samples with architecture localized to the gage, with and without a perimeter.

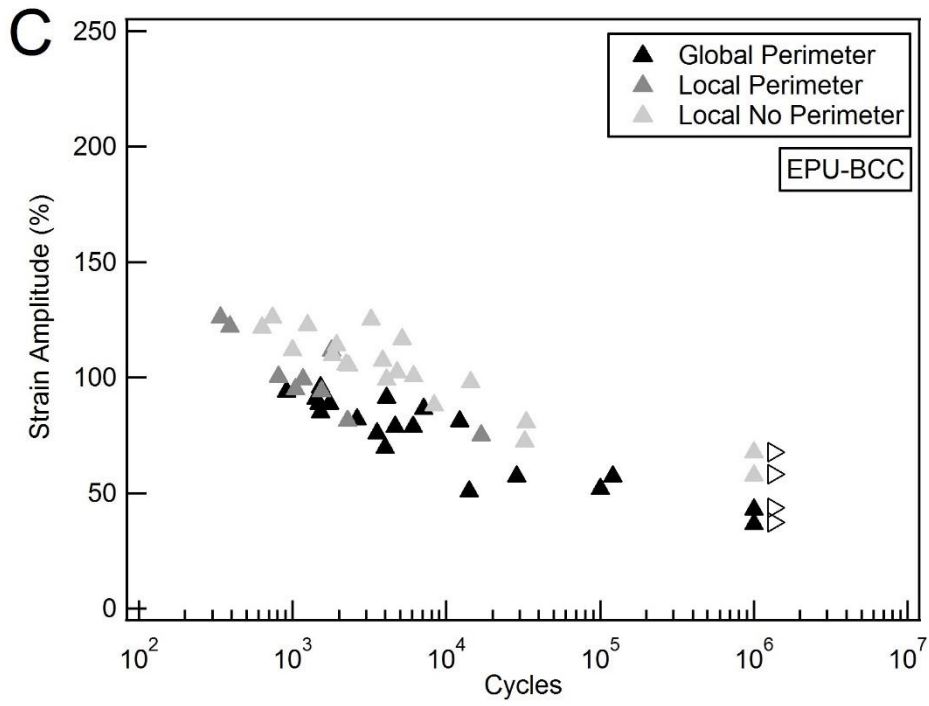
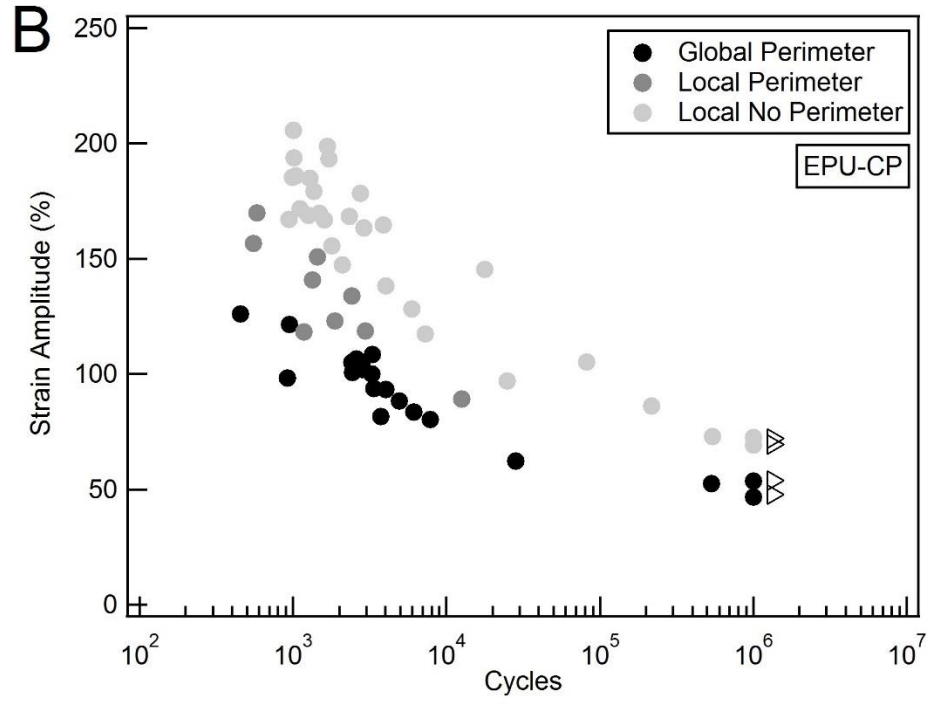


Figure 5.11: Continued

## 5.4 Discussion

Polyurethanes are a popular class of biomaterials that have already found widespread use in a number of biomedical applications. Their popularity will likely continue to increase as the biomedical field pushes for the use of tough, compliant materials to address issues associated with many traditional, stiffer materials. For example, the benefits of a compliant material are becoming apparent in applications ranging from spinal devices [115] to acetabular cups [106, 109] to meshes for hernia repair [248, 249]. Not only are PUs compliant, tough, and biocompatible, but they are also candidates for 3D printing through processes such as fused deposition modeling for thermoplastic varieties or even through photo-curing methods. 3D printing capabilities provide obvious benefits such as custom implant design and/or inclusion of complex architectures or geometries that are not otherwise possible with conventional processing methods. However, prior to these benefits becoming reality, the effect of 3D printing and printed architectures on the resulting material properties must first be understood. In our previous work (Chapter 4), we demonstrated the potential for printing solid PCU samples that perform on par with traditional injection molded controls in terms of strength and fatigue performance. While the properties of solid printed samples were on par with injection molded samples, many biomedical applications may benefit from, or simply require the use of architectures or pores. The work in the present study represents the beginnings of an effort to characterize the effects of printed architectures and pores on the resultant mechanical properties, including fatigue, of compliant PUs. The results obtained allow us to make several observations.



Our first observation is that the tested elastomeric polyurethanes are relatively tolerant of notches and complex architectures; however, the results differed slightly between the tested materials and also seemingly depended on pore shape. For FDM PCU, simple crosshatch architectures have a significant impact on tensile failure stress and stress-based tensile fatigue performance as compared to solid controls, however, they do not have a large impact on tensile failure strain or strain-based tensile fatigue performance. This observation is supported by data shown in Figures 5.4 and 5.8. For 95A, the use of a crosshatch architecture with even a relatively small porosity of 18% results in a decrease in tensile strength by roughly 50% from the solid printed control. Greater line spacings, and thus greater porosity, exacerbate the effect albeit to a diminishing degree. Figure 5.8C indicates that the effect on stress-based fatigue performance is not simply proportional to the sample's porosity, as adjusting the data by the solid fraction percent does not provide a full recovery of the stress-life fatigue data to that of the solid control. This suggests that the introduction of a crosshatch architecture likely also causes significant stress concentrations or significantly changes the loading states observed. The significant change in slope of the stress-life fatigue data (Figure 5.8B) indicates that this effect has a larger impact in higher cycle regimes. Comparing the adjusted data for both 95A crosshatch varieties (Figure 5.8C) suggests the effect is independent of the exact porosity of the resulting crosshatch scaffold. While crosshatch 95A samples did exhibit significantly lower failure strain in tension than the solid printed control, as well as apparently diminished strain-based fatigue performance, it is not believed these results are completely attributed to the architecture. In our previous work, we compared 3D printed solid (FDM) and injection molded (IM) PCUs in monotonic tension and fatigue, finding that FDM

samples exhibited larger failure strains and improved strain-based fatigue performance. It was concluded the effect was due to smaller and less organized hard domains in FDM samples (Chapter 4). This conclusion is supported by the findings of Pompe et al., who found that the hard segment morphology of thermoplastic polyurethanes is highly dependent on processing temperature rather than processing method, with higher processing temperatures leading to smaller hard domains and greater tensile failure strain [230]. As mentioned in Section 5.2.2, the solid 95A samples were printed with a nozzle temperature of 225°C, while the crosshatch samples were printed at 205°C. The higher nozzle temperature for solid samples was necessary as it lowered the viscosity of the extruded material, allowing for minimization of voids. Whereas for crosshatch samples, the lower nozzle temperature and viscosity were necessary to ensure well-formed, round extrusions that bridged between the lines of the previous layer without slumping. Therefore, it is likely that much of the difference in failure strain, and strain-based fatigue performance, is due to differences in processing temperatures and not due solely to the presence of the crosshatch architecture. This assertion is supported by the IM monotonic and fatigue data (Figures 5.4A & 5.8A), which was processed at an intermediate temperature of 215°C. As can be seen, the IM monotonic failure strain and strain-based fatigue data matches much closer with the crosshatch samples, in fact the failure strain of IM samples was not significantly different from any group of crosshatch samples. However regression analysis of stress-based fatigue data indicates that that both sets of adjusted crosshatch data still show a significantly lower x-axis intercept and higher slope as compared to IM samples ( $p < 0.0001$  for all).

Similar to the PCU crosshatch samples, the EPU crosshatch samples also saw a significant reduction in tensile strength while maintaining the tensile failure strain of the solid control. Figure 5.5 indicates that the EPU40 crosshatch samples maintained a higher percentage of the solid sample failure stress than PCU samples, perhaps due to the material's softer nature. The EPU crosshatch samples demonstrated a notable decrease in strain-based fatigue performance (Figure 5.10A), particularly in the higher cycle regime. Careful examination of Figures 5.9A and 5.10A suggests that this change in fatigue performance is similar to that seen for the diamond notch samples. It is likely that this similarity is due to the use of square lines, combined with the continuous nature of the printing process, which makes the crosshatch EPU samples essentially an array of diamond notches. Much like PCU, the EPU crosshatch samples also demonstrated a significant effect on fatigue from a stress-based standpoint. When adjusted by the solid fraction percent, the EPU fatigue data demonstrated a much more significant recovery towards the solid sample control as compared to PCU. However, the EPU crosshatch sample stress-based fatigue data still exhibited a significantly increased slope which may indicate a residual stress concentration. Figure 5.7A demonstrates the change in geometry of an EPU crosshatch specimen at approximately 50% strain and from this figure it is clear that the vertices between lines restrain their reorientation as expected, leading to a wave-like formation that is likely a source of significant stress concentrations.

Moving on to the notched specimens of EPU40, monotonic results demonstrated no significant difference in failure stress or strain for both the circular and diamond notches as compared to the solid control. The apparent increase in overall stiffness from solid samples seen in Figure 5.4C is likely the result of an increased strain rate due to the

presence of a notch causing strain localization. Comparing the strain-based fatigue data (Figure 5.9A) suggests that pore geometry, and hence notch severity, did impact fatigue performance. However, regression analysis on stress-based fatigue data (Figure 5.9B) indicated no significant difference in either slope or x-axis intercept of stress-based fatigue data for either tested notch as compared to the solid control. While in general agreement, these results are not as definitive as those of McNamara et al., who found a notable decrease in fatigue lifetime with the addition of edge notches in samples of natural rubber and EPDM [193]. Although, comparisons are difficult to make due to differences in materials, sample geometry, notch location, and notch severity. Based on data by McNamara, it seems likely that the fatigue performance of EPU40 would suffer more if notch severity was increased further. However, the comparison would be interesting as materials with high hysteresis, such as polyurethanes, have been shown to significantly outperform materials with less hysteresis, such as natural rubber, in terms of resisting crack propagation [196, 197]. Nevertheless, while notch severity did seem to have a noticeable effect on fatigue performance, the effects were rather small.

Finally, examining the performance of the cylindrical pore and BCC spherical pore EPU40 specimens draws some interesting parallels with the notched and crosshatch sample data. Figure 5.10A suggests that neither architecture had a large impact on the strain-based fatigue performance, similar to the circular notch samples, and in contrast to the crosshatch as well as diamond notched samples. While Figure 5.10B clearly shows a significant decrease in stress-based fatigue performance, that difference is fully recovered when adjusted by sample porosity. This is again in contrast to the crosshatch samples, which still demonstrates a significantly increased slope for stress-based fatigue performance after

porosity adjustment. These results confirm the detrimental effect of notch severity and illustrate the relative tolerance of this material to architectures.

To summarize the points of our first observation, both tested materials were relatively tolerant of the tested architectures. Introduction of porosity led to a decrease in tensile failure stress as expected, without a significant effect on tensile failure strain. Both materials saw relatively small effects on fatigue performance after introduction of architecture, however it is clear through the comparison of the adjusted crosshatch fatigue data that the EPU40 material was more tolerant than the 95A PCU. It is not immediately clear if this result is completely attributable to the difference in material stiffness or whether other factors of the material structure are involved, as the EPU40 material is significantly softer than the 95A PCU. Future studies utilizing a softer thermoplastic PCU which matches the stiffness of EPU40 would be interesting, however printing with such a soft filament via FDM would be exceedingly difficult. Our data also shows that pore geometry, and hence notch severity, does impact the fatigue performance of elastomeric PUs. This effect becomes most apparent in higher cycle regimes as evidenced by the increased slope of the resulting fatigue data and the lower amplitudes of the 1 million cycle runouts. Finally, due to the similarities in fatigue performance between the different EPU40 samples, it seems that the fatigue performance may be somewhat predictable if the porosity and pore shape are known. Whether the same can be said for the thermoplastic PCU is not immediately clear, as the printing process is not yet well suited for the creation of complex architectures. However, the agreement in fatigue data between the two varieties of 95A crosshatch samples tested (Figures 5.8A & 5.8C) suggests so.

The predictability of the EPU40 fatigue performance comes with an important caveat and leads to our second observation, which is that the fatigue performance of elastomeric PU samples is highly affected by the placement of architecture. This effect is demonstrated in Figure 5.11 which shows the strain-based fatigue data of EPU40 crosshatch, cylindrical pore, and BCC spherical pore samples when the architecture is printed globally versus locally, with and without a perimeter. While full fatigue curves were not developed for each iteration, it seems apparent across all three architectures that the fatigue performance rather drastically improves when the architecture is localized to the gage section of the sample. Furthermore, when the perimeter is removed, the samples again see an apparent boost to fatigue performance. Each of these changes would lead to an effective softening of the gage section relative to the taper and grip sections of the sample and hence a localization of strain to the gage section. The effect also seems more pronounced in the lower cycle or higher strain amplitude regions. Monotonic results (Figure 5.6) provide little insight towards the discrepancy in fatigue performance. While the crosshatch and BCC architectures appear softer as expected when printed without a perimeter, the cylindrical pore samples remain largely unchanged likely due to the minimal additional volume a perimeter adds for this architecture. Localizing the architecture to the gage section as well as having a perimeter both serve to restrain the gage section from transverse strain, thereby reducing the effective Poisson's ratio of the sample, and indeed the single samples imaged for this purpose support this (Section 5.3.2). Such an effect could lead to substantial changes in the loading states and stresses observed in the gage section; however, the two differences in sample design have contradictory effects on fatigue performance. Nevertheless, while the cause of this effect on fatigue performance is not

perfectly clear, the results suggest the effect is geometrical or structural in nature and demonstrates the importance of designing samples to be consistent when studying the relative performance of samples with architecture.

Our last observation is that the EPU40 material performs very similarly in fatigue to the thermoplastic PCUs tested in both this study as well as our previous study (Chapter 4). This observation is demonstrated in Figure 5.12, which shows the fatigue results of the EPU40 material together with data from solid printed samples of 75A, 85A, and 95A grades of PCU. Strain-based data (Figure 5.12A) appears slightly flatter, indicating that larger strain amplitudes are perhaps more detrimental to EPU40, however the million cycle runout amplitudes are among the highest of the tested PCU grades. Stress-based data (Figure 5.12B) clearly shows the EPU40 material is the lowest performing for stress-based fatigue. However, the EPU40 material has a listed Shore hardness of 68A, whereas the PCUs are denoted by their Shore hardness, which are: 75A, 85A, and 95A. Based on the trends in the stress-based data based on hardness, the EPU40 material fits approximately where a PCU of 68A hardness would be expected. This result is somewhat surprising considering the presumably different chemical structure to accommodate chemical crosslinking in EPU40 and the vastly different printing methods between the two materials, but illustrates the versatile nature of polyurethanes. Combined with the significantly enhanced printing capabilities for this material, and general tolerance for notches and architectures, the results are promising overall for the material's potential in biomedical applications.

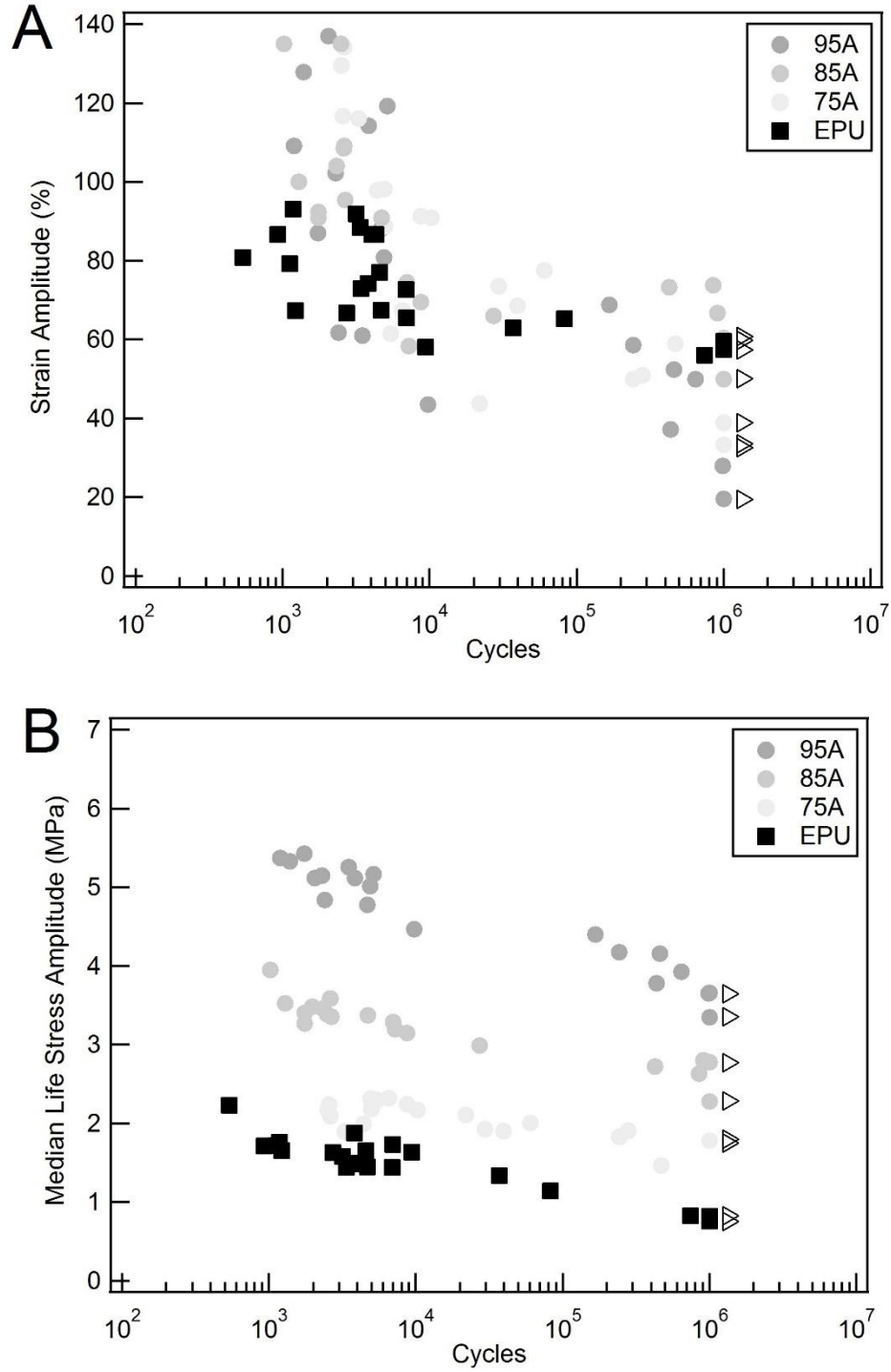


Figure 5.12: Fatigue data for three grades of solid printed PCU and solid EPU40 in terms of strain amplitude (A) and median life stress amplitude (B). All PCU fatigue data obtained from a previous study (Chapter 4).



## 5.5 Conclusions

We have investigated the tensile fatigue performance of samples of a printed thermoplastic PCU as well as a photo-cured PU with various architectures. The following are the conclusions of the work:

1. Elastomeric PUs are relatively tolerant of architectures and notches. Introduction of porosity led to a decrease in tensile failure stress based on gross area as expected, without a significant effect on tensile failure strain. Effects on fatigue performance were small, and the EPU40 material proved more tolerant than the tested thermoplastic PCU. Comparison of square shaped notches and pores to circular indicates that notch severity impacts fatigue performance and the effect is largest in the high cycle regime.
2. Fatigue data of polyurethanes with architecture is strongly impacted by localizing the architecture to the gage section as well as the use of a perimeter. The cause of the effect is likely geometrical or structural in nature, therefore caution is warranted when designing and comparing performances of samples with architecture.
3. The elastomeric, photo-cured polyurethane EPU40 performs similarly in tensile fatigue to thermoplastic PCUs despite the presence of chemical crosslinks and vastly different printing methods.

Limitations of this study include the consideration of only one type of crosshatch orientation, and an overall limited number of included architectures and notches. There are many untested variables that may affect the fatigue performance of crosshatch scaffolds such as: line width, layering scheme, and loading axis. In addition, there are countless numbers of scaffold designs that may be desired for use in biomedical applications.

However, this study still provides insight into the effects of some basic architectures on fatigue performance, which has not yet been shown in literature. In addition, based on the negligible effect of crosshatch scaffold line spacing beyond loss of material volume for PCU samples, as well as the parallels in fatigue performance between different EPU40 sample types, the effects detailed in this study may apply more broadly to other scaffold designs for elastomeric materials however further studies are required to verify this. Feature resolution of printed samples is perhaps another limitation, as printed features may have been larger than desired for some biomedical applications due to current limitations in printer capabilities. However, small changes in size scale would not be expected to significantly impact results for the tested architectures. Finally, the use of a buffered saline bath, instead of a more biologically active and relevant solution, represents another limitation. While EPU40 remains to be proven as a biomaterial, PCU has shown to be extremely resistant to biodegradation. However, the increase in surface area to volume ratio from the introduction of architecture may exacerbate degradative effects and warrants consideration.

## **CHAPTER 6**

### **FOLLOW-UP STUDIES**

#### **6.1 Introduction**

This section presents a series of three follow-up studies to address questions arising from previous studies. The first study presented addresses the differences in strain behavior of FDM and IM samples of PCU found in Chapter 4. It was hypothesized that the differences in strain behavior was due to smaller and less organized hard domains brought on by differences in processing temperature, cooling rate, or simply sample age. Therefore, this study involved testing FDM samples that have been: printed at IM temperatures, aged, or annealed. The second study presented addresses a limitation of the study presented in Chapter 4, which is the use of a laser cutter to form the IM samples. Since it was necessary to develop a custom fatigue sample geometry, fatigue samples had to be laser cut from IM sheet stock. However, this raised the question of whether such cutting had an impact of the resulting sample fatigue performance as the FDM samples were directly printed and not laser cut. To address this, a follow-up study is presented here in which sheet stock is printed and then cut into fatigue samples utilizing a laser cutter. Initially, this method of forming FDM fatigue samples was considered to eliminate the laser cutting variable upfront. However, we ultimately decided to directly print the fatigue sample geometry in order to include any surface roughness attributed to the FDM process, which laser cutting would remove. In addition, the ability to directly print final parts is a major benefit of 3D printing. Finally, the third study presented probes the effect of oxidation on PCU fatigue performance. The oxidative and hydrolytic stability of PCU has been somewhat

extensively studied, even accounting for effects of dynamic load (See Section 1.1). However, no studies could be found assessing the fatigue performance of PCU following oxidation. This is accomplished by comparing the fatigue performance of IM samples of PCU before and after oxidation by an established, accelerated oxidation protocol for PCU.

## **6.2 Materials and Methods**

### 6.2.1 Processing temperature, aging, and annealing study

Four different methods are employed in an attempt to match IM monotonic tension performance with FDM samples. For the first method, FDM monotonic samples were printed, allowed to rest seven days at room temperature, placed in an oven for 24 hours to anneal at 110°C, and finally allowed another seven day rest at room temperature (n = 3 for each grade). For the second method, FDM monotonic samples were printed and allowed to sit at room temperature to age for approximately 3 months (n = 3 for each grade). For the third method, FDM monotonic samples were printed, allowed to rest seven days at room temperature, placed in an oven for 24 hours to anneal at 150°C, and finally allowed another seven day rest at room temperature (n = 3, 85A grade only). Finally, for the fourth method, FDM monotonic samples were printed at a nozzle temperature matching the maximum temperature utilized during injection molding (see Section 4.2.1) and then allowed to rest for seven days. This corresponds to a nozzle temperature of 200°C for the 85A grade of PCU (n = 3, 85A grade only). All tested groups are summarized in Table 6.1. All samples were printed utilizing the same printing parameters previously used (see Section 4.2.2), with the obvious exception of the annealing, longer aging, or decreased nozzle temperature. Samples were tested in monotonic tension utilizing the same procedure previously used

(see Section 4.2.4). Monotonic tension curves for IM and control FDM specimens are taken from our previous study (Figure 4.13).

Table 6.1: Summary of tested groups for aging and annealing study.

Method	Denoted	Process	Grades†
1	ANL110	PRINT → REST (7 DAYS) → ANNEAL (110°C 24 HRS) → REST (7 DAYS)	75A 85A 95A
2	AGED	PRINT → AGE (3 MONTHS)	75A 85A 95A
3	ANL150	PRINT → REST (7 DAYS) → ANNEAL (150°C 24 HRS) → REST (7 DAYS)	85A
4	200C	PRINT (200°C NOZZLE TEMP) → REST (7 DAYS)	85A
† n = 3 for each			

### 6.2.2 Laser cut FDM fatigue study

Assessing the effects of laser cutting on the fatigue performance of PCU first required the printing of sheet stock for laser cutting. Sheets of dimensions 6 mm x 15 mm x 71 mm were printed of the 85A grade of PCU utilizing the exact printing parameters previously used for directly printing fatigue samples (Section 4.2.2). The dogbone shape was then laser cut from the sheet stock utilizing the exact cutting parameters previously used for cutting IM fatigue samples (Section 4.2.6). Samples illustrating this process can be seen in the image shown in Figure 6.1. Following laser cutting, the samples were allowed to rest the requisite seven days (Section 4.2.3.5 & 4.3.1.5) prior to tensile fatigue

testing in the same manner as previously done (Section 4.2.6, n = 6). The original, directly printed FDM sample fatigue data is taken from our previous study (Figure 4.18).



Figure 6.1: Image showing printed sheet stock, laser cut sheet, and final sample.

### 6.2.3 Oxidation study

Fatigue samples for oxidation were laser cut from IM sheet stock in the exact same manner as done previously (Section 4.2.6). In order to assess the effects of oxidation on the fatigue performance of PCU, we utilized a well-established, accelerated oxidation protocol that has been found to result in damage comparable to one year *in vivo* for PCU [53, 56, 62, 63, 250, 251]. IM PCU samples were submerged in a 0.1 M  $\text{CoCl}_2$ , 20% by weight  $\text{H}_2\text{O}_2$  solution and kept in an incubator at  $37^\circ\text{C}$  for 24 days. Solution changes were carried out every 3 days. After 24 days, samples were thoroughly rinsed in distilled water

and then kept in PBS until fatigue testing. Fatigue tests were carried out in the same manner as done in our previous study in order to develop a fatigue life curve for oxidized samples (Section 4.2.6), and untreated sample fatigue data is also taken from our previous study (Figure 4.16). To assess the oxidative damage and compare to established literature, treated and untreated samples were scanned utilizing FTIR in the same manner as performed in our previous study (Section 4.2.3.4,  $n \geq 4$ ). The ratio (I) of the  $1256 \text{ cm}^{-1}$  peak, which corresponds to the C-O of the soft segment carbonate, to that of the  $1600 \text{ cm}^{-1}$  peak, which corresponds to a hard segment, aromatic ring carbon-carbon double bond, is utilized to assess soft segment damage [251].

#### 6.2.4 Statistical analysis

Comparisons between the tensile failure stress and strain of samples as well as FTIR data were performed with a Student's t-test. Comparisons between sample fatigue performances were performed via linear regression with a dummy variable, as described in Section 4.2.7, on the fatigue data based on median life stress amplitude.

### **6.3 Results**

#### 6.3.1 Processing temperature, aging, and annealing study

Figure 6.2 shows representative monotonic tension curves for the original tested IM and FDM samples from Chapter 4, as well as all new tested groups. Plots represent a median plot based on failure stress. While the 3 month aged samples for 75A and 85A did show a decrease in failure strain, they still do not match IM controls in terms of failure strain or slope of the strain-hardening portion of the plot. Samples annealed at  $110^\circ\text{C}$  demonstrate similar behavior as the control FDM samples, indicating that annealing at  $110^\circ\text{C}$  had little effect. Furthermore, the 85A samples annealed at  $150^\circ\text{C}$  also demonstrate

similar behavior as the control FDM samples. However, the 85A sample printed at a nozzle temperature matching the injection molded processing temperature not only showed decreased failure strain, but showed behavior that was remarkably similar to the original IM controls. In fact, the failure stress and strain were not significantly different between the two.

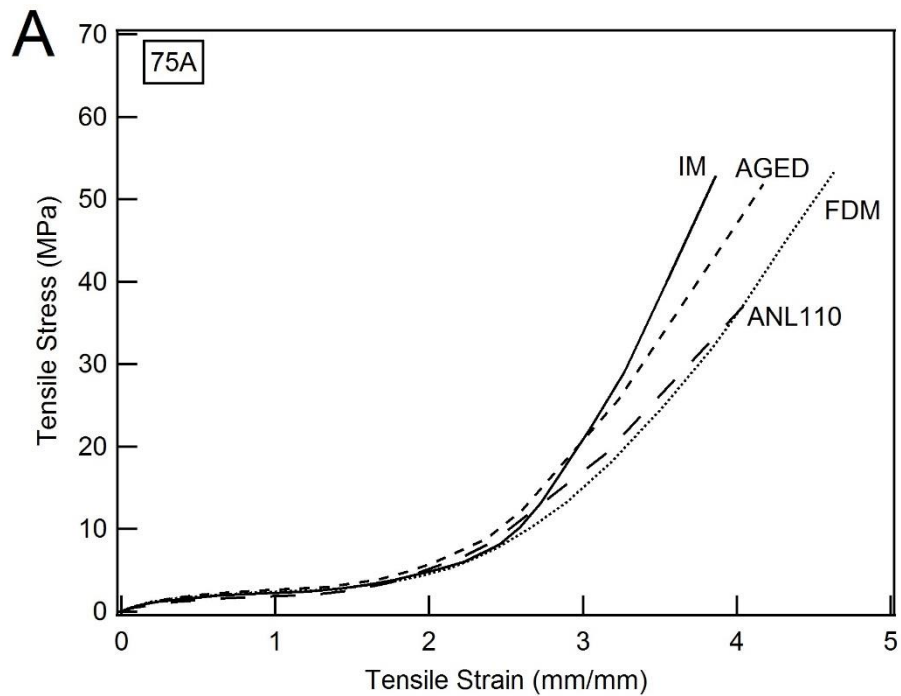


Figure 6.2: Monotonic tension curves of original IM and FDM samples, as well as the new groups for 75A (A), 85A (B), and 95A (C). FDM 200C 85A samples (B) showed no significant difference in failure stress or strain as compared to IM samples.



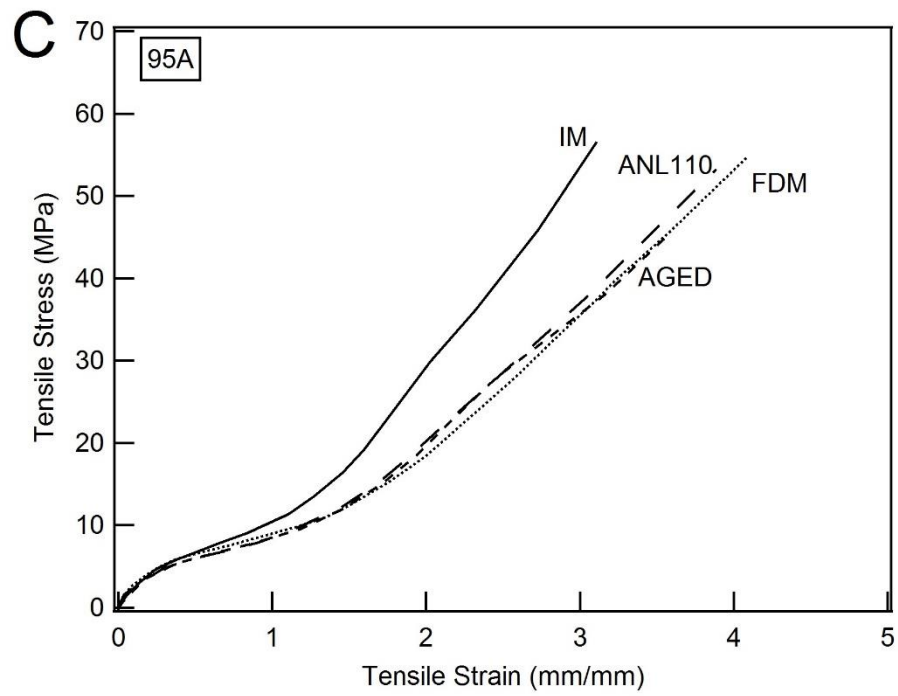
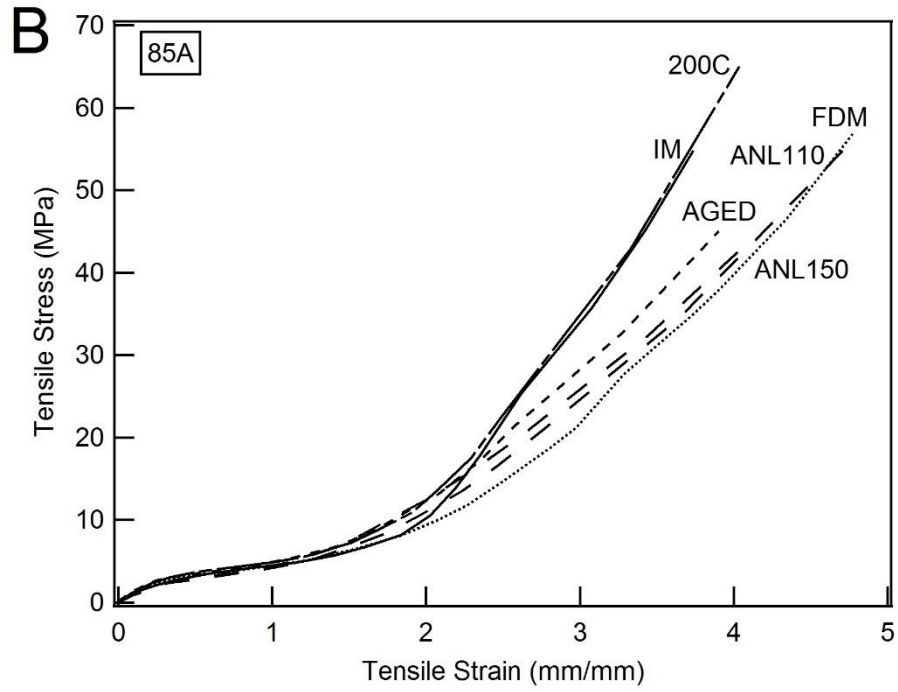


Figure 6.2: Continued

### 6.3.2 Laser cut FDM fatigue study

Fatigue data for the laser cut FDM samples (LC FDM), as well as the original IM and FDM fatigue data from Chapter 4, is presented in Figure 6.3. Strain-based fatigue data (Figure 6.3A) indicates that laser cut specimens of FDM sheet stock performed at least as well as the original, directly printed FDM specimens. Stress-based fatigue data shown in Figure 6.3B indicates that laser cut FDM samples performed on par with the original FDM specimens. Performing linear regression on the stress-based fatigue data (as in Section 4.3.4) indicates that there is no significant difference in either the slope or x-axis intercept of the laser cut FDM sample data as compared to the directly printed sample data.

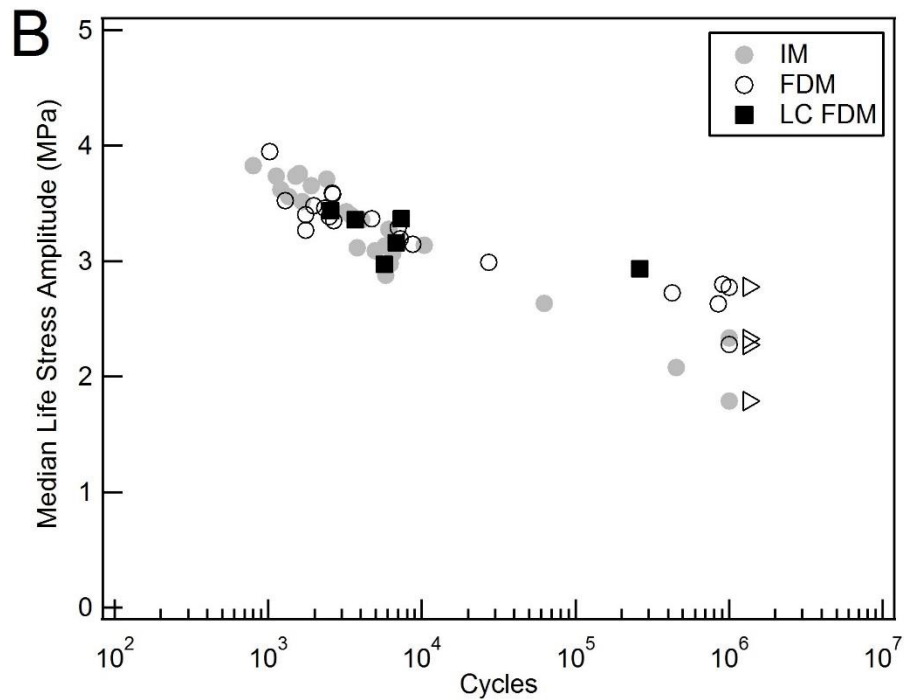
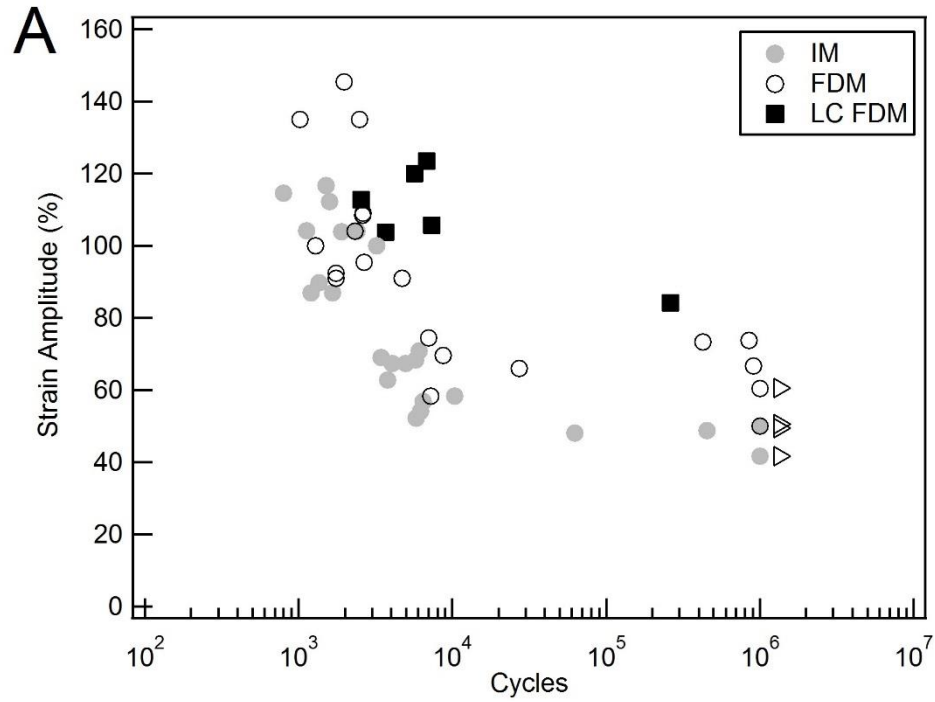


Figure 6.3: Fatigue data for original IM and FDM specimens together with new laser cut FDM samples in terms of strain amplitude (A) and median life stress amplitude (B). No significant difference was found in intercept or slope of LC FDM samples as compared to FDM.

### 6.3.3 Oxidation study

Representative FTIR plots for the oxidized IM samples versus control IM samples are shown in Figure 6.4. The plots show a clearly diminished peak at  $1256\text{ cm}^{-1}$  for the oxidized sample despite peaks at  $1600\text{ cm}^{-1}$  remaining the same. This indicates a loss of C-O bonds in the soft segment as expected. Comparison of the ratio of the  $1256\text{ cm}^{-1}$  peak to the  $1600\text{ cm}^{-1}$  peak for treated versus untreated samples indicates that the ratios are significantly different ( $p = 0.0135$ ). The reduction in this ratio for treated samples as compared to untreated is calculated as described by Dempsey et al., returning an average reduction of 14.3%. Dempsey et al. found reductions varying between 16% and 34%, however they used a 36 day oxidation protocol rather than the standard 24 day [251]. Therefore, we conclude that our oxidation protocol worked as expected.

Fatigue data for the oxidized, as well as the original IM fatigue data from Chapter 4, is presented in Figure 6.5. Strain-based fatigue data (Figure 6.5A) indicates that there may be a slight detriment in fatigue performance following oxidation. However, stress-based fatigue data shown in Figure 6.5B indicates that the oxidized samples performed on par with the untreated controls. Performing linear regression on the stress-based fatigue data (as in Section 4.3.4) indicates that there is no significant difference in either the slope or x-axis intercept of the oxidized sample data as compared to the untreated sample data.

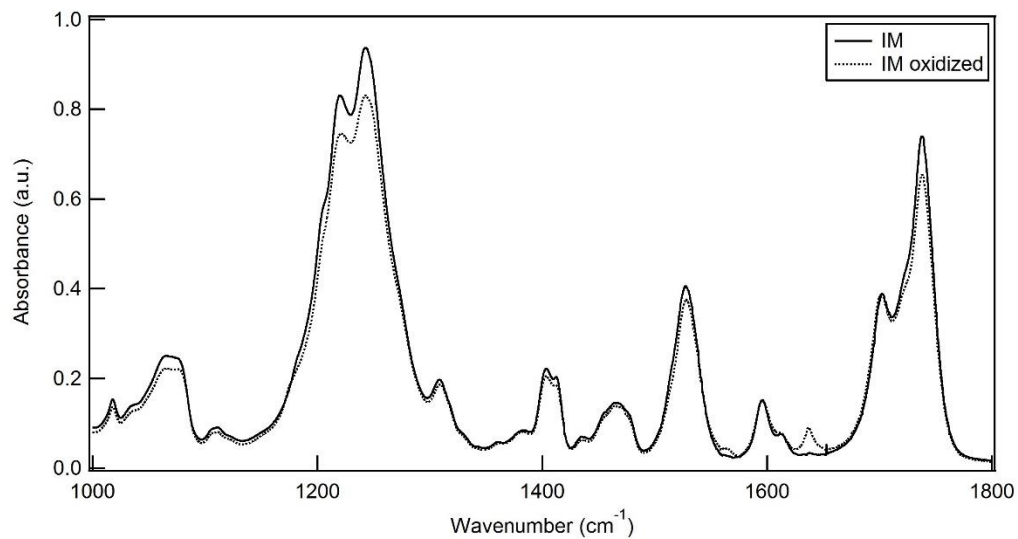


Figure 6.4: Representative FTIR plots of oxidized and control PCU samples. Oxidized samples demonstrate a significantly reduced ratio of the 1256 cm<sup>-1</sup> peak to the 1600 cm<sup>-1</sup> peak as compared to the control samples (p = 0.0135).

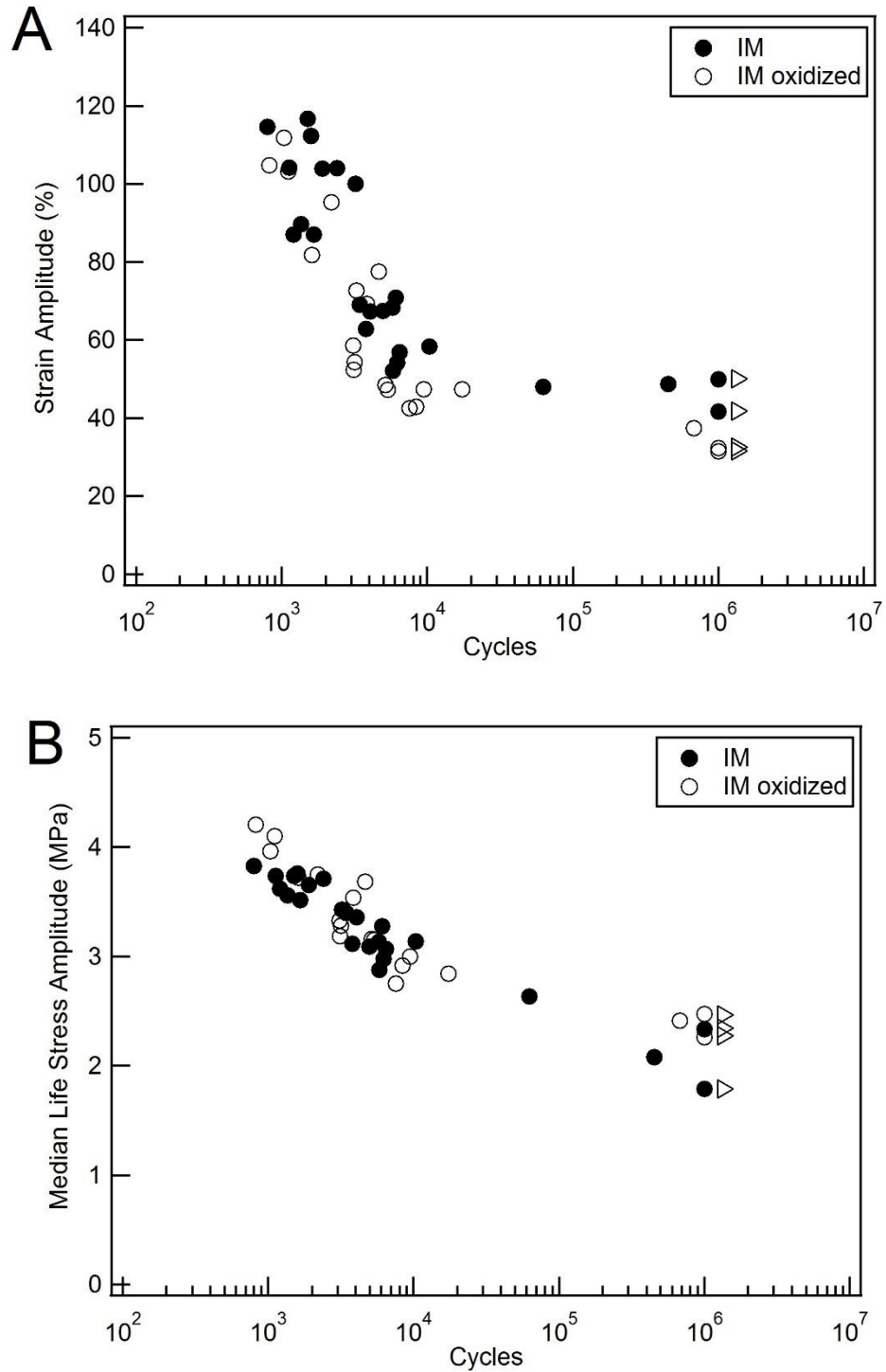


Figure 6.5: Fatigue data for oxidized and control samples in terms of strain amplitude (A) and median life stress amplitude (B). No significant difference between the control and oxidized samples was found in either intercept or slope of the stress-based data (B).

## 6.4 Discussion

### 6.4.1 Processing temperature, aging, and annealing study

The purpose of this study was to investigate the discrepancy in strain behavior between IM and FDM samples seen in Chapter 4. It was hypothesized that the difference in behavior was due to smaller and less organized hard domains which could be due to a number of factors such as processing temperature or simply sample age. From the results shown in Figure 6.2, it is clear that further aging of printed samples did not restore the behavior of FDM samples to IM controls, indicating that our seven day rest period implemented in Chapter 4 was adequate for phase separation at room temperature. While aged samples of 75A and 85A grades did appear to show smaller failure strains than FDM controls, the overall shape of the plots still matches closer with FDM controls than that of IM samples. This indicates that aging likely has its own unique effects on PCU morphology and behavior in tension. Results also indicate that annealing samples at either 110°C or 150°C does not have a noticeable effect on sample monotonic behavior. Annealed samples across all grades demonstrated essentially the same behavior as FDM control samples. Only by changing the printing nozzle temperature to match IM processing conditions were we able to match the monotonic tension behavior of IM samples. In fact, as shown in Figure 6.2B, the samples printed at the reduced nozzle temperature matched the behavior of IM samples remarkably well and showed no significant difference in failure strain or stress. This supports the findings of Pompe et al., who found that processing temperature, and not processing method, has a profound effect on TPU morphology and the resulting failure strain. Higher processing temperatures thermodynamically favor smaller “type I” crystallites of the hard domain over the larger “type II”. They also noted that relatively fast

cooling rates from higher processing temperatures also favored the formation of “type I” crystallites [230]. Therefore, it seems that by printing at a relatively high temperature (225°C), followed by rapid cooling of the 0.15 mm thick printed line, the TPU morphology favored “type I” crystallites in our original FDM samples. These smaller “type I” crystallites lead to increased tensile failure strain, and as was seen in Chapter 4, apparent improvements in strain crystallization and tensile fatigue performance. The effect of cooling rate brings into question whether the TPU morphology seen in FDM samples, and consequent benefit to fatigue performance, could be reproduced through injection molding instead. Certainly small samples, which may be easily quenched, could obtain such morphology. However, larger samples may be difficult to cool fast enough to retain the “type I” favored morphology. In addition, the effect of cooling rate also implies that TPU morphology can be altered in FDM samples simply by changing printing parameters such as layer thickness. Characterizing TPU morphology and resulting properties as a function of printing parameters (nozzle temperature, layer thickness, extrusion width, etc.) would certainly make for a valuable and interesting future study.

#### 6.4.2 Laser cut FDM fatigue study

The purpose of this study was to determine if laser cutting the IM samples in Chapter 4 had a significant impact on their fatigue performance. The laser power was purposely kept relatively low, instead using a large number of passes, in order to prevent significant damage to the IM material. However, the issue still warranted consideration, especially considering the remarkable comparison between FDM and IM sample fatigue presented in Chapter 4. Based on the fatigue data shown in Figure 6.3, we can conclude that laser cutting did not have a significant impact on PCU sample fatigue performance,



and that the conclusions of Chapter 4 remain valid. Linear regression indicates no significant difference in either slope or intercept of the stress-based fatigue data between the original FDM samples and the laser cut FDM samples. Strain-based fatigue data (Figure 6.3A) may even suggest that the laser cut FDM samples performed marginally better than the original FDM samples. This effect is likely due to the elimination of side surface roughness, as well as a reduction in the average presence of voids, from the use of laser cutting. During direct printing of fatigue dogbone samples, it was observed that the junction between perimeters and infills was perhaps the most problematic in terms of inclusion of voids. This effect was often exacerbated in the gage section and tapered sections. However, by printing an oversized, rectangular sheet this perimeter-infill junction was kept to the periphery, where it was later removed through laser cutting. Regardless, this effect is obviously not applicable with IM samples and the data presented confirms that laser cutting does not have a significant, detrimental impact on sample fatigue performance.

#### 6.4.3 Oxidation study

The purpose of this study was to investigate the effect of oxidation on the fatigue performance of PCU. As mentioned in Section 6.1, the hydrolytic and oxidative stability of PCU has been relatively well established. In fact, PCU was developed to address issues of hydrolytic and oxidative stability in previous generations of biomedical polyurethanes, specifically polyester urethanes and polyether urethanes [54]. While PCU has been found to outperform these previous generations in terms of biostability, the general consensus is that it is still somewhat susceptible to oxidation *in vivo* [53]. Studies have included examining the effects of dynamic loads [56] and even *in vivo* device studies [58], however the authors could not find any published work that investigates the effects of oxidation on

fatigue performance. Results from our study are shown in Figure 6.5, and are approximately representative of the fatigue performance of PCU following one year *in vivo*. While linear regression of the stress-based data (Figure 6.5B) indicates no significant difference in fatigue performance following oxidation, the strain-based data (Figure 6.5A) indicates that perhaps there was a relatively small effect. This effect is particularly noticeable for the higher cycle tests. Previous studies have shown that oxidation of PCU results in primarily only superficial surface damage such as pitting, and that tensile loading and unloading results in plastic deformation of the now crosslinked surface layer with a wave-like pattern emerging as the bulk material recovers and the surface buckles [53]. This effect could lead to minute surface cracks under cyclic tensile loading, and accelerated failure under fatigue, and is the likely source of any differences in fatigue performance observed. Such small effects may not be as apparent in stress-based data due to the use of the median life stress amplitude.

## **6.5 Conclusions**

The follow-up studies presented in this chapter sought to address several questions that arose during previous investigations. The following are the conclusions of these follow-up studies:

1. Aging and annealing, at temperatures up to 150°C, of our FDM PCU samples does not restore the morphology and subsequent strain behavior to that of IM samples. Changing the printer nozzle temperature to that of the IM processing conditions results in much more consistent behavior between FDM and IM samples. This confirms that processing temperature is a larger determinant of resulting TPU morphology than processing method, and illustrates the importance of

understanding the thermal history of TPU samples. The thermal history and resulting morphology may change as a function of FDM parameters.

2. Laser cutting of our PCU samples did not significantly impact their tensile fatigue performance. However, this may be dependent on sample size, geometry, and cutting parameters, therefore caution is still warranted.
3. One year of simulated *in vivo* oxidation of PCU did not have a large impact on tensile fatigue performance.

One potential limitation is considering only one year of simulated time when probing the effects of oxidation on fatigue performance of PCU. Results suggested that there may have been a small effect of oxidation on fatigue performance, and it is not clear whether, or to what extent, this effect would be exacerbated by further oxidation. Regardless, the study still provides valuable insight into the fatigue performance of PCU under simulated *in vivo* oxidation.

## CHAPTER 7

### CONCLUSIONS AND FUTURE WORK

The purpose of this work was to develop relationships between soft polymer structure and processing with the resulting mechanical properties, particularly fatigue performance. The ultimate goal was to provide insights useful for the application of soft polymers in load-bearing, biomedical applications such as in orthopedics. As such, a large portion of the work herein pertains to polyurethanes, particularly polycarbonate urethane, as it is rapidly gaining popularity in a number of biomedical applications. Biocompatible, soft polymers have many potential applications as solutions to issues with stiffer implant materials are sought. However, soft materials are often plagued with durability issues as was seen in many applications of silicone. Therefore, we sought to develop processing-structure-property relationships that would provide a better understanding of soft material performance and hopefully lead to more successful soft devices in the future.

In the first aim, we sought to develop relationships between polymer structure and compressive fatigue performance and cyclic loading properties for an array of soft polymers including: silicone, PCU, and acrylates. We compared these materials to native meniscal tissue and utilized thermo-mechanical transition data to help interpret the results. What we found was that materials devoid of sufficient energy dissipation mechanisms at the testing temperature, as evidenced by tan delta or loss modulus data, typically exhibited fatigue fracture under our cyclic compression protocol. This included silicone as well as one acrylate that was specifically tailored to have low energy dissipation. In contrast, materials with sufficient energy dissipation mechanisms at the testing temperature, such as

PCU, resisted fatigue fracture during cyclic compression. Instead, these materials demonstrated a ratcheting type behavior whereby they exhibited a continued increase in mean compressive strain without fracture under cyclic compressive loading. These materials behaved very similarly to native meniscal tissue which also demonstrated ratcheting type behavior without fatigue fracture. Results indicated minimal permanent damage to these energy dissipating, or toughened, materials under our cyclic compression protocol, which is in contrast to the obvious fatigue fracture of materials such as silicone. While the toughened polymers behaved similarly under cyclic compression, the mechanisms behind their energy dissipation likely differed. For PCU, the dissipation is attributed to hydrogen bonding between hard and soft segments. For the acrylates, dissipation is attributed to the proximity to their glass transition and the relative motions of chains. For the meniscal tissue, dissipation is attributed to the flow of water through the charged extracellular matrix. Overall, these results illustrate the benefits of having energy dissipation mechanisms for compressive fatigue performance.

In our second aim, we focused exclusively on PCU due to its popularity and relative success in our first aim. There are a large number of factors that can ultimately affect the structure and morphology, and therefore resulting properties and fatigue performance, of thermoplastic polyurethanes such as PCU. For this aim, we sought to better understand the effects of perhaps one of the most basic factors: hard segment content. In addition, we also sought to address the effects of 3D printing due to the potential benefits such processing could provide. To achieve these goals we tested three grades of PCU in cyclic tension, in both injection molded and 3D printed (FDM) varieties. Results indicated that increased PCU hard segment content led to increases in monotonic stiffness and shear failure stress,

as well as improvements in tensile fatigue from a stress-based standpoint despite insignificant effects on monotonic tensile strength. Effects on tensile failure strain and strain-based fatigue performance were more complex and seemingly influenced by interaction between phases. 3D printed samples matched or exceeded IM controls across the board in terms of monotonic tension, compression, shear, and tensile fatigue. The success of printed PCU samples was attributed to favorable printing parameters, resulting in samples more than 99% solid, as well as the toughness of PCU which results in lower flaw sensitivity. Results also indicated a discrepancy in strain behavior of printed and IM samples which was verified to be due to processing temperature differences. Overall, the results of this aim demonstrated the differences in PCU properties due to hard segment content, illustrated the remarkable potential for 3D printing of PCU, and also illustrated the importance of understanding how such processing can affect material morphology.

Based on the success of solid printed PCU samples in our second aim, we decided to focus on another major benefit of 3D printing for our third aim, which is the ability to create complex architectures and geometries. Many biomedical applications of polymers would benefit from the inclusion of pores or architectures, however very little published work exists documenting the effects of such architectures on fatigue performance for polymers. Therefore in this aim we sought to characterize the effects of various relevant architectures on the fatigue performance of polyurethanes. We tested simple crosshatch scaffolds of both PCU as well as a photo-cured, chemically crosslinked, elastomeric polyurethane (EPU40). In addition, we tested two notch geometries and two advanced architectures, including cylindrical pore and BCC spherical pore type architectures, for the EPU40 material. Results for PCU indicated a significant decrease in monotonic tensile

failure stress and stress-based fatigue performance for crosshatch scaffolds that was not fully attributed to loss of material volume. Effects on tensile failure strain and strain-based fatigue performance were not as substantial. For the EPU40 material, crosshatch scaffolds saw a similar decrease in tensile failure stress without a significant impact on tensile failure strain. Fatigue results indicated a small effect on strain and stress-based fatigue data for the crosshatch architecture, however stress-based data was more readily recovered to solid samples controls when adjusted by porosity as compared to the 95A PCU. Advanced architecture samples of EPU40 did not demonstrate a significant impact to fatigue performance, likely due to the spherical pore shape. The impact of the diamond notch and crosshatch architecture on EPU40 sample fatigue performance versus that of the circular notch, cylindrical pore, and BCC spherical pore architectures suggests that notch severity does impact fatigue performance for soft polyurethanes. During this study, it was also discovered that the PU fatigue results were greatly impacted by localization of strain to the gage section, which illustrates the importance of careful sample design when comparing the performance of different architectures. Finally, results indicated fairly similar fatigue performance between the solid specimens of PCU and EPU40 which is rather surprising given the presumably altered polymer structure to accommodate chemical crosslinks in EPU40 and the vastly different method of printing. Overall, the results of this aim demonstrated the effects of including architectures in soft polyurethanes which may be valuable in many biomedical applications. While some architectures did affect fatigue performance beyond loss of material volume, the effects seem small relative to many stiffer materials, which illustrates the versatility of soft polyurethanes for such applications.

While the results presented provide valuable insights for the biomedical field, a great number of further studies are warranted or may be of interest. For instance, based on the results of Aim 1, while relative energy dissipation capabilities of materials can be used to understand general trends and behaviors of materials under cyclic compressive loads, it is clear this factor alone is not sufficient for *a priori* prediction of fatigue performance. Further studies to include other factors and improve on this understanding in soft materials would be extremely valuable. For example, systematic studies addressing variables such as crosslinking density, crosslink type, or polymer structure could likely help complete the picture and may be a good starting point. Another limitation of Aim 1 was the harvesting and isolation of cylindrical meniscal samples from the surrounding tissue. While necessary for direct materials comparison, it likely had a substantial effect on cyclic ratcheting behavior due to the loss of surrounding tissue to provide support and negative pressure which would assist with fluid inflow during unloading. Further studies on the ratcheting behavior of intact menisci under cyclic loading of similar amplitudes, as well as geometrically similar synthetic materials, would make for an interesting comparison to the data presented in Aim 1.

The success of FDM PCU samples in Aim 2 is promising for the realization of the many benefits 3D printing can offer the biomedical field. However, with the success of these printed samples also comes a great deal of additional questions worthy of future studies. For instance, characterizing TPU morphology as a function of FDM printing parameters (nozzle temperature, layer thickness, etc.) may be of interest, as it was demonstrated that temperature profile can affect the resulting material properties. The samples of Aim 2 were printed at a relatively high nozzle temperature and low layer



thickness. As discussed, the high nozzle temperature thermodynamically favors smaller hard domains, and the low layer thickness results in a relatively rapid cooling rate, which may prohibit the reformation of any larger hard domains. In Aim 2, these effects led to a notable difference in strain behavior for injection molded versus FDM samples. However, during preliminary work for Aim 3 it was discovered that PCU crosshatch scaffolds demonstrated similar tensile behavior when printed at both 205°C and 225°C. This is likely due to the substantially larger size of the extrudate for crosshatch scaffolds versus solid samples (570 μm diameter round lines versus 150 μm thick smeared layers) as well as differences in cooling rate as solid sample extrusions were in direct contact with the cooler, previous layer whereas the crosshatch scaffolds lines were mostly surrounded by air. These differences may have mitigated the effect of nozzle temperature on resulting morphology. Therefore, further studies on the combined effects of nozzle temperature, extrudate thickness, and PCU grade on the resulting morphology would be of interest. In addition, characterizing the effects of various FDM parameters on overall sample properties (eg. effect of nozzle temperature on interlayer bonding and shear strength) may be of interest. The success of FDM samples in shear during Aim 2 is likely attributable to the relatively high nozzle temperature leading to melting of the previous, underlying layer thus yielding adequate bonding. It seems likely that this interlayer bond strength would be diminished with decreasing nozzle temperature, and therefore would be a valuable effect to investigate. Further studies on the effects of printing orientation, and method of infill, on the monotonic properties and fatigue performance would also be of interest. During investigation of the discrepancy in strain behavior between injection molded and FDM samples of Aim 2, monotonic tensions tests were performed on samples in which all printed lines were

oriented along the specimen axis instead of the  $\pm 45^\circ$  infill used in our study. Results seemingly indicated no difference for these two methods of infill, however this small study was certainly not an exhaustive effort. In addition, as mentioned in Chapter 4, performing tensile fatigue on samples in which the layers were printed perpendicular to the specimen axis would be of interest. Due to the compliant nature of the studied PCUs, as well as the slenderness of the custom dogbone geometry, we were unable to successfully print our fatigue samples in such a manner. However, perhaps by adjusting the dogbone geometry, samples may be printed in this manner. While the shear results for FDM samples indicated good interlayer bond strength, tensile fatigue on samples with layers perpendicular to the loading direction represents the most conservative case and therefore needs to be considered.

Taking clues from both Aims 2 and 3, another future study of interest would include relating 3D printed sample performance to void geometry and higher void fractions for future quality control standards. While the quality control standard for sample inclusion in Aim 2 was set at samples 99% solid and above, there was no notable difference in monotonic properties for any of our printed samples, whether they met the quality control criteria or not. However, all of our tested samples were over 98.4% solid. Therefore, developing a method to systematically print samples at larger void fractions, perhaps as much as 10% or more, in order to further probe this effect and develop a more meaningful standard based on empirical monotonic or fatigue data would be of great interest. Furthermore, investigations into the effect of geometry and orientation of voids on monotonic and fatigue performance would also be of interest. Voids due to the printing process can essentially be viewed as notches of varying intensity, and based on the results

of Aim 3, these notches likely have implications on fatigue performance. Therefore it would be of great interest to devise a method for determining the severity of included voids, likely relating to the void width, minimum radius, as well as orientation of the void with respect to loading, and examine the effect of this severity on sample fatigue performance for the purposes of future quality control specifications. Along these same lines, a more in-depth study of notch sensitivity, particularly with more severe notches or with different grades of materials, may provide more valuable insights into the effects of architectures and stress concentrations and allow for optimization of scaffolds from a fatigue standpoint.

In the theme of quality, another potential study of interest would be to investigate if further refinement to printing parameters could further increase sample quality over that seen in Aim 2. While the printing parameters specified in this work resulted in samples with adequate mechanical properties, based on results from the laser cut FDM samples (Section 6.4.2), it is likely the quality could be improved through further reductions in void fraction. Since the printed samples in Aim 2 were already low in terms of void fraction, it is likely any improvements would come from subtle differences in parameter values or print head control. To this end, it would be of interest to try repeating similar experiments with different FDM printers and/or slicing software. Improvements may also be realized through the use of printing filament with a more consistent diameter. Minor variations in filament diameter were noted for the PCU filament used in Aim 2. Success with FDM printers depends in large part on precise control over the amount of material extruded, and such variations in filament diameter would alter the rate of material extrusion and may potentially affect sample quality. Alternatively, working towards a method of precisely

monitoring the material extrusion rate from the nozzle and coupling this with real-time print head control adjustments could also address this issue.

Lastly, other studies of potential interest would include a longer oxidation study than that performed in Chapter 6, as well as further investigation into the effects of aging on PCU properties. The oxidation study performed in Chapter 6 simulated only one year *in vivo* as longer comparisons between the *in vivo* effects and the accelerated oxidation protocol have not yet been established. Results indicated that oxidation may have had a subtle effect on PCU fatigue performance, however for orthopedic applications, timeframes considerably longer than one year will be necessary. In addition, as noted in Chapter 6, aging of PCU had a notable effect on the material mechanical properties. In general, the material seems to exhibit an overall stiffening, with the monotonic tension plots demonstrating a leftward shift. Therefore, it is likely that aging has substantial effects on phase organization. Further characterization of this effect to longer time points with monotonic tests as well as perhaps FTIR, DMA, and DSC would certainly be of interest.

In conclusion, the studies presented in this work have provided several key findings. We have demonstrated the benefits of energy dissipation mechanisms for compressive fatigue, and illustrated the similarity in performance of toughened soft polymers to native soft tissue under high cycle compressive loading. We have demonstrated the effects of hard segment content on PCU fatigue performance as well as the remarkable potential for 3D printing of soft polyurethanes. To the best of the authors' knowledge, the work herein represents the first published work in which the mechanical performance, including fatigue, of injection molded samples was matched via FDM. Also, to the best of the authors' knowledge, the present work represents the first published work

in which the effect of architectures, beyond simple notches, has been investigated for soft polymers in fatigue. While there are a number of questions still to be answered, the studies presented in this work have nevertheless provided valuable insights that may assist in the development of future soft devices and have illustrated the potential that exists with 3D printing of soft materials.

## REFERENCES

1. Urban, J.P.G. and S. Roberts, *Degeneration of the intervertebral disc*. Arthritis Research & Therapy, 2003. **5**(3): p. 120.
2. An, H.S., et al., *Disc Degeneration: Summary*. Spine (Phila Pa 1976), 2004. **29**(23): p. 2677-8.
3. Luoma, K., et al., *Low back pain in relation to lumbar disc degeneration*. Spine (Phila Pa 1976), 2000. **25**(4): p. 487-92.
4. Hugle, T., et al., *Aging and osteoarthritis: an inevitable encounter?* J Aging Res, 2012. **2012**: p. 950192.
5. Bieleman, H.J., et al., *Functional capacity of people with early osteoarthritis: a comparison between subjects from the cohort hip and cohort knee (CHECK) and healthy ageing workers*. Int Arch Occup Environ Health, 2010. **83**(8): p. 913-21.
6. Han, K.S., et al., *Effect of centers of rotation on spinal loads and muscle forces in total disk replacement of lumbar spine*. Proc Inst Mech Eng H, 2013. **227**(5): p. 543-50.
7. Noble, P.C., et al., *Does total knee replacement restore normal knee function?* Clinical Orthopaedics And Related Research, 2005(431): p. 157-165.
8. Hilibrand, A.S., et al., *Radiculopathy and myelopathy at segments adjacent to the site of a previous anterior cervical arthrodesis*. The Journal Of Bone And Joint Surgery. American Volume, 1999. **81**(4): p. 519-528.
9. André van, O., F.C. Oner, and J.V. Ab, *Complications of Artificial Disc Replacement: A Report of 27 Patients with the SB Charité Disc*. Journal of Spinal Disorders, 2003. **16**(4): p. 369-383.
10. Christoph, M., *Heterotopic Ossification in Total Cervical Artificial Disc Replacement*. Spine, 2006. **31**(24): p. 2802-2806.
11. Punt, I.M., et al., *Complications and reoperations of the SB Charite lumbar disc prosthesis: experience in 75 patients*. Eur Spine J, 2008. **17**(1): p. 36-43.
12. Agarwal, S., R.K. Sharma, and J.K. Jain, *Periprosthetic fractures after total knee arthroplasty*. Journal Of Orthopaedic Surgery (Hong Kong), 2014. **22**(1): p. 24-29.
13. Au, A.G., et al., *Contribution of loading conditions and material properties to stress shielding near the tibial component of total knee replacements*. Journal of Biomechanics, 2007. **40**(6): p. 1410-1416.

14. Antunes, R.A. and M.C. de Oliveira, *Corrosion fatigue of biomedical metallic alloys: mechanisms and mitigation*. Acta Biomater, 2012. **8**(3): p. 937-62.
15. Cahoon, J.R. and R.N. Holte, *Corrosion fatigue of surgical stainless steel in synthetic physiological solution*. Journal Of Biomedical Materials Research, 1981. **15**(2): p. 137-145.
16. Dharme, M.R., A.M. Kuthe, and S.W. Dahake, *Comparison of Fatigue Analysis of Hip Joint Implant for Stainless Steel, Cobalt Chrome Alloys and Titanium Alloys*. Trends in Biomaterials & Artificial Organs, 2013. **27**(2): p. 58-61.
17. Fleck, C. and D. Eifler, *Corrosion, fatigue and corrosion fatigue behaviour of metal implant materials, especially titanium alloys*. International Journal of Fatigue, 2010. **32**(6): p. 929-935.
18. Gencur, S.J., C.M. Rimnac, and S.M. Kurtz, *Fatigue crack propagation resistance of virgin and highly crosslinked, thermally treated ultra-high molecular weight polyethylene*. Biomaterials, 2006. **27**(8): p. 1550-7.
19. Kurtz, S.M., et al., *The yielding, plastic flow, and fracture behavior of ultra-high molecular weight polyethylene used in total joint replacements*. Biomaterials, 1998. **19**(21): p. 1989-2003.
20. Niinomi, M. *Mechanical properties of biomedical titanium alloys*. 1998. Place of Publication: Wollongong, NSW, Australia. Country of Publication: Switzerland.: Elsevier U.S. Air Force Office of Sci. Res U.S. Air Force Office of Sci. Res.
21. Niinomi, M., et al., *Fatigue characteristics of ultra high molecular weight polyethylene with different molecular weight for implant material*. Journal Of Materials Science. Materials In Medicine, 2001. **12**(3): p. 267-272.
22. Papakyriacou, M., et al., *Effects of surface treatments on high cycle corrosion fatigue of metallic implant materials*. International Journal of Fatigue, 2000. **22**(10): p. 873-886.
23. Pruitt, L.A., *Deformation, yielding, fracture and fatigue behavior of conventional and highly cross-linked ultra high molecular weight polyethylene*. Biomaterials, 2005. **26**(8): p. 905-15.
24. Sauer, W.L., K.D. Weaver, and N.B. Beals, *Fatigue performance of ultra-high-molecular-weight polyethylene: effect of gamma radiation sterilization*. Biomaterials, 1996. **17**(20): p. 1929-1935.
25. Semlitsch, M. and H. Willert, *Properties of implant alloys for artificial hip joints*. Medical & Biological Engineering & Computing, 1980. **18**(4): p. 511.

26. Simis, K.S., et al., *The combined effects of crosslinking and high crystallinity on the microstructural and mechanical properties of ultra high molecular weight polyethylene*. *Biomaterials*, 2006. **27**(9): p. 1688-94.
27. Taira, M. and E.P. Lautenschlager, *In vitro corrosion fatigue of 316L cold worked stainless steel*. *Journal Of Biomedical Materials Research*, 1992. **26**(9): p. 1131-1139.
28. Teoh, S.H., *Fatigue of biomaterials: a review*. *International Journal of Fatigue*, 2000. **22**(10): p. 825-837.
29. Katti, K.S., *Biomaterials in total joint replacement*. *Colloids and Surfaces B: Biointerfaces*, 2004. **39**(3): p. 133-142.
30. Shan, Z., et al., *Correlation between biomechanical properties of the annulus fibrosus and magnetic resonance imaging (MRI) findings*. *European Spine Journal*, 2015. **24**(9): p. 1909-1916.
31. Hori, R.Y. and L. Mockros, *Indentation tests of human articular cartilage*. *Journal of Biomechanics*, 1976. **9**(4): p. 259-268.
32. Callister, W.D., *Materials science and engineering: an introduction*. 2003: John Wiley & Sons.
33. Źak, M. and C. Pezowicz, *Spinal sections and regional variations in the mechanical properties of the annulus fibrosus subjected to tensile loading*. *Acta of Bioengineering and Biomechanics*, 2013. **15**(1).
34. Garcia-Leiner, M., et al., *Structure-property relationships in commercial polyetheretherketone resins*. *Polymer Engineering & Science*, 2016.
35. Kurtz, S.M., *The UHMWPE handbook: ultra-high molecular weight polyethylene in total joint replacement*. 2004: Academic press.
36. Temple, D.K., et al., *Viscoelastic properties of human and bovine articular cartilage: a comparison of frequency-dependent trends*. *BMC Musculoskeletal Disorders*, 2016. **17**(1): p. 419.
37. Miller, A.T., et al., *Compressive cyclic ratcheting and fatigue of synthetic, soft biomedical polymers in solution*. *Journal of the mechanical behavior of biomedical materials*, 2016. **54**: p. 268-282.
38. Miller, A.T., et al., *Fatigue of injection molded and 3D printed polycarbonate urethane in solution*. *Polymer*, 2017. **108**: p. 121-134.
39. Swanson, A.B. and L.F. Peltier, *Silicone rubber implants for replacement of arthritic or destroyed joints in the hand*. *Clinical Orthopaedics & Related Research*, 1997. **342**: p. 4-10.



40. Chan, M., et al., *Silicone synovitis: MR imaging in five patients*. Skeletal Radiology, 1998. **27**(1): p. 13-17.
41. De Lurgio, D.B., et al., *Incidence and implications of abrasion of implantable cardioverter-defibrillator leads*. The American Journal Of Cardiology, 1997. **79**(10): p. 1409-1411.
42. Trepman, E. and F.C. Ewald, *Early failure of silicone radial head implants in the rheumatoid elbow. A complication of silicone radial head implant arthroplasty*. The Journal Of Arthroplasty, 1991. **6**(1): p. 59-65.
43. Vanderwilde, R.S., et al., *Inflammatory arthritis after failure of silicone rubber replacement of the radial head*. The Journal Of Bone And Joint Surgery. British Volume, 1994. **76**(1): p. 78-81.
44. Rosenthal, D.I., et al., *Destructive arthritis due to silicone: a foreign-body reaction*. Radiology, 1983. **149**(1): p. 69-72.
45. Cunningham, B.W., et al. *An analysis of the Acroflex Lumbar Disc as an intervertebral disc prosthesis: a nonhuman primate model*. 2001. Elsevier.
46. Fraser, R.D., et al., *Lumbar Disc Replacement: AcroFlex design and results*. The Spine Journal, 2004. **4**(Supplement): p. S245-S251.
47. Meir, A.R., et al., *2012 Outstanding Paper: Runner-up: Ten-year survival and clinical outcome of the AcroFlex lumbar disc replacement for the treatment of symptomatic disc degeneration*. The Spine Journal, 2013. **13**: p. 13-21.
48. Serhan, H., et al., *Biomechanical characterization of a new lumbar disc prosthesis*. Journal of Bone & Joint Surgery, British Volume, 2002. **84**(SUPP III): p. 215-215.
49. Quigley, F., M. Buggy, and C. Birkinshaw, *Selection of elastomeric materials for compliant-layered total hip arthroplasty*. Proceedings of the Institution of Mechanical Engineers, Part H: Journal of Engineering in Medicine, 2002. **216**(1): p. 77-83.
50. Baker, M.I., et al., *A review of polyvinyl alcohol and its uses in cartilage and orthopedic applications*. Journal of Biomedical Materials Research Part B: Applied Biomaterials, 2012. **100**(5): p. 1451-1457.
51. Hepburn, C., *Polyurethane elastomers*. 2012: Springer Science & Business Media.
52. Petrović, Z.S. and J. Ferguson, *Polyurethane elastomers*. Progress in Polymer Science, 1991. **16**(5): p. 695-836.

53. Christenson, E., J. Anderson, and A. Hiltner, *Biodegradation mechanisms of polyurethane elastomers*. Corrosion Engineering, Science and Technology, 2007. **42**(4): p. 312-323.
54. Treharne, R.W. and A. Greene, *The Case for the Use of Polycarbonate-Urethane in Orthopedic Implants*. Med-Tech, Spring, 2008. **1**: p. 18-22.
55. Stokes, K., R. McVenes, and J.M. Anderson, *Polyurethane elastomer biostability*. Journal of biomaterials applications, 1995. **9**(4): p. 321-354.
56. Wiggins, M.J., et al., *Effect of soft-segment chemistry on polyurethane biostability during in vitro fatigue loading*. Journal of Biomedical Materials Research Part A, 2004. **68**(4): p. 668-683.
57. Khan, I., et al., *Analysis and evaluation of a biomedical polycarbonate urethane tested in an in vitro study and an ovine arthroplasty model. Part I: materials selection and evaluation*. Biomaterials, 2005. **26**(6): p. 621-631.
58. Khan, I., et al., *Analysis and evaluation of a biomedical polycarbonate urethane tested in an in vitro study and an ovine arthroplasty model. Part II: in vivo investigation*. Biomaterials, 2005. **26**(6): p. 633-643.
59. Tanzi, M.C., et al., *Chemical stability of polyether urethanes versus polycarbonate urethanes*. Journal of biomedical materials research, 1997. **36**(4): p. 550-559.
60. Tanzi, M.C., S. Farè, and P. Petrini, *In vitro stability of polyether and polycarbonate urethanes*. Journal of biomaterials applications, 2000. **14**(4): p. 325-348.
61. Mathur, A.B., et al., *In vivo biocompatibility and biostability of modified polyurethanes*. Journal of biomedical materials research, 1997. **36**(2): p. 246-257.
62. Chandy, T., et al., *Long-term in vitro stability assessment of polycarbonate urethane micro catheters: Resistance to oxidation and stress cracking*. Journal of Biomedical Materials Research Part B: Applied Biomaterials, 2009. **89**(2): p. 314-324.
63. Christenson, E.M., J.M. Anderson, and A. Hiltner, *Oxidative mechanisms of poly (carbonate urethane) and poly (ether urethane) biodegradation: in vivo and in vitro correlations*. Journal of Biomedical Materials Research Part A, 2004. **70**(2): p. 245-255.
64. Christenson, E.M., et al., *Poly (carbonate urethane) and poly (ether urethane) biodegradation: in vivo studies*. Journal of Biomedical Materials Research Part A, 2004. **69**(3): p. 407-416.

65. Cipriani, E., et al., *In-vivo degradation of poly (carbonate-urethane) based spine implants*. Polymer degradation and stability, 2013. **98**(6): p. 1225-1235.
66. Kurtz, S., R. Siskey, and M. Reitman, *Accelerated aging, natural aging, and small punch testing of gamma-air sterilized polycarbonate urethane acetabular components*. Journal of Biomedical Materials Research Part B: Applied Biomaterials, 2010. **93**(2): p. 442-447.
67. Jin, J., et al., *An analysis on enhancement of fatigue durability of polyurethane by incorporating organoclay nanofillers*. Macromolecular Materials and Engineering, 2006. **291**(11): p. 1414-1421.
68. Oprea, S., *Effect of composition and hard-segment content on thermo-mechanical properties of cross-linked polyurethane copolymers*. High Performance Polymers, 2008.
69. Kaneko, Y., et al., *Effect of molecular weight distribution of poly (oxytetramethylene) glycol on cut growth resistance of polyurethane*. Journal of Applied Polymer Science, 1980. **25**(11): p. 2467-2478.
70. Jimenez, G., et al., *Effect of the soft segment on the fatigue behavior of segmented polyurethanes*. European Polymer Journal, 2000. **36**(9): p. 2039-2050.
71. El Fray, M. and V. Altstädt, *Fatigue behaviour of multiblock thermoplastic elastomers. 1. Stepwise increasing load testing of poly(aliphatic/aromatic-ester) copolymers*. Polymer, 2003. **44**: p. 4635-4642.
72. El Fray, M. and V. Altstädt, *Fatigue behaviour of multiblock thermoplastic elastomers. 2. Dynamic creep of poly(aliphatic/aromatic-ester) copolymers*. Polymer, 2003. **44**: p. 4643-4650.
73. Fray, M.E. and V. Altstädt, *Fatigue behaviour of multiblock thermoplastic elastomers. 3. Stepwise increasing strain test of poly(aliphatic/aromatic-ester) copolymers*. Polymer, 2004. **45**: p. 263-273.
74. Cristiano, A., et al., *Fracture of model polyurethane elastomeric networks*. Journal of Polymer Science Part B: Polymer Physics, 2011. **49**(5): p. 355-367.
75. Song, M., et al., *High performance nanocomposites of polyurethane elastomer and organically modified layered silicate*. Journal of applied polymer science, 2003. **90**(12): p. 3239-3243.
76. Pukánszky, B., et al., *Nanophase separation in segmented polyurethane elastomers: Effect of specific interactions on structure and properties*. European Polymer Journal, 2008. **44**(8): p. 2431-2438.

77. Bagdi, K., et al., *Quantitative estimation of the strength of specific interactions in polyurethane elastomers, and their effect on structure and properties*. European polymer journal, 2012. **48**(11): p. 1854-1865.
78. Kim, C.K., et al., *Structure-property relationships of hydroxy-terminated polyether based polyurethane network*. Polymer Bulletin, 2008. **61**(2): p. 225-233.
79. Jin, J., et al., *A study on viscoelasticity of polyurethane–organoclay nanocomposites*. Journal of applied polymer science, 2006. **99**(6): p. 3677-3683.
80. Bagdi, K., et al., *Thermal analysis of the structure of segmented polyurethane elastomers: relation to mechanical properties*. Journal of thermal analysis and calorimetry, 2009. **98**(3): p. 825-832.
81. Saralegi, A., et al., *Thermoplastic polyurethanes from renewable resources: effect of soft segment chemical structure and molecular weight on morphology and final properties*. Polymer International, 2013. **62**(1): p. 106-115.
82. Corcuera, M., et al. *Effect of Diisocyanate Structure on Thermal Properties and Microstructure of Polyurethanes Based on Polyols Derived from Renewable Resources*. in *V INTERNATIONAL CONFERENCE ON TIMES OF POLYMERS (TOP) AND COMPOSITES*. 2010. AIP Publishing.
83. Kuta, A., et al., *The influence of macrodiol type on the mechanical properties of polyurethane materials*. Materials and Manufacturing Processes, 2009. **24**(10-11): p. 1214-1216.
84. Špírková, M., et al., *Novel polycarbonate-based polyurethane elastomers: Composition–property relationship*. European Polymer Journal, 2011. **47**(5): p. 959-972.
85. Kojio, K., et al., *Structure– mechanical property relationships for poly (carbonate urethane) elastomers with novel soft segments*. Macromolecules, 2009. **42**(21): p. 8322-8327.
86. Guo, J., et al., *Study on structure and performance of polycarbonate urethane synthesized via different copolymerization methods*. Journal of materials science, 2007. **42**(14): p. 5508-5515.
87. Kultys, A., et al., *The synthesis and characterization of new thermoplastic poly (carbonate-urethane) elastomers derived from HDI and aliphatic–aromatic chain extenders*. European Polymer Journal, 2009. **45**(9): p. 2629-2643.
88. Eceiza, A., et al., *Thermoplastic polyurethane elastomers based on polycarbonate diols with different soft segment molecular weight and chemical structure: mechanical and thermal properties*. Polymer Engineering & Science, 2008. **48**(2): p. 297-306.

89. Rodriguez, E., et al., *Fatigue cut growth of thermoplastic polyurethanes*. Journal of reinforced plastics and composites, 1994. **13**(1): p. 2-19.
90. Lazennec, J.Y., et al., *The Viscoelastic LP-ESP Lumbar Disc Prosthesis With 6 Degrees of Freedom: A Prospective Study of 120 Patients With Two Years' Minimum Follow-Up*. Bone & Joint Journal Orthopaedic Proceedings Supplement, 2013. **95**(SUPP 34): p. 389-389.
91. Lazennec, J.-Y., et al., *The LP-ESP® lumbar disc prosthesis with 6 degrees of freedom: development and 7 years of clinical experience*. European Journal of Orthopaedic Surgery & Traumatology, 2013. **23**(2): p. 131-143.
92. Lazennec, J.-Y., et al., *The LP-ESP Lumbar Disc Prosthesis: Concept, Development and Clinical Experience*. 2013: INTECH Open Access Publisher.
93. Lazennec, J.-Y., et al. *ONE-YEAR FOLLOW-UP AFTER LP-ESP® LUMBAR DISC REPLACEMENT: CLINICAL AND RADIOLOGICAL OUTCOMES INCLUDING MEAN CENTER OF ROTATION AND SAGITTAL BALANCE: GP243*. in *Spine Journal Meeting Abstracts*. 2011. LWW.
94. Lazennec, J.-Y., et al., *Clinical outcomes, radiologic kinematics, and effects on sagittal balance of the 6 df LP-ESP lumbar disc prosthesis*. The Spine Journal, 2014. **14**(9): p. 1914-1920.
95. Anekstein, Y., et al., *Seven years follow-up for total lumbar facet joint replacement (TOPS) in the management of lumbar spinal stenosis and degenerative spondylolisthesis*. European Spine Journal, 2015: p. 1-9.
96. McAfee, P., et al., *Treatment of lumbar spinal stenosis with a total posterior arthroplasty prosthesis: implant description, surgical technique, and a prospective report on 29 patients*. Neurosurgical focus, 2007. **22**(1): p. 1-11.
97. Cao, F., et al., *Comparison of Clinical and Radiographic Changes after Bryan Disc Arthroplasty versus ACDF: A 60-Month Follow-Up on 120 Patients*. World Journal of Neuroscience, 2015. **5**(01): p. 40.
98. Quan, G.M., et al., *Eight-year clinical and radiological follow-up of the Bryan cervical disc arthroplasty*. Spine, 2011. **36**(8): p. 639-646.
99. Rao, M.-J., et al., *Cervical disc arthroplasty versus anterior cervical discectomy and fusion for treatment of symptomatic cervical disc disease: a meta-analysis of randomized controlled trials*. Archives of orthopaedic and trauma surgery, 2015. **135**(1): p. 19-28.
100. Laurysen, C., et al., *Cervical total disc replacement using a novel compressible prosthesis: Results from a prospective Food and Drug Administration–regulated feasibility study with 24-month follow-up*. The International Journal of Spine Surgery, 2012. **6**(1): p. 71-77.

101. Reyes-Sanchez, A., et al., *Initial clinical experience with a next-generation artificial disc for the treatment of symptomatic degenerative cervical radiculopathy*. SAS Journal, 2010. **4**(1): p. 9-15.
102. Thomas, S., et al., *The M6-C Cervical Disc Prosthesis: First Clinical Experience In 33 Patients*. Journal of spinal disorders & techniques, 2013.
103. Rischke, B., et al., *Preclinical and clinical experience with a viscoelastic total disc replacement*. SAS Journal, 2011. **5**(4): p. 97-107.
104. Scholes, S., et al., *Compliant layer acetabular cups: friction testing of a range of materials and designs for a new generation of prosthesis that mimics the natural joint*. Proceedings of the Institution of Mechanical Engineers, Part H: Journal of Engineering in Medicine, 2006. **220**(5): p. 583-596.
105. Kurtz, S.M., *Retrieval analysis of a polycarbonate-urethane acetabular cup: a case report*. Journal of long-term effects of medical implants, 2008. **18**(1).
106. Smith, S., H. Ash, and A. Unsworth, *A tribological study of UHMWPE acetabular cups and polyurethane compliant layer acetabular cups*. Journal of biomedical materials research, 2000. **53**(6): p. 710-716.
107. John, K.S. and M. Gupta, *Evaluation of the wear performance of a polycarbonate-urethane acetabular component in a hip joint simulator and comparison with UHMWPE and cross-linked UHMWPE*. Journal of biomaterials applications, 2012. **27**(1): p. 55-65.
108. Elsner, J.J., et al., *Long-term evaluation of a compliant cushion form acetabular bearing for hip joint replacement: A 20 million cycles wear simulation*. Journal of Orthopaedic Research, 2011. **29**(12): p. 1859-1866.
109. Elsner, J.J., et al., *Wear rate evaluation of a novel polycarbonate-urethane cushion form bearing for artificial hip joints*. Acta biomaterialia, 2010. **6**(12): p. 4698-4707.
110. Elsner, J., et al., *A Novel Polycarbonate-Urethane Meniscal Implant: From Bench to First Clinical Experience*. Journal of Bone & Joint Surgery, British Volume, 2012. **94**(SUPP XL): p. 125-125.
111. Shemesh, M., et al., *Viscoelastic properties of a synthetic meniscus implant*. journal of the mechanical behavior of biomedical materials, 2014. **29**: p. 42-55.
112. Cook, J.L., et al., *Evaluation of synthetic osteochondral implants*. The journal of knee surgery, 2014. **27**(4): p. 295-302.
113. Daebritz, S.H., et al., *Introduction of a flexible polymeric heart valve prosthesis with special design for aortic position*. European journal of cardio-thoracic surgery, 2004. **25**(6): p. 946-952.

114. Daebritz, S.H., et al., *Introduction of a flexible polymeric heart valve prosthesis with special design for mitral position*. *Circulation*, 2003. **108**(10 suppl 1): p. II-134-II-139.
115. John, K.R.S., *The use of polyurethane materials in the surgery of the spine: a review*. *The Spine Journal*, 2014. **14**(12): p. 3038-3047.
116. Rajaei, S.S., et al., *Spinal fusion in the United States: analysis of trends from 1998 to 2008*. *Spine*, 2012. **37**(1): p. 67-76.
117. Mars, W. and A. Fatemi, *A literature survey on fatigue analysis approaches for rubber*. *International Journal of Fatigue*, 2002. **24**(9): p. 949-961.
118. Papadopoulos, I., *Predicting the fatigue life of elastomer components*. 2006, Queen Mary, University of London.
119. Thomas, A., *The development of fracture mechanics for elastomers*. *Rubber Chemistry and Technology*, 1994. **67**(3): p. 50-67.
120. Zarrin-Ghalami, T. and A. Fatemi, *Material deformation and fatigue behavior characterization for elastomeric component life predictions*. *Polymer Engineering & Science*, 2012. **52**(8): p. 1795-1805.
121. Legorju-Jago, K. and C. Bathias, *Fatigue initiation and propagation in natural and synthetic rubbers*. *International Journal of Fatigue*, 2002. **24**(2): p. 85-92.
122. Mars, W. and A. Fatemi, *Factors that affect the fatigue life of rubber: a literature survey*. *Rubber Chemistry and Technology*, 2004. **77**(3): p. 391-412.
123. Fitzgerald, J.J., et al., *The effect of cyclic stress on the physical properties of a poly (dimethylsiloxane) elastomer*. *Polymer Engineering & Science*, 1992. **32**(18): p. 1350-1357.
124. Flamm, M., et al., *Effects of very high loads on fatigue life of NR elastomer materials*. *International Journal of Fatigue*, 2011. **33**(9): p. 1189-1198.
125. Harbour, R.J., A. Fatemi, and W.V. Mars, *Fatigue life analysis and predictions for NR and SBR under variable amplitude and multiaxial loading conditions*. *International Journal of Fatigue*, 2008. **30**(7): p. 1231-1247.
126. Fitzgerald, J., W. Ferrar, and T. Binga, *Fatigue-resistant silicone elastomer formulations*. *Journal of applied polymer science*, 1998. **70**(8): p. 1633-1641.
127. Lemieux, M.A. and P.C. Killgoar Jr, *Low modulus, high damping, high fatigue life elastomer compounds for vibration isolation*. *Rubber chemistry and technology*, 1984. **57**(4): p. 792-803.

128. Mars, W. and A. Fatemi, *Multiaxial stress effects on fatigue behavior of filled natural rubber*. International Journal of Fatigue, 2006. **28**(5): p. 521-529.
129. Alshuth, T., F. Abraham, and S. Jerrams, *Parameter dependence and prediction of fatigue properties of elastomer products*. Rubber Chemistry and Technology, 2002. **75**(4): p. 635-642.
130. McMillin, C.R., *Biomedical applications of rubbers and elastomers*. Rubber chemistry and technology, 2006. **79**(3): p. 500-519.
131. Yoda, R., *Elastomers for biomedical applications*. Journal of Biomaterials Science, Polymer Edition, 1998. **9**(6): p. 561-626.
132. Smith, K.E., J.S. Temenoff, and K. Gall, *On the toughness of photopolymerizable (meth) acrylate networks for biomedical applications*. Journal of applied polymer science, 2009. **114**(5): p. 2711-2722.
133. Chaffin, K.A., et al., *Influence of water on the structure and properties of PDMS-containing multiblock polyurethanes*. Macromolecules, 2012. **45**(22): p. 9110-9120.
134. Chaffin, K.A., et al., *Abrasion and fatigue resistance of PDMS containing multiblock polyurethanes after accelerated water exposure at elevated temperature*. Biomaterials, 2013. **34**(33): p. 8030-8041.
135. Wiggins, M.J., J.M. Anderson, and A. Hiltner, *Effect of strain and strain rate on fatigue-accelerated biodegradation of polyurethane*. Journal of Biomedical Materials Research Part A, 2003. **66**(3): p. 463-475.
136. Wiggins, M.J., J.M. Anderson, and A. Hiltner, *Biodegradation of polyurethane under fatigue loading*. Journal of Biomedical Materials Research Part A, 2003. **65**(4): p. 524-535.
137. Hayashi, K., et al., *Effects of immersion in cholesterol-lipid solution on the tensile and fatigue properties of elastomeric polymers for blood pump applications*. Journal of biomedical materials research, 1984. **18**(8): p. 939-951.
138. Sevastianov, V. and V. Parfeev, *Fatigue and hemocompatibility of polymer materials*. Artificial organs, 1987. **11**(1): p. 20-25.
139. Hayashi, K., *Fatigue properties of segmented polyether polyurethanes for cardiovascular applications*. ASTM SPECIAL TECHNICAL PUBLICATION, 1994. **1173**: p. 9-9.
140. Hayashi, K., et al., *Mechanical stability of elastomeric polymers for blood pump applications*. Journal of biomedical materials research, 1985. **19**(2): p. 179-193.



141. McMillin, C.R., *Physical testing of elastomers for cardiovascular applications*. Artificial organs, 1983. **7**(1): p. 78-91.
142. Mcmillin, C.R., *Characterization of hexsyn, a polyolefin rubber*. Journal of biomaterials applications, 1987. **2**(1): p. 3-99.
143. Murayama, T. and C. McMillin, *Dynamic mechanical properties of elastomers for use in circulatory assist devices*. Journal of Applied Polymer Science, 1983. **28**(6): p. 1871-1877.
144. McKenna, G. and R. Penn, *Time-dependent failure of a polyolefin rubber candidate material for blood pump applications*. Journal of biomedical materials research, 1980. **14**(5): p. 689-703.
145. Takahara, A., et al., *Effect of aggregation state of hard segment in segmented poly(urethaneureas) on their fatigue behavior after interaction with blood components*. Journal of biomedical materials research, 1985. **19**(1): p. 13-34.
146. El Fray, M., et al., *Biocompatibility and fatigue properties of polystyrene-polyisobutylene-polystyrene, an emerging thermoplastic elastomeric biomaterial*. Biomacromolecules, 2006. **7**(3): p. 844-850.
147. Puskas, J.E. and Y. Chen, *Biomedical application of commercial polymers and novel polyisobutylene-based thermoplastic elastomers for soft tissue replacement*. Biomacromolecules, 2004. **5**(4): p. 1141-1154.
148. Puskas, J.E., et al., *Dynamic stress relaxation of thermoplastic elastomeric biomaterials*. Polymer, 2009. **50**(1): p. 245-249.
149. El Fray, M., J.E. Puskas, and V. Altstädt, *THE EFFECT OF CHEMICAL STRUCTURE AND PHASE MORPHOLOGY ON THE FATIGUE PROPERTIES OF THERMOPLASTIC ELASTOMER BIOMATERIALS*. Polymer Preprints, 2006. **47**(2): p. 51.
150. Puskas, J.E., et al., *Fatigue testing of implantable specimens: Effect of sample size and branching on the dynamic fatigue properties of polyisobutylene-based biomaterials*. Polymer, 2009. **50**(2): p. 591-597.
151. Götz, C., et al., *Investigation of structure–property relationships of polyisobutylene-based biomaterials: Morphology, thermal, quasi-static tensile and long-term dynamic fatigue behavior*. Journal of the mechanical behavior of biomedical materials, 2012. **10**: p. 206-215.
152. Pinchuk, L., et al., *Medical applications of poly(styrene-block-isobutylene-block-styrene) (“SIBS”)*. Biomaterials, 2008. **29**(4): p. 448-460.

153. Pavka, P.A., *Effect of Network Structure on the Quasi-static, Fatigue, Creep, Thermal and Fiber Properties of Polyisobutylene-based Thermoplastic Elastomers*. 2013, The University of Akron.
154. Götz, C., et al., *Influence of e-beam irradiation on the dynamic creep and fatigue properties of poly (aliphatic/aromatic-ester) copolymers for biomedical applications*. *Polymer*, 2009. **50**(23): p. 5499-5507.
155. Götz, C., et al., *The effect of carbon black reinforcement on the dynamic fatigue and creep of polyisobutylene-based biomaterials*. *Journal of the mechanical behavior of biomedical materials*, 2014. **39**: p. 355-365.
156. Helsen, J., et al., *Evaluation of an elastomer for biomedical use in load-bearing applications*. *Journal of Materials Science: Materials in Medicine*, 1993. **4**(5): p. 471-480.
157. Safranski, D.L., et al., *Thermo-mechanical properties of semi-degradable Poly ( $\beta$ -amino ester)-co-methyl methacrylate networks under simulated physiological conditions*. *Polymer*, 2011. **52**(21): p. 4920-4927.
158. Safranski, D.L., et al., *Semi-degradable poly ( $\beta$ -amino ester) networks with temporally controlled enhancement of mechanical properties*. *Acta biomaterialia*, 2014. **10**(8): p. 3475-3483.
159. Smith, K.E., et al., *Long-term toughness of photopolymerizable (meth) acrylate networks in aqueous environments*. *Acta biomaterialia*, 2011. **7**(2): p. 558-567.
160. Smith, K.E., et al., *The effect of the glass transition temperature on the toughness of photopolymerizable (meth) acrylate networks under physiological conditions*. *Polymer*, 2009. **50**(21): p. 5112-5123.
161. Safranski, D.L. and K. Gall, *Effect of chemical structure and crosslinking density on the thermo-mechanical properties and toughness of (meth) acrylate shape memory polymer networks*. *Polymer*, 2008. **49**(20): p. 4446-4455.
162. Moore, J.P. and C.B. Williams, *Fatigue properties of parts printed by PolyJet material jetting*. *Rapid Prototyping Journal*, 2015. **21**(6): p. 675-685.
163. Ziemian, C., R. Ziemian, and K. Haile, *Characterization of stiffness degradation caused by fatigue damage of additive manufactured parts*. *Materials & Design*, 2016. **109**: p. 209-218.
164. Lee, J. and A. Huang, *Fatigue analysis of FDM materials*. *Rapid Prototyping Journal*, 2013. **19**(4): p. 291-299.
165. Ziemian, S., M. Okwara, and C.W. Ziemian, *Tensile and fatigue behavior of layered acrylonitrile butadiene styrene*. *Rapid Prototyping Journal*, 2015. **21**(3): p. 270-278.

166. Amel, H., et al., *Effect of section thickness on fatigue performance of laser sintered nylon 12*. Polymer Testing, 2016.
167. Munguia, J. and K. Dalgarno, *Fatigue behaviour of laser sintered Nylon 12 in rotating and reversed bending tests*. Materials Science and Technology, 2015. **31**(8): p. 904-911.
168. Munguia, J. and K. Dalgarno, *Fatigue behaviour of laser-sintered PA12 specimens under four-point rotating bending*. Rapid Prototyping Journal, 2014. **20**(4): p. 291-300.
169. Salazar, A., et al., *Fatigue crack growth of SLS polyamide 12: Effect of reinforcement and temperature*. Composites Part B: Engineering, 2014. **59**: p. 285-292.
170. Van Hooreweder, B. and J.-P. Kruth, *High cycle fatigue properties of selective laser sintered parts in polyamide 12*. CIRP Annals-Manufacturing Technology, 2014. **63**(1): p. 241-244.
171. Blattmeier, M., et al., *Influence of surface characteristics on fatigue behaviour of laser sintered plastics*. Rapid Prototyping Journal, 2012. **18**(2): p. 161-171.
172. Amel, H., et al., *Investigating the behavior of laser-sintered Nylon 12 parts subject to dynamic loading*. Journal of Materials Research, 2014. **29**(17): p. 1852-1858.
173. Van Hooreweder, B., et al., *Microstructural characterization of SLS-PA12 specimens under dynamic tension/compression excitation*. Polymer testing, 2010. **29**(3): p. 319-326.
174. Salazar, A., et al., *Monotonic loading and fatigue response of a bio-based polyamide PA11 and a petrol-based polyamide PA12 manufactured by selective laser sintering*. European Polymer Journal, 2014. **59**: p. 36-45.
175. Van Hooreweder, B., et al., *On the difference in material structure and fatigue properties of nylon specimens produced by injection molding and selective laser sintering*. Polymer Testing, 2013. **32**(5): p. 972-981.
176. Santerre, J., et al., *Understanding the biodegradation of polyurethanes: from classical implants to tissue engineering materials*. Biomaterials, 2005. **26**(35): p. 7457-7470.
177. Zdrahala, R.J. and I.J. Zdrahala, *Biomedical applications of polyurethanes: a review of past promises, present realities, and a vibrant future*. Journal of biomaterials applications, 1999. **14**(1): p. 67-90.
178. Evans, N.T., et al., *High-strength, surface-porous polyether-ether-ketone for load-bearing orthopedic implants*. Acta biomaterialia, 2015. **13**: p. 159-167.

179. Evans, N.T., *Processing-Structure-Property Relationships of Surface Porous Polymers for Orthopaedic Applications*. 2016.
180. Hoyt, A.J., et al., *Monotonic and cyclic loading behavior of porous scaffolds made from poly (para-phenylene) for orthopedic applications*. Journal of the mechanical behavior of biomedical materials, 2015. **41**: p. 136-148.
181. Li, S., et al., *Compression fatigue behavior of Ti-6Al-4V mesh arrays fabricated by electron beam melting*. Acta Materialia, 2012. **60**(3): p. 793-802.
182. Hrabe, N.W., et al., *Compression-compression fatigue of selective electron beam melted cellular titanium (Ti-6Al-4V)*. Journal of Biomedical Materials Research Part B: Applied Biomaterials, 2011. **99**(2): p. 313-320.
183. Wolfarth, D. and P. Ducheyne, *Effect of a change in interfacial geometry on the fatigue strength of porous-coated Ti-6Al-4V*. Journal of biomedical materials research, 1994. **28**(4): p. 417-425.
184. Cook, S.D., et al., *The effect of post-sintering heat treatments on the fatigue properties of porous coated Ti-6Al-4V Alloy*. Journal of biomedical materials research, 1988. **22**(4): p. 287-302.
185. Yavari, S.A., et al., *Fatigue behavior of porous biomaterials manufactured using selective laser melting*. Materials Science and Engineering: C, 2013. **33**(8): p. 4849-4858.
186. Cook, S.D., et al., *Fatigue properties of carbon-and porous-coated Ti-6Al-4V alloy*. Journal of biomedical materials research, 1984. **18**(5): p. 497-512.
187. Yue, S., R. Pilliar, and G. Weatherly, *The fatigue strength of porous-coated Ti-6% Al-4% V implant alloy*. Journal of biomedical materials research, 1984. **18**(9): p. 1043-1058.
188. Kohn, D.H. and P. Ducheyne, *A parametric study of the factors affecting the fatigue strength of porous coated Ti-6Al-4V implant alloy*. Journal of biomedical materials research, 1990. **24**(11): p. 1483-1501.
189. Yavari, S.A., et al., *Relationship between unit cell type and porosity and the fatigue behavior of selective laser melted meta-biomaterials*. Journal of the mechanical behavior of biomedical materials, 2015. **43**: p. 91-100.
190. Sevilla, P., et al., *Comparison of the mechanical properties between tantalum and nickel-titanium foams implant materials for bone ingrowth applications*. Journal of Alloys and Compounds, 2007. **439**(1): p. 67-73.
191. Wernle, J. and M. Dharia, *POROUS SCAFFOLD PERFORMANCE FOR FOOT AND ANKLE APPLICATIONS: MATERIAL AND SHAPE AS PREDICTORS FOR FRACTURE*. Bone Joint J, 2016. **98**(SUPP 10): p. 127-127.

192. Zardiackas, L.D., et al., *Structure, metallurgy, and mechanical properties of a porous tantalum foam*. Journal of biomedical materials research, 2001. **58**(2): p. 180-187.
193. McNamara, J., *Novel Approaches to the Analysis of Localised Stress Concentrations in Deformed Elastomers*. 2011.
194. Balazs, C., *Mechanical Design and Notch Sensitivity of Molding Materials*. 1964, DTIC Document.
195. Takano, M. and L.E. Nielsen, *The notch sensitivity of polymeric materials*. Journal of Applied Polymer Science, 1976. **20**(8): p. 2193-2207.
196. Andrews, E., *Rupture propagation in hysterical materials: stress at a notch*. Journal of the Mechanics and Physics of Solids, 1963. **11**(4): p. 231-242.
197. Whittaker, R.E., *Cut growth and fatigue properties of cellular polyurethane elastomers*. Journal of Applied Polymer Science, 1974. **18**(8): p. 2339-2353.
198. Zielinska, B. and T.L.H. Donahue, *3D finite element model of meniscectomy: changes in joint contact behavior*. Journal of biomechanical engineering, 2006. **128**(1): p. 115-123.
199. Apfel, C.C., et al., *Restoration of disk height through non-surgical spinal decompression is associated with decreased discogenic low back pain: a retrospective cohort study*. BMC musculoskeletal disorders, 2010. **11**(1): p. 155.
200. Coleman, J.L., et al., *Diurnal variations in articular cartilage thickness and strain in the human knee*. Journal of biomechanics, 2013. **46**(3): p. 541-547.
201. Lötters, J., et al., *The mechanical properties of the rubber elastic polymer polydimethylsiloxane for sensor applications*. Journal of Micromechanics and Microengineering, 1997. **7**(3): p. 145.
202. Pimbert, S., L. Avignon-Poquillon, and G. Levesque. *Relations between glass transition temperatures in miscible polymer blends and composition: from volume to mass fractions*. in *Macromolecular Symposia*. 2005. Wiley Online Library.
203. Adams, M.A. and T.P. Green, *Tensile properties of the annulus fibrosus. I. The contribution of fibre-matrix interactions to tensile stiffness and strength*. Eur Spine J, 1993. **2**(4): p. 203-8.
204. Burr, D.B., et al., *Bone remodeling in response to in vivo fatigue microdamage*. Journal of biomechanics, 1985. **18**(3): p. 189-200.
205. Clarkson, P.M. and I. Tremblay, *Exercise-induced muscle damage, repair, and adaptation in humans*. Journal of Applied Physiology, 1988. **65**(1): p. 1-6.

206. Bentolila, V., et al., *Intracortical remodeling in adult rat long bones after fatigue loading*. Bone, 1998. **23**(3): p. 275-281.
207. Lakhera, N., K.E. Smith, and C.P. Frick, *Systematic tailoring of water absorption in photopolymerizable (meth) acrylate networks and its effect on mechanical properties*. Journal of Applied Polymer Science, 2013. **128**(3): p. 1913-1921.
208. Hertzberg, R.W., H. Nordberg, and J. Manson, *Fatigue crack propagation in polymeric materials*. Journal of Materials Science, 1970. **5**(6): p. 521-526.
209. Riddell, M., G. Koo, and J. O'Toole, *Fatigue mechanisms of thermoplastics*. Polymer Engineering & Science, 1966. **6**(4): p. 363-368.
210. Zhao, X., *Multi-scale multi-mechanism design of tough hydrogels: building dissipation into stretchy networks*. Soft Matter, 2014. **10**(5): p. 672-687.
211. Proctor, C., et al., *Material properties of the normal medial bovine meniscus*. Journal of Orthopaedic Research, 1989. **7**(6): p. 771-782.
212. Bursac, P., S. Arnoczky, and A. York, *Dynamic compressive behavior of human meniscus correlates with its extra-cellular matrix composition*. Biorheology, 2008. **46**(3): p. 227-237.
213. Constable, I., J. Williams, and D. Burns, *Fatigue and cyclic thermal softening of thermoplastics*. Journal of Mechanical Engineering Science, 1970. **12**(1): p. 20-29.
214. Crawford, R. and P. Benham, *Cyclic stress fatigue and thermal softening failure of a thermoplastic*. Journal of Materials Science, 1974. **9**(1): p. 18-28.
215. Park, S., C. Hung, and G. Ateshian, *Mechanical response of bovine articular cartilage under dynamic unconfined compression loading at physiological stress levels*. Osteoarthritis and cartilage, 2004. **12**(1): p. 65-73.
216. Li, L., M. Buschmann, and A. Shirazi-Adl, *Strain-rate dependent stiffness of articular cartilage in unconfined compression*. Journal of biomechanical engineering, 2003. **125**(2): p. 161-168.
217. Kazemi, M., et al., *Creep behavior of the intact and meniscectomy knee joints*. Journal of the Mechanical Behavior of Biomedical Materials, 2011. **4**(7): p. 1351-1358.
218. Chia, H.N. and M. Hull, *Compressive moduli of the human medial meniscus in the axial and radial directions at equilibrium and at a physiological strain rate*. Journal of Orthopaedic Research, 2008. **26**(7): p. 951-956.

219. Joshi, M.D., et al., *Interspecies variation of compressive biomechanical properties of the meniscus*. Journal of biomedical materials research, 1995. **29**(7): p. 823-828.
220. McDermott, I.D., S.D. Masouros, and A.A. Amis, *Biomechanics of the menisci of the knee*. Current Orthopaedics, 2008. **22**(3): p. 193-201.
221. Sandmann, G.H., et al., *Biomechanical comparison of menisci from different species and artificial constructs*. BMC musculoskeletal disorders, 2013. **14**(1): p. 324.
222. Sweigart, M., et al., *Intraspecies and interspecies comparison of the compressive properties of the medial meniscus*. Annals of biomedical engineering, 2004. **32**(11): p. 1569-1579.
223. Uezaki, N., A. Kobayashi, and K. Matsushige, *The viscoelastic properties of the human semilunar cartilage*. Journal of biomechanics, 1979. **12**(1): p. 65-73.
224. Zhu, W., K.Y. Chern, and M. van C, *Anisotropic viscoelastic shear properties of bovine meniscus*. Clinical orthopaedics and related research, 1994. **306**: p. 34-45.
225. Tien, Y. and K. Wei, *Hydrogen bonding and mechanical properties in segmented montmorillonite/polyurethane nanocomposites of different hard segment ratios*. Polymer, 2001. **42**(7): p. 3213-3221.
226. Bižal, A., J. Klemenc, and M. Fajdiga, *Evaluating the Statistical Significance of a Fatigue-Life Reduction Due to Macro-Porosity*. Strojniški vestnik-Journal of Mechanical Engineering, 2014. **60**(6): p. 407-416.
227. Tanaka, H. and M. Kunimura, *Mechanical properties of thermoplastic polyurethanes containing aliphatic polycarbonate soft segments with different chemical structures*. Polymer Engineering & Science, 2002. **42**(6): p. 1333-1349.
228. Lee, H.S. and S.L. Hsu, *An analysis of phase separation kinetics of model polyurethanes*. Macromolecules, 1989. **22**(3): p. 1100-1105.
229. Myers, C.W.S., *Morphology and fatigue properties of polyurethane thermoplastic elastomers*. Dissertation Abstracts International(USA), 1994. **55**(1): p. 199.
230. Pompe, G., et al., *Influence of processing conditions on the multiphase structure of segmented polyurethane*. Polymer, 1998. **39**(21): p. 5147-5153.
231. Cipriani, E., et al., *Thermoplastic polyurethanes with polycarbonate soft phase: effect of thermal treatment on phase morphology*. Polymer degradation and stability, 2012. **97**(9): p. 1794-1800.
232. Hollister, S.J., *Porous scaffold design for tissue engineering*. Nature materials, 2005. **4**(7): p. 518-524.

233. Williams, J.M., et al., *Bone tissue engineering using polycaprolactone scaffolds fabricated via selective laser sintering*. *Biomaterials*, 2005. **26**(23): p. 4817-4827.
234. Knutsen, A.R., et al., *Static and dynamic fatigue behavior of topology designed and conventional 3D printed bioresorbable PCL cervical interbody fusion devices*. *Journal of the mechanical behavior of biomedical materials*, 2015. **49**: p. 332-342.
235. Moroni, L., J. De Wijn, and C. Van Blitterswijk, *3D fiber-deposited scaffolds for tissue engineering: influence of pores geometry and architecture on dynamic mechanical properties*. *Biomaterials*, 2006. **27**(7): p. 974-985.
236. Korpela, J., et al., *Biodegradable and bioactive porous scaffold structures prepared using fused deposition modeling*. *Journal of Biomedical Materials Research Part B: Applied Biomaterials*, 2013. **101**(4): p. 610-619.
237. Woodfield, T.B., et al., *Design of porous scaffolds for cartilage tissue engineering using a three-dimensional fiber-deposition technique*. *Biomaterials*, 2004. **25**(18): p. 4149-4161.
238. Kalita, S.J., et al., *Development of controlled porosity polymer-ceramic composite scaffolds via fused deposition modeling*. *Materials Science and Engineering: C*, 2003. **23**(5): p. 611-620.
239. Domingos, M., et al., *Effect of process parameters on the morphological and mechanical properties of 3D bioextruded poly ( $\epsilon$ -caprolactone) scaffolds*. *Rapid Prototyping Journal*, 2012. **18**(1): p. 56-67.
240. Zein, I., et al., *Fused deposition modeling of novel scaffold architectures for tissue engineering applications*. *Biomaterials*, 2002. **23**(4): p. 1169-1185.
241. Chin Ang, K., et al., *Investigation of the mechanical properties and porosity relationships in fused deposition modelling-fabricated porous structures*. *Rapid Prototyping Journal*, 2006. **12**(2): p. 100-105.
242. Hutmacher, D.W., et al., *Mechanical properties and cell cultural response of polycaprolactone scaffolds designed and fabricated via fused deposition modeling*. *Journal of biomedical materials research*, 2001. **55**(2): p. 203-216.
243. Cao, T., K.-H. Ho, and S.-H. Teoh, *Scaffold design and in vitro study of osteochondral coculture in a three-dimensional porous polycaprolactone scaffold fabricated by fused deposition modeling*. *Tissue engineering*, 2003. **9**(4, Supplement 1): p. 103-112.
244. Hutmacher, D.W., *Scaffolds in tissue engineering bone and cartilage*. *Biomaterials*, 2000. **21**(24): p. 2529-2543.



245. Lebourg, M., et al., *Biodegradable polycaprolactone scaffold with controlled porosity obtained by modified particle-leaching technique*. Journal of Materials Science: Materials in Medicine, 2008. **19**(5): p. 2047-2053.
246. Tan, J., C. Chua, and K. Leong, *Fabrication of channeled scaffolds with ordered array of micro-pores through microsphere leaching and indirect rapid prototyping technique*. Biomedical microdevices, 2013. **15**(1): p. 83-96.
247. Draghi, L., et al., *Microspheres leaching for scaffold porosity control*. Journal of materials science: materials in medicine, 2005. **16**(12): p. 1093-1097.
248. Maurer, M.M., et al., *Prosthetic meshes for repair of hernia and pelvic organ prolapse: Comparison of biomechanical properties*. Materials, 2015. **8**(5): p. 2794-2808.
249. Grundfest-Broniatowski, S., *What would surgeons like from materials scientists?* Wiley Interdisciplinary Reviews: Nanomedicine and Nanobiotechnology, 2013. **5**(4): p. 299-319.
250. Arjun, G. and P. Ramesh, *Structural characterization, mechanical properties, and in vitro cytocompatibility evaluation of fibrous polycarbonate urethane membranes for biomedical applications*. Journal of Biomedical Materials Research Part A, 2012. **100**(11): p. 3042-3050.
251. Dempsey, D.K., et al., *Comparative analysis of in vitro oxidative degradation of poly (carbonate urethanes) for biostability screening*. Journal of Biomedical Materials Research Part A, 2014. **102**(10): p. 3649-3665.

## VITA

### ANDREW TODD MILLER

Andy was born in July of 1987 in Westlake, Ohio and resided in Lakewood and Highland Heights, Ohio, before moving to Canonsburg, Pennsylvania and then finally Alpharetta, Georgia in the spring of 2001. From 2001 to 2005 he attended Chattahoochee High School and swam competitively for Dynamo Swim Club. Andy began his undergraduate studies at Georgia Tech in the fall of 2005, eventually earning his Bachelor's and Master's degrees in Civil Engineering in December of 2009 and 2010, respectively. During this time, he also competed on the Georgia Tech swim team, eventually becoming team captain and qualifying for the NCAA Championships in the 100 yard breaststroke. Following his graduation in 2010, Andy worked for several years as a structural engineer at a nuclear power consulting firm in Kennesaw, Georgia. During this time, he became increasingly discontent with the opportunities available to him in the industry. Unsure of what to do, he stumbled upon the Georgia Tech Bioengineering graduate program website one fateful morning in September of 2012. After receiving overwhelming support from his wife, parents, and in-laws, he decided to apply. Thanks to the support of Dr. Gall and Dr. Guldberg, he was eventually offered a tremendous opportunity to return to Georgia Tech in 2013 for a PhD in Bioengineering. Outside of his research, Andy enjoys working out, target shooting, and brewing/drinking beer (separately, of course), and has competed in the Crossfit Games team division four times (2012-2015) to appease his competitive nature.